Aus dem Zentrum für Medizinische Forschung
der Medizinischen Fakultät Mannheim
Direktor: Prof. Dr. med. Norbert Gretz

Influence of blue light on skin models consisting of human fibroblasts and keratinocytes

Inauguraldissertation
zur Erlangung des akademischen Grades
Doctor scientiarum humanarum (Dr. sc. hum.)
der
Medizinischen Fakultät Mannheim
der Ruprecht-Karls-Universität
zu
Heidelberg

vorgelegt von
Natalia Kuch

aus
Saran, Kasachstan
2019

Dekan: Prof. Dr. med. Sergij Goerdt
Referent: Prof. Dr. med. Norbert Gretz

ABBREVIATIONS

$\Delta\Psi_m$	Metabolic membrane potential
ALT	Alanine aminotransferase
ANOVA	Analysis of variance
AST	Aspartate aminotransferase
ATP	Adenosine-triphosphate
BW	Body weight
CLS	Cell line service
CRP	C-reactive protein
DFU	Diabetic foot ulcer
DMEM	Dulbecco's modified eagle medium
DMSO	Dimethyl sulfoxide
ECM	Extracellular matrix
EDTA	Ethylene-diamine-tetra-acetic acid
FACS	Fluorescence-activated cell sorting
FBS	Fetal bovine serum
FGF	Fibroblast growth factor
GSEA	Gene set enrichment analysis
GLDH	Glutamate dehydrogenase
HaCaT	Immortalized human keratinocytes
H&E staining	Haematoxylin and eosin staining
IL	Interleukin
IR	Infrared
KEGG	Kyoto encyclopedia of genes and genomes
LED	Light emitting diode
LLLT	Low-level light therapy
MMF	Midazolam medetomidine fentanyl
NES	Normalized Enrichment Score
NF-κB	Nuclear factor of kappa light polypeptide gene enhancer in B cells 1
NaCl	Sodium-chloride
NHDF	Normal human dermal fibroblasts
PBM	Photobiomodulation
PBS	Phosphate buffered saline
PDGF	Platelet-derived growth factor

PFA	Paraformaldehyde
ROS	Reactive oxygen species
TNF	Tumor necrosis factor
UV	Ultraviolet
VIS	Visible light
XTT	Sodium 3´-[1-(phenylaminocarbonyl)-3,4-tetrazolium] bis(4-methoxy-6-nitro)benzene sulfonic acid hydrate
ZDF fa/+	Zucker diabetic fatty rat – healthy non-diabetic control animal (heterozygous)
ZDF fa/fa	Zucker diabetic fatty rat – diabetic animal (homozygous)

1 INTRODUCTION

1.1 Human skin

The human skin consists of three layers: epidermis, dermis and hypodermis (subcutaneous fat) (Figure 1).
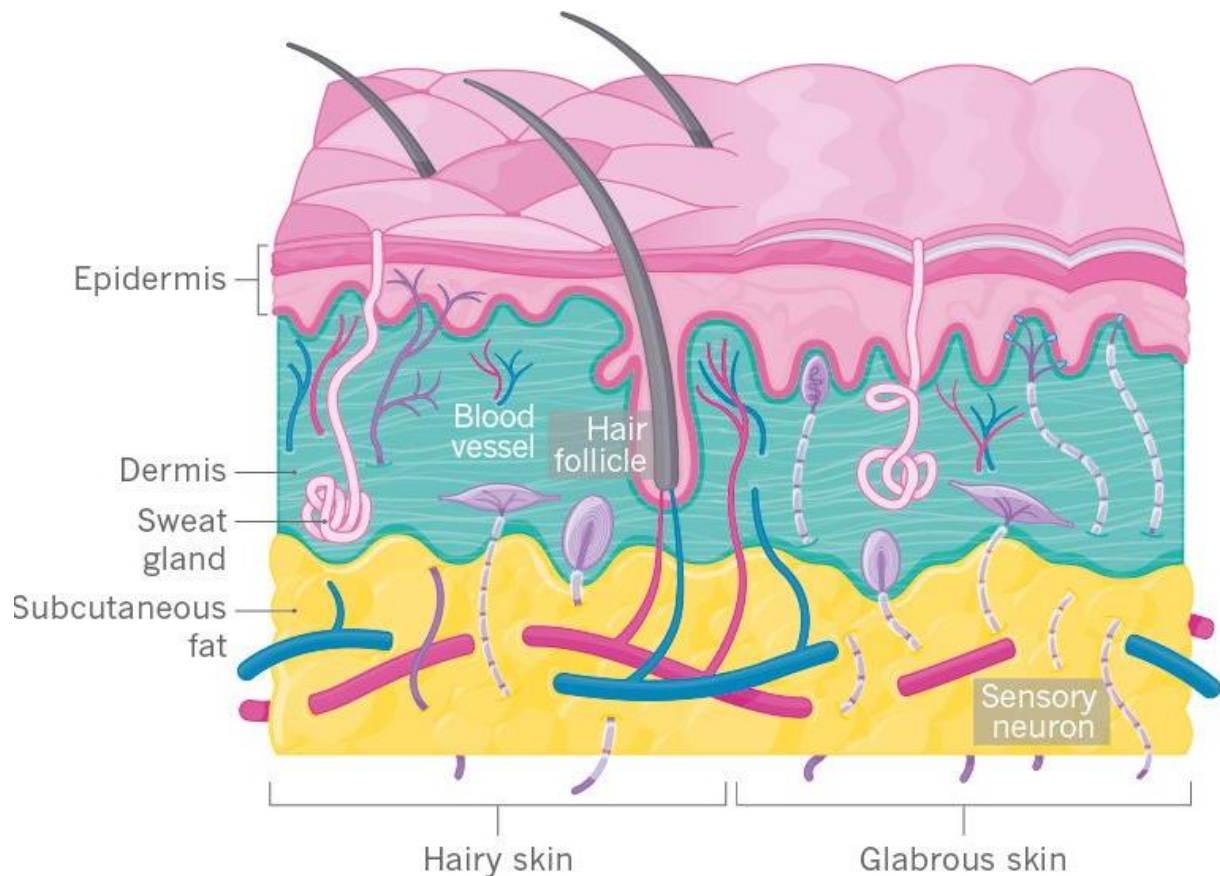
Figure 1: Structure of the human skin consisting of the epidermis, dermis and subcutaneous fat [1].

Thin, hairy skin makes up 90% of the body's surface, while the remaining 10% are covered by thicker, glabrous skin, which contains more sensory neurons to be able to perform delicate tasks [1]. The outermost layer, the epidermis, protects the organism against chemical, biological and mechanical harm. It prevents water loss, while simultaneously acting as a barrier for pathogens of microbial or chemical nature [2-4]. The epidermis is separated from the underlying dermis by the basement membrane, which is linked to the dermis by short fibrils [5]. The vascularized dermis is composed of connective tissue consisting of collagen and elastin, where structures such as hair follicles, nerve endings, sebaceous and sweat glands are embedded [1, 6]. Various types of nerve endings make it possible to distinguish between sensations such as

heat, itching, pain and pleasure [1]. Sebaceous glands surround hair follicles and produce sebum, which is a fatty material keeping skin and hair soft and pliable.
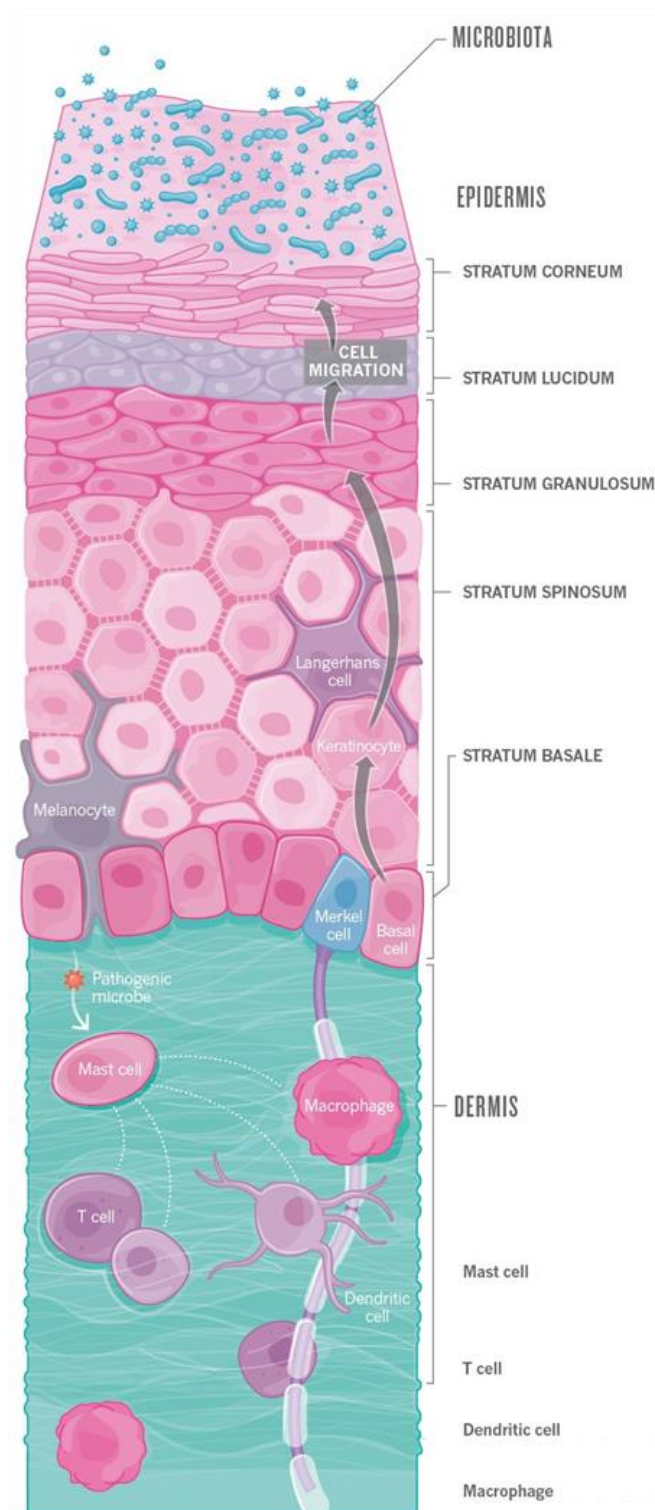
Figure 2: Detailed structure of the epidermis and dermis and its cells. The maturation of basal cells is shown and how they move from the stratum basale up to the stratum corneum[1].

Below the dermis lies the subcutaneous fat or hypodermis. Its purpose is to insulate the organism by retaining body heat while simultaneously protecting against heat from the environment. Small blood vessels in the dermis have their origin here, where the major blood vessels that supply the skin lie [5].

The detailed structure of the skin and which cells are present in the different layers is shown in Figure 2. The epidermis mainly consists of keratinocytes that have their origin in the stratum basale. Here, basal cells are dividing continuously, maturating and becoming keratinocytes. Melanocytes are also present in the stratum basale, where they produce melanin, causing skin pigmentation. In case of DNA damage by UV irradiation, melanocytes can turn into skin cancer, known as melanoma cells. By dividing continuously, basal cells push newly matured keratinocytes upwards to the surface of the skin. In the stratum spinosum keratinocytes accumulate, producing keratin. Keratin makes the skin water-proof and gives it strength and firmness.

Langerhans cells, located in the stratum spinosum, can react to allergens of microbial infiltration, which are bound to epidermal proteins [7].

The further upwards keratinocytes move the flatter and more keratinized they are becoming. Because of the increasing distance from the vascularized dermis, they start to lack nutrients and slowly die [5]. Due to the increasing amount of keratin, the stratum granulosum is a water-proof barrier. The stratum lucidum is what defines thick, glabrous skin, which can only be found on the palms and soles [1, 5]. The stratum corneum is the outermost layer of the epidermis and completely consists of flat dead cells. The cells structures cannot be distinguished and are not nucleated anymore and eventually they shed [5].

In addition to providing elasticity through collagen secretion by fibroblasts [8], the dermis also provides immunological defense against microbial invasion. Mast cells recognize pathogenic antigens and activate other immune cells through chemical signals. T cells act as an immunological memory and can react faster to known pathogens. Dendritic cells absorb antigens and can in turn activate other immune cells. Macrophages digest cell debris of destroyed microbes.

1.2 Wound healing

When skin integrity is impaired by physical injury, chemical or biological harm, precisely orchestrated mechanisms take place. They are separated into hemostastis/inflammation phase, proliferation phase and remodeling phase. They are sequential but include overlapping mechanisms [9].

In the first phase hemostasis leads to the formation of a fibrin clot. It serves as a scaffold, but also attracts inflammatory cells by the release of chemokines and growth factors from degranulating platelets [10, 11]. Neutrophils cleanse debris and bacteria and in turn macrophages facilitate phagocytosis of the remains [12]. They release growth factors and cytokines (IL 1, IL 6, TNFα, FGF2) activating fibroblasts to proliferate and form a provisional matrix [13], thereby initiating the proliferative phase. Keratinocytes close the epidermis by migration from the margins and using the matrix as support. The extracellular matrix containing proteoglycans, collagen and elastin form a granulation tissue and replace the fibrin clot [14].

In the last phase of wound healing the granulation tissue is remodeled. Here, new cells are produced while existing cells are removed by apoptosis. The extracellular

matrix is degraded and immature type III collagen is replaced by mature type I collagen [15, 16].

1.2.1 Impaired wound healing and scar formation

Sometimes normal repair mechanisms cannot be executed. This can lead to the development of chronic wounds, which are defined by persistent wounds that do not or heal only slowly in an extensive period of time. This leads to barrier defects and structural and functional integrity cannot be restored [17]. Mainly, there are three major types of chronic wounds, which are divided by their cause of origin: Vascular insufficiency (venous leg ulcers), diabetes mellitus (diabetic foot ulcer (DFU) and high local pressure (pressure ulcers) [13]. They are defined by nonmigratory epidermis, persistent inflammation, presence of infection, and biofilm formation. Underlying causes for diabetic foot ulcers are atherosclerotic diseases. Arterial blood supply is reduced, which causes tissue hypoxia and therefore damage. False or lack of medication can further contribute to the formation of DFUs, as small vessels and tissue can be damaged by hyperglycemia [18]. Diabetes is often a cause of obesity, where hyperlipidemia adds to the existing conditions. The morbidity and mortality for these conditions are quite high, as 15% of diabetes patients will develop a foot ulcer. Even treated chronic wounds often result in amputation of which the 5-year mortality rate is around 50% [19].

All of these conditions lead to an imbalanced immune response, where inflammatory and anti-inflammatory responses are misbalanced [13, 20]. Studies show that proinflammatory cellular infiltrates lead to delayed wound healing. Proinflammatory cytokines as IL-1β and TNFα are deregulated and therefore prolong the inflammatory phase [21, 22]. This leads to elevated metalloproteinases which degrade the ECM of the wound site and impair migration [23].

The other side of impaired wound healing are a hyperproliferative epidermis which can cause hypertrophic scars or keloids. It contains thick collagen fibers which extend beyond the margins of the tissue damage [13]. They are characterized by highly inflammatory processes, up-regulated fibroblast activity and excessive ECM deposition [24]. Hypertrophic scars are usually self-limited and are more of a cosmetic concern than a severe disease [25].

1.2.2 Therapies to improve wound healing

As obesity is becoming a global epidemic, chronic diseases as type 2 diabetes are a common consequence [26]. By the implied rise of chronic wounds, development of new strategies for chronic wound management is essential.

First interventions are always the application of wound dressings. They protect the open wound from contaminations while providing moisture and absorbing excess exudate. They can have antibacterial properties or stimulate cells to proliferate and migrate or induce matrix deposition [13]. Current popular dressings are hydrocolloid dressings, which can trap fluid and are occlusive, but cannot be used for infected wounds. Hydrogels with integrated therapeutics can also rehydrate wounds, but may cause over-hydration [27]. Wound dressings, while helpful, have limitations and have only a small impact on enhancement of chronic wound healing.

Topical application of growth factors, especially platelet-derived growth factor, was attempted and had positive effects on wound healing, but only to a small extent [28-30]. In contrast to other methods, this therapy seems to focus only on one factor. While growth factors are reduced in chronic wounds, many more molecules come into play and it seems unlikely that by replacing one of them all of the processes can be brought back to normal [27].

Cellular products are widely used in regenerative therapies. They are not only used for chronic wounds, but also burns can be treated with allogeneic grafts. Epidermal keratinocytes are cultured and rapidly expanded using a feeder layer of murine fibroblasts [31]. They have been shown to be quite effective, but are expensive and pose a risk of infection, also only a limited number of clinical trials exists [27, 32].

Non-conventional therapies include negative pressure wound therapy. Negative pressure is applied by a device to optimize blood flow and remove exudate. Apparently, a reduction of wound edema and stimulation of granulation tissue formation adds to the advantages of this therapy. Studies showed that wounds treated with negative pressure, have reduced rates of infection from gram-negative bacteria [33].

1.2.3 Photobiomodulation

Photobiomodulation (PBM), also known as low level laser therapy (LLLT), is a non-pharmacological and non-invasive strategy [34-39] to tackle different medical conditions including wound healing. Here, non-ionizing light in the visible or near-infrared

spectrum is used at a relatively low irradiance. While heat is produced, the mechanism of action does not include thermal effects, but rather rely on the absorption of photons by chromophores. Effects include neuroprotective responses, improvements in metabolism, blood flow and neurogenesis while decreasing inflammation and oxidative stress [40].

One of the first medical benefits of PBM was discovered in 1967, when E. Mester tried to cure malignant tumors in rats with a ruby laser, by repeating an experiment of McGuff [41]. As the power of the laser was too low, he was not successful in curing the tumors, but noticed enhanced hair growth and improved wound healing of the irradiated area [42, 43]. Since then, many applications of PBM have been found. It is widely used in the treatment of back pain [44] and wounds [45]. Blue light has been used against neonatal jaundice for over 60 years, firstly discovered by Cremer et al. [46, 47], who showed that bilirubin in neonates could be reduced [48-50]. The use of PBM is also investigated for treating neurological conditions, including traumatic brain injury and neurodegenerative diseases as Alzheimer's and Parkinson's disease [51-57].

PBM finds application also for cosmetic purposes such as acne treatment and improvement of scarring [58, 59], decreasing severity of wrinkles [60] and regrowing hair [61].

As PBM is seen as a strategy in regenerative medicine, it also found applications in sport sciences. While treatment with mostly red and infrared light can improve muscle strength and therefore performance, it can also be used to prevent muscle damage after excessive exercise [62-65].

As a light source, lasers or light emitting diodes (LEDs) are used. They are either employed in continuous or pulsed modes. The wavelength is an important characteristic, where blue light in the range of 400 – 450 nm is mostly used against neurologic conditions and with anti-inflammatory purposes. Red and infrared light in the spectrum between 600 – 690 nm and 700 – 900 nm are used against inflammatory diseases and for treatment of muscle tissue. Important parameters are the irradiance or power density (mW/cm²) which should not exceed a certain threshold, otherwise thermal effects would overshadow the photochemical processes and could result in burns. The irradiation time is also an aspect that should not be neglected, as together with the irradiance it defines the fluence or energy density (J/cm²). All in all these three factors are prone to errors, as outcomes rely heavily on

their precise adjustment. Effects can vary strongly if for instance the overall fluence is the same, but irradiance and irradiation time are adjusted. The typical biphasic dose-response curve of PBM is the reason for this. While one dose can trigger certain effects, another dose with the same wavelength and irradiance can trigger the contrary. This follows the 'Arndt-Schulz Law' which states that weak stimuli accelerate cell activity, whereas stronger stimuli suppress it [66, 67].

The first law of photochemistry states that light or photons must be absorbed by photoacceptors for photochemistry to occur. If a certain wavelength is not absorbed by anything in the tissue, no photobiological effects can be triggered [68, 69].

Light of the VIS and NIR spectrum was shown to be absorbed by the respiratory chain molecules in mitochondria, for instance cytochrome C oxidase. This leads to an increased metabolism and by signal transduction other effects are triggered [68].

The main mechanisms in the signal transduction of photoacceptors changed by light were identified. The metabolic membrane potential ($\Delta\Psi_m$) is affected by VIS and IR light and stimulates ATP synthesis and the consumption of O_2 [70-72]. A misconception that ROS are only damaging by-products of respiration could be revealed. Mitochondrial ROS was found to be important for cellular signaling, including retrograde mitochondrial signaling [73-76]. Broadband radiation was found to increase mitochondria-derived ROS formation and caused an increase of intracellular redox potential [77]. Further, an increase in Ca^{2+} could be measured after irradiation with VIS light, which was released by affected mitochondria [78]. The interplay of Ca^{2+}, $\Delta\Psi m$ and ROS trigger several pathways to be up-regulated, including NF-κB [79], c-fos [80], DNA and RNA synthesis [81].

1.3 Aim of the study

The aim of the project was to test, whether the effects of photobiomodulation with blue light that were identified for keratinocytes and fibroblasts, also hold true for co-cultures consisting of both of the cell lines. The effects on metabolic activity and proliferation should be determined for low dosages (10.35 J/cm²), where an increase for both cell lines was already proven in mono-cultures [82, 83]. Also higher dosages (41.40 J/cm²) that cause an inhibitory effect should be investigated concerning these aspects.

After these effects were proven *in vitro*, these experiments should be translated to *in vivo* studies. Here, short and long-term effects were analyzed with the addition of a fluence of 82.80 J/cm², which was found to inhibit bacterial growth. The analysis *in vivo* should give results on whether an impairment of wound healing is taking place.

Further, the findings were translated to the application of a portable device. The device had to be tested on its efficacy and safety for irradiation of patients. Therefore temperature development was tested on porcine skin.

Key questions of the project are:

- Does blue light irradiation have the same effects on co-cultures as it has on mono-cultures of keratinocytes and fibroblasts?

- Can results found in cell culture be translated to animals and what are the effects on wound size, plasma parameters, histology and gene expression after single irradiations of different fluences?

- Is it possible to develop a stable animal model for diabetes?

- Does blue light irradiation affect the wound size of diabetic animals?

- Which long-term effects does blue light cause, regarding plasma, histology and gene expression?

- If a portable device for the treatment of chronic wounds can be developed, is its efficacy and safety ensured?

2 MATERIALS AND METHODS

2.1 Material list

2.1.1 Substances

Description	Manufacturer
Fentanyl citrate	Janssen Cilag
Fetal Bovine Serum (FBS), heat-inactivated	Life Technologies
Fibroblast Growth medium 3 SupplementMix	PromoCell
Fibroblast Growth medium 3 SupplementMix, serumfree	PromoCell
Isoflurane	CP-Pharma
Ketamidor (Ketamine)	WDT
Midazolam (Midazolam)	Ratiopharm
Penicillin-Streptomycin	Thermo Fisher Scientific
Phosphate buffered saline (PBS)	Life Technologies
Rimadyl (Carprofen)	Zoetis
Trypan Blue Solution, 0.4%	Sigma-Aldrich
Trypsin-EDTA, phenol red, 0.25%	Thermo Fisher Scientific
Xylazine	WDT

2.1.2 Kits

Description	Manufacturer
Agilent RNA 6000 Nano Chip Kit	Agilent Technologies
Colorimetric Cell Viability Kit III (XTT)	Promocell
GeneChip® Hybridization, Wash and Stain Kit	Thermo Fisher Scientific
GeneChip® WT Plus Reagent Kit	Thermo Fisher Scientific
Rat C-Reactive Protein ELISA Kit (PTX1)	Abcam
RNase-Free DNase Set	Qiagen
RNeasy Fibrous Tissue Mini Kit	Qiagen

2.1.3 Equipment

Description	Manufacturer
12-Well plates, black, glass bottom	In vitro Scientific
AcuPunch Skin Biopsy Punches, 6mm	Acuderm
ACCU-CHEK® Compact Glucose (Test Strip)	Roche Diagnostics
Cell Culture Flasks, different sizes	Greiner Bio-One International

Cell Culture Multiwell Plate 12-well, transparent	Greiner Bio-One International
Corning® Costar® 6-Well Plates, transparent	Sigma-Aldrich
Corning® Costar® 96-Well Plates, black, clear bottom	Sigma-Aldrich
Elastic net bandage, 3.5 cm width	MaiMed Medical
GeneChip® Rat Genome 230 2.0 Microarrays	Affymetrix
Leukosilk®	BSN Medical
LUNA™ Cell Counting Slides	Logos Biosystems
NanoQuant Plate™	Tecan Group
NG4 grey glass filter after Schott, 10%, D1.0	ITOS
PMI 5008 mod. rat feed	ssniff Spezialdiäten
Prototype Pocket M4000	Laboratoires URGO S.A.
Skin polymer model	Laboratoires URGO S.A.
ThinCert™, 0.4 µm, transparent	Greiner Bio-One International
UrgoStart Wound Dressing E2723	Laboratoires URGO S.A.

2.1.4 Devices

Description	Manufacturer
818-ST2-UV/DB Metal Wand Photodetector	Newport Corporation
ACCU-CHEK® Compact Plus Glucometer	Roche Diabetes Care
Agilent 2100 Bioanalyzer	Agilent Technologies
Automatic Tissue Processor TP1020	Leica Biosystems
Axio Scan.Z1 Microscope	Carl Zeiss
BioLight LED lamp	Philips Research
Cobas c 311 Analyzer	Roche Diagnostics
Digital Multimeter DMM230	Multmetrix®
DNA Engine® Peltier Thermal Cycler	Bio-Rad
Economical Handheld Laser Power & Energy Meter, 843-R-USB	Newport Corporation
Eppendorf® Microcentrifuge 5415 L	Eppendorf
GeneChip® Cartridge Array	Affymetrix
GeneChip® Hybridisation Oven 640	Affymetrix
GeneChip® Fluidics Station 450	Affymetrix
GeneChip® Scanner 3000	Affymetrix
HERAcell™ VIOS 160i Incubator	Thermo Fisher Scientific
Heraeus® Biofuge, primo R	Thermo Fisher Scientific
HERAsafe™ Laminar Flow Cabinet	Thermo Fisher Scientific
IncuCyte® ZOOM System	Essen Bioscience
Infinite® M200 PRO Microplate Reader	Tecan Group

Inverted Microscope DM IRB	Leica Microsystems
LUNA™ Automated Cell Counter	Logos Biosystems
Microscope DM IRBE	Leica Microsystems
MEDILIGHT prototype	MEDILIGHT
Spark® 10M Multimode Microplate Reader	Tecan Group
ST5010 Autostainer XL	Leica Biosystems
Thermocouple Type K	RS PRO
ThermoStat Plus	Eppendorf
TissueLyser II	Qiagen
USB TC-08 Thermocouple Data Logger	Pico Technology

2.1.5 Software

| Description	Manufacturer/Application
AutoScratchSeg (MATLAB)	*MATLAB based GUI program to determine wound areas of scratch assay*
AutoWoundSeg (MATLAB)	*MATLAB based GUI program to determine wound areas of animals*
Bio-formats (Fiji function)	*Open source software to import images from Axio Scan microscope from Zeiss*
Countpix Macro	*Fiji macro to process segmented ilastik images*
Fiji	*Open source software for image analysis based on ImageJ*
Ilastik	*Open source software for interactive image classification, segmentation and analysis based on Python*
IncuCyte® S3 Acquisition interface	Essen BioScience
JMP Genomics version 7.1	SAS Institute Inc.
Leica Application Suite X (LAS X)	Leica Biosystems
MEDILIGHT App V2.5	MEDILIGHT
PicoLog 6 data logging software	Pico Technology
PMManager Application Software	Newport Corporation
ZEN 2 (blue edition) Axio Scan software	Carl Zeiss

2.2 Light sources and their characteristics

For the various *in vitro* and *in vivo* experiments, different light sources were used. The properties of their set-up and the characteristics of the LEDs used are listed in Table 1 for each type of lamp.

Table 1: Properties of different light sources used in the experiments.

	Philips BioLight	ENMECH board	MEDILIGHT Prototype
Distance to Surface [cm]	5	5	0
Number of LEDs	128	84	32
Irradiance [mW/cm²]	23	23	23
Peak Wavelength [nm]	453	455	453
Irradiation field [cm²]	150	316	16

The lamp provided by Philips Research (Eindhoven, Netherlands) was used for the initial *in vitro* experiments. The light source consists of LUXEON Rebel LXML-PR01-0275 (blue) LEDs from Lumileds (Amsterdam, Netherlands). 12- and 96-well plates were irradiated at a distance of 5 cm in this set-up, as shown in Figure 3.

Figure 3: Irradiation set-up for *in vitro* studies with the Philips BioLight.

For *in vivo* short-term and the first long-term irradiation experiments a rigid board was used that was built by ENMECH (Berlin, Germany). For the LEDs the LUXEON Z Royal Blue LXZ1-PR01 from Lumileds were used. The peak wavelength is between 450 and 455 nm and the lamp was used, as well as the Philips lamp, at an irradiance of 23 mW/cm². Between the lamp and the animal a diffusion plate was placed to increase homogeneity of the irradiation field (Figure 4).
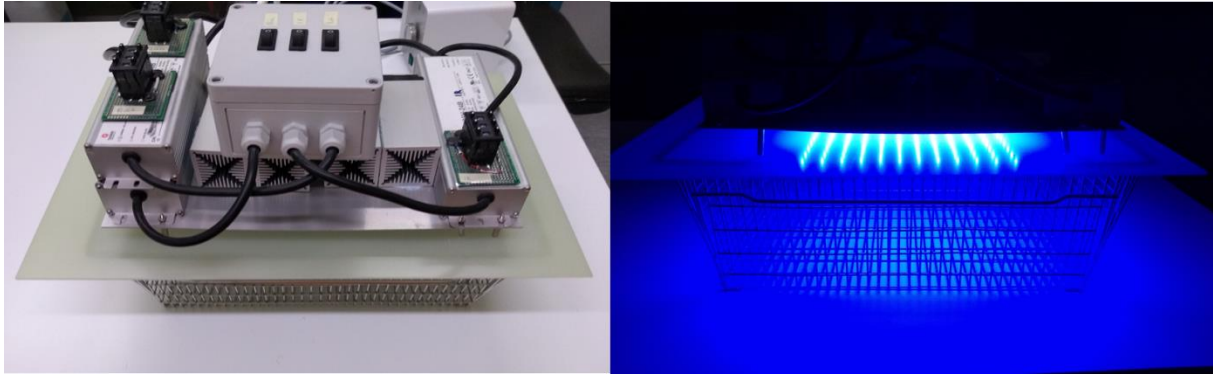
Figure 4: Irradiation set-up for *in vivo* studies with the ENMECH board.

In vitro as well as *in vivo* experiments were performed with the MEDILIGHT prototype. In contrast to the previous two light sources (Philips and ENMECH) there was no distance between the plate/animal and the LEDs. Irradiance was always set to 23 mW/cm² adjustable by the duty cycle in the MEDILIGHT software. The MEDILIGHT prototype consists of two parts: the encapsulated, electronic module and the flexible LED foil (Figure 5). In the electronic module the battery and the control unit for the LEDs and sensors are integrated, as well as a data transmitter. It is encapsulated in a plastic housing and can be attached to a diabetic pressure relief shoe with a plastic clip. Throughout the experiments, the prototype was developed and components added. One of these components is a white back reflector that is attached to the LED foil to reflect scattered light. Also, the flexible foil was encapsulated with silicone to prevent pressure marks from the integrated parts. Additionally the silicone encapsulation makes it possible to disinfect the device. During optimization the battery capacity and the range of irradiance was increased. Also the connection between the flexible foil and the electronic module was made more stable and the encapsulation of the electronic module was redesigned to be water-resistant.

Figure 5: MEDILIGHT Prototype consisting of the electronic module and silicone encapsulated flex foil.

On top of that two different types of sensors were placed on the LED foil (Figure 6). First, there are five temperature sensors, of which one is placed in the center and the other four on each corner of the flexible foil. These sensors can measure the patient's or the animal's skin temperature, as well as monitor the temperature of the LEDs. Second, there are four pulse oximetry sensors, consisting of red and infrared LEDs, respectively, as well as a photodiode. They are used to monitor and map changes in blood oxygenation levels, but are not relevant for this study.
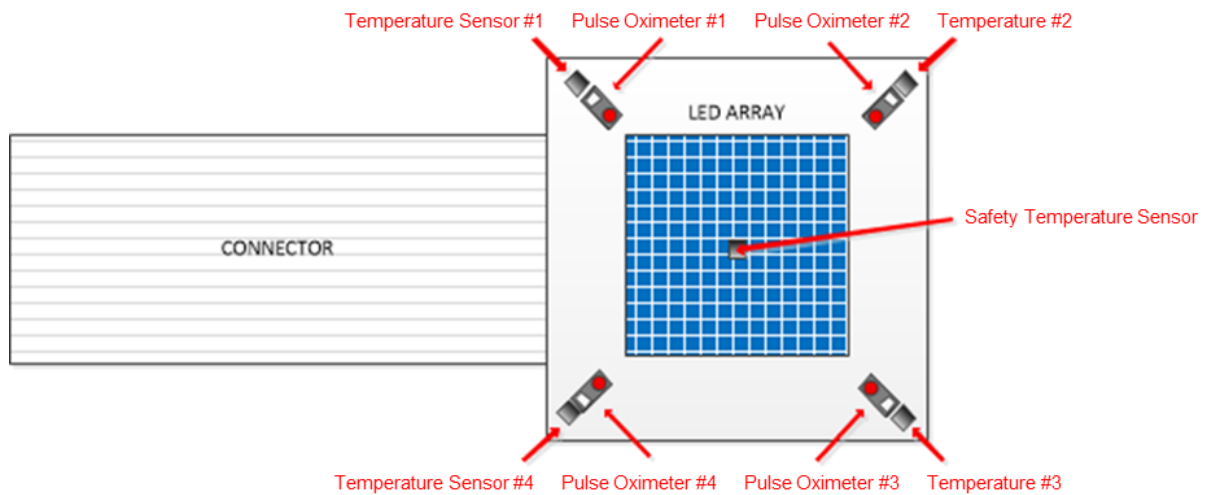
Figure 6: Schematic display of MEDILIGHT flex foil with respective sensors for temperature and pulse oximetry. Image was taken from MEDILIGHT deliverable created by K. Michaelides[84].

The device is controlled by a phone App that is connected by Bluetooth. Different irradiation modes can be used. It is possible to adjust the maximum and minimum temperature for the central sensor, by LEDs turning on and off accordingly. Another possibility to regulate the irradiation time is to adjust the total irradiation time, the total break time, or the irradiation and break time independently from one another.

2.3 Development of an *in vitro* skin model and assessing the effects of blue light

2.3.1 Cell lines

For *in vitro* experiments two different cell lines were used (Table 2).

Table 2: Cell lines used to test effects of blue light *in vitro*.

Cell line	Species	Tissue	Medium	Company
HaCaT (immortal human keratinocytes)	Human	Skin	DMEM	CLS
NHDF (normal human dermal fibroblasts)	Human	Skin	DMEM	PromoCell

One was an immortal human keratinocyte cell line, HaCaT, which is a permanent cell line (spontaneously immortalized aneuploid human keratinocyte cell line).

16

Additionally, normal human dermal fibroblasts (NHDF) from an adult donor were used in the form of a primary cell line.

2.3.2 Culturing cells

For culturing HaCaT cells Dulbecco's modified Eagles medium with high glucose (DMEM GlutaMAX™) was used. Supplements were 10% fetal bovine serum (FBS), 1 mM sodium pyruvate and 100 U/mL penicillin/streptomycin (pen/strep) (Gibco® by Life Technologies (Carlsbad, CA, USA)). Standard conditions for culturing the cells were 37°C and a CO_2 concentration of 5%. For passaging 0.25% trypsin/EDTA from Gibco® was used as a dilution with phosphate buffered saline (PBS), producing a final concentration of 0.1%. Cells were incubated for 10 min under standard conditions to detach the cells. 1:20 dilutions were produced for long-term cultivation (2 weeks) and lower dilutions for use after 3 days (1:4 or 1:3). Volumes for different flask sizes of the solutions are listed in Table 3. For the NHDF cells DMEM GlutaMAX™ was used as base medium as well. Supplements were 100 U/mL pen/strep and SupplementMix Fibroblast Growth Medium 3 (with FBS) from PromoCell (Heidelberg, Germany) and 5 mL sodium pyruvate. Standard conditions for culturing were identical to the keratinocyte conditions. For passaging cells were treated with 0.25% trypsin/EDTA in a 1:16 dilution with PBS (final concentration of 0.04%). The cells were incubated for 3 min under standard conditions. 1:20 dilutions were made for long-term cultivation (2 weeks) and lower dilutions for use after 3 days (1:4 or 1:3). The cells were used up to passage 15. Volumes for different flask sizes of the used solutions are listed in Table 3 and are the same as for HaCaT cells.

Co-culture medium consisted of DMEM GlutaMAX™, 100 U/mL pen/strep, SupplementMix Fibroblast Growth Medium (without FBS) and 5 mL sodium pyruvate.

Table 3: Volumes of solutions for keratinocytes and fibroblasts, cultivated in different flask sizes (Txxx). The numbers of the flasks refer to the cultivation area in cm².

	T175 [mL]	T75 [mL]	T25 [mL]	96-well plate [mL]
Medium	25.0	15.0	5.0	0.100
PBS	5.0	3.0	2.0	0.050
Trypsin/EDTA (diluted in PBS)	5.0	3.0	2.0	0.050
Medium (stopping)	5.0	3.0	2.0	-

2.3.3 Co-culturing

In Figure 7 a schematic drawing is shown on how the fibroblasts were cultivated on the underside of the membrane. The cell culture insert from Greiner Bio-One International (Frickenhausen, Germany) 'ThinCert™' is positioned in a well and both insert and well are filled with medium, so that the fibroblasts are prevented from entering the inner part of the insert.
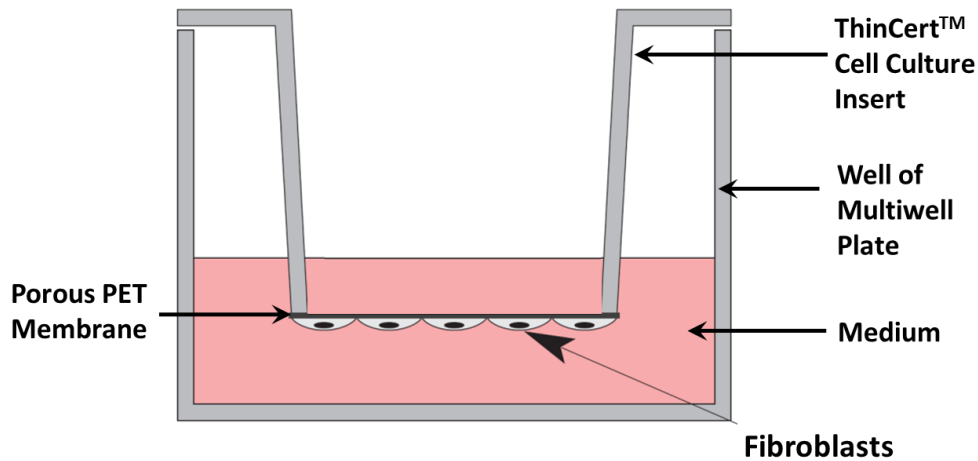
Figure 7: Cultivation model with cell culture insert 'ThinCert™' placed in a well with fibroblasts growing on the underside of the membrane. The well and the insert are both filled with medium [85].

In Figure 8 the co-culture model is presented. The keratinocytes are located on top of the membrane where they can communicate via signal peptides, but cannot mix with fibroblasts.
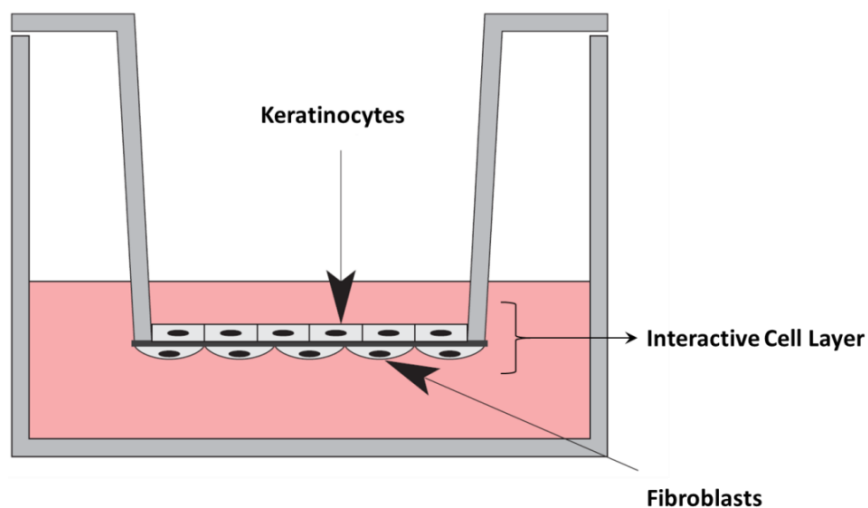
Figure 8: Co-cultivation model with cell culture insert 'ThinCert™' placed in a well with fibroblasts growing on the underside of the insert and keratinocytes growing inside of the insert. Together they form an interactive cell layer [85].

To gain this interactive cell layer 12-well ThinCerts™ with a transparent membrane (2×10^6 cm^{-1} pore density) and 0.4 µm pore size were inverted and placed into a

6-well plate (Figure 9/A). To create a humid environment 340 µL sterile water were pipetted to the bottom of the well (Figure 9/B). 200 µL of NHDF cell suspension containing 36,000 cells in fibroblast medium were pipetted onto the underside of the membrane (Figure 9/C+D).
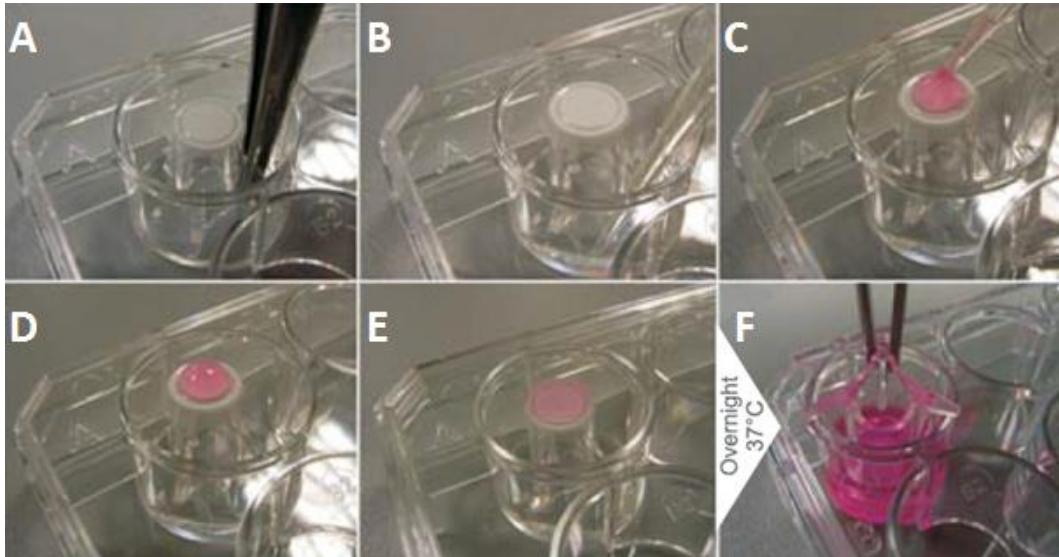
Figure 9: Procedure of preparing co-cultures with ThinCerts™ step by step [85].

The plate was covered with a lid, holding the cell suspension to the membrane (Figure 9/E). The cells were allowed to adhere overnight under standard conditions. Afterwards, the inserts were placed into a 12-well plate, pre-filled with 1.5 mL co-culture medium (described in 2.3.2) (Figure 9/F). 600 µL of HaCaT cell suspension containing 96,000 cells in co-culture medium were added into the insert well and cultivated overnight. On the next day experiments were started.

2.3.4 Harvesting of co-cultures for XTT assay in 96-well plates

To harvest the cells, the medium was removed from the bottom well, as well as from inside the ThinCerts™. The inserts and the well bottom were rinsed once with 2.0 mL PBS in total. 1.5 mL of 0.04% Trypsin/EDTA was added to the well bottom and incubated for 5 min at standard conditions. Meanwhile the PBS was left inside the insert to protect the keratinocytes from dehydration. Falcon tubes were pre-filled with 5 mL fibroblast medium and the fibroblast cell suspension was added after the incubation time. Then 0.3 mL 0.1% Trypsin/EDTA was pipetted into the insert and incubated for 5 min at standard conditions and the keratinocyte cell suspension collected in a Falcon tube prefilled with 5 mL keratinocyte medium. The tubes were vortexed to re-suspend the cells and centrifuged for 3 min at 220×g. The medium was removed from the centrifuge tube, leaving the cell pellet, which was re-

suspended in an appropriate amount of medium [85]. The cell suspension was divided into 96-well plates (100 µL per well) and incubated for 30 min at standard conditions with a subsequent XTT test.

2.3.5 Irradiation with blue light of mono-cultures and mixed cultures in 96-well plates

To study the effect of light irradiation on cells, cells were seeded in black 96-well plates with a clear flat bottom surface. For mono-cultures, HaCaT cells were seeded at a concentration of 10,000 cells/well and NHDF cells with 7,500 cells/well. In mixed cultures both cell types were seeded at a concentration of 5,000 cells/well respectively. The plates were incubated for 24 h at standard conditions and blue light irradiation with different irradiances followed. 24 h after irradiation XTT test was performed.

In prototype studies, the set-up was changed regarding the distance of the light source. While for the first experiments the Philips BioLight was used at a distance of 5 cm, the MEDILIGHT prototype was placed directly on top of the cell culture plate. Different configurations were tested where components were added to the set-up. Experiments with a spacer, diffusor and a wound dressing were performed to possibly increase the homogeneity of the illumination area, by simply placing one or more components between the cell culture plate and the LED foil.

2.3.6 Colorimetric cell viability (XTT) assay

To test possible changes of metabolic activity the Colorimetric Cell Viability Kit III from PromoKine was used. 50 µL of labeling-mixture containing labeling reagent and electron coupling reagent were added to the cell suspension and incubated for 1 h. Here the tetrazolium salt XTT is metabolized to water soluble formazan dye. Only viable cells have the ability to metabolize the salt, hence this kit is used to directly quantify the metabolic activity. The orange formazan is measured by spectrophotometric absorption at 450 nm (690 nm as reference wavelength) with Infinite® 200 PRO microplate reader from Tecan. Results of irradiated samples are normalized to the control, which were located on the same plate. Experiments were done in triplicates and repeated three times.

2.3.7 Scratch wound healing assay

First, cells (keratinocytes, fibroblasts or mixed culture) were seeded in 12-well plates with the cell numbers depicted in Table 4.

Table 4: Number of cells for different types of scratch tests.

Culture	Number of Keratinocytes per Well	Number of Fibroblasts per Well	Total cell number per Well	Cultivation time [h]
Keratinocytes	300,000	0	300,000	24
Fibroblasts	0	60,000	60,000	48
Mixed culture	45,000	45,000	90,000	48
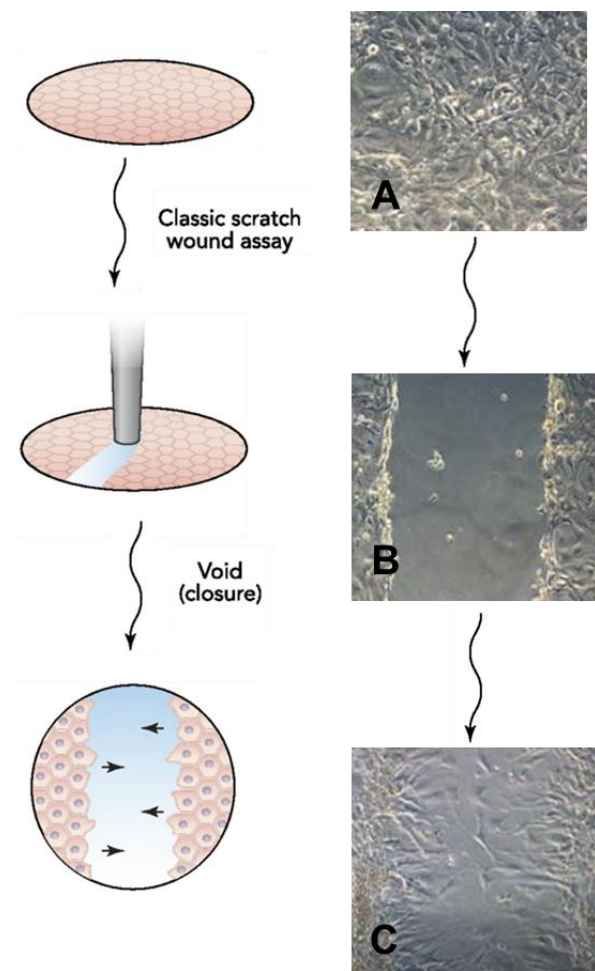
Figure 10: Work-flow of scratch wound healing assay [86, 87].

To test the migration and proliferation of cells, a scratch assay was performed. The workflow is shown in Figure 10. The respective cells were grown to confluence within 24 to 48 h. With a scratch device an artificial wound was created in the middle of the plate (see Figure 11) by removing cells in a defined area, causing gaps of the same size. By creating the artificial wound, cells were detached from the well surface; therefore a washing step with PBS followed and the wells were refilled with medium. At time point 0 h images of the gaps were taken directly after the procedure with an inverted microscope, followed by light treatment. Image acquisition took place in regular time intervals until the gap was closed completely.
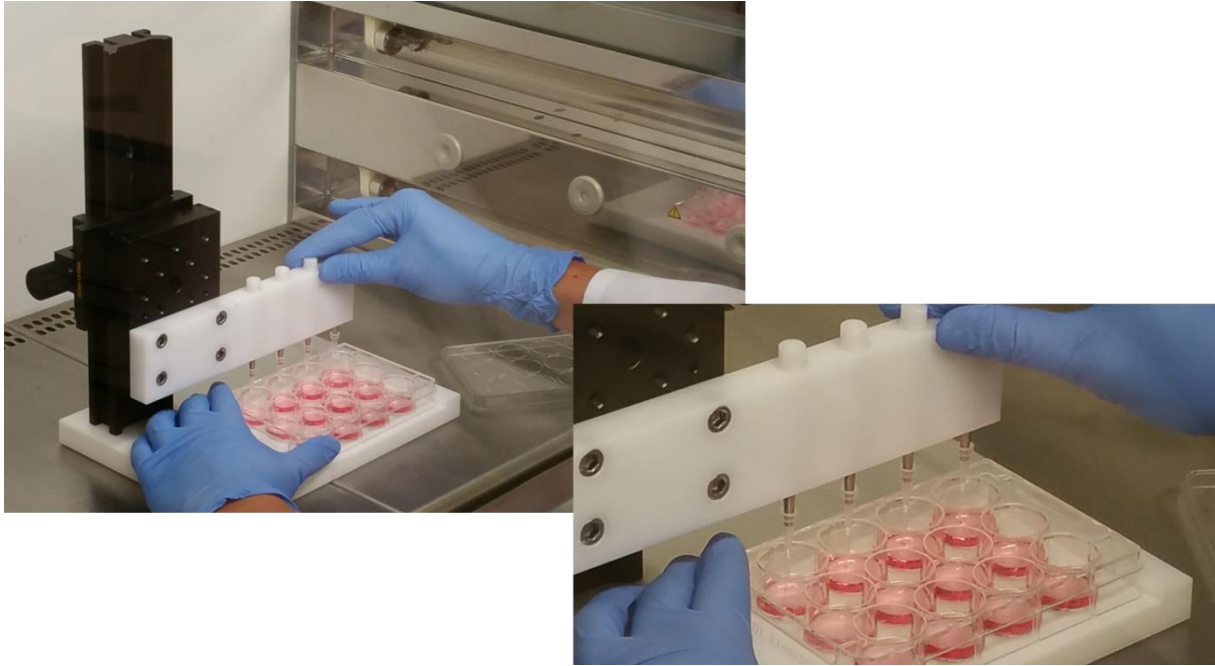
Figure 11: Scratch device used in 12-well plates to create an artificial wound.

Images were evaluated with the AutoScratchSeg program (Fiji plugin), where the area of the gap was determined in pixels (Figure 12) and further converted to % of the initial wound area at 0 h.
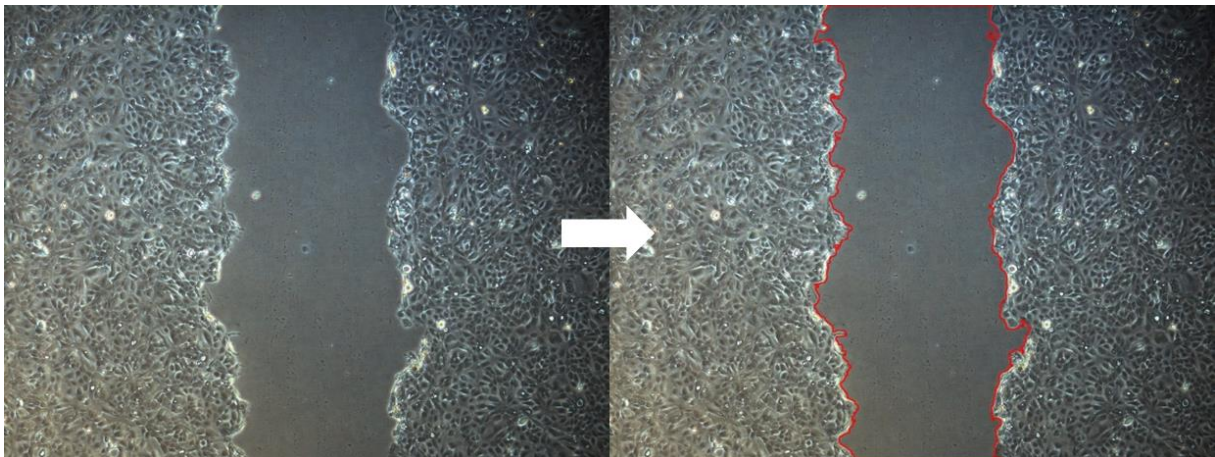
Figure 12: Exemplary evaluation of scratch wounds with the evaluation software AutoScratchSeg (based on MATLAB).

Two images per well were taken, generating 24 images per plate. Experiments were performed in triplicates with three repetitions.

2.4 *In vivo* studies to test the effects of blue light on rats

2.4.1 Animal groups

All experiments were conducted in accordance with the German Animal Protection Law and approved by the Regierungspräsidium Karlsruhe (in agreement with EU Guideline 2010/63/EU) with the permission number G-183/16.

To investigate short-term effects of blue light irradiation (section 2.4.2.1), 24 male ZDF fa/+ (lean) rats (Charles River Laboratories, Wilmington, MA, USA) at the age of 12 weeks, were used. All groups of rats are summarized in Table 5.

For both long-term experiments (section 2.4.2.2 for irradiation with ENMECH board and 2.4.2.3 for irradiation with the MEDILIGHT prototype) 12 male ZDF fa/fa (obese) rats (ZDF-*Lepr^fa*) were ordered, respectively, at the age of 6 weeks. Additional 6 male ZDF fa/+ (lean) rats (ZDF-*Lepr^fa*/Crl) were used in the first long-term experiment to compare the effect between the diabetic and non-diabetic wound model.

Table 5: Groups of rats used in the distinct experiments with their respective conditions and numbers.

Experiment	Rat Strain	Condition	Number of Animals	Animals per Experiment
Short-term irradiation	ZDF fa/+ (lean)	00.00 J/cm²	6	**Σ = 24**
		10.35 J/cm²	6	
		41.40 J/cm²	6	
		82.80 J/cm²	6	
Long-term irradiation (ENMECH board)	ZDF fa/fa (obese)	Control	6	**Σ = 18**
		Irradiated	6	
	ZDF fa/fa (lean)	Irradiated	6	
Long-term irradiation (MEDILIGHT prototype)	ZDF fa/fa (obese)	Control	6	**Σ = 12**
		Irradiated	6	

All rats were fed a special diet for 6 weeks, consisting of PMI 5008 mod. (ssniff Spezialdiäten, Soest, Germany). With 18 kJ% fat, 27 kJ% protein and 55 kJ% carbohydrates, this feed (Figure 13) is different from the standard, containing more fat and protein and therefore less carbohydrates (standard feed: 9 kJ% fat, 24 kJ%,

Gross Energy (GE)   **17.6 MJ/kg**
Metabolizable Energy (ME)   **14.7 MJ/kg**

100%   18 kJ%   Fat
80%
60%   27 kJ%   Protein
40%
   55 kJ%   Carbohydrates
20%
0%
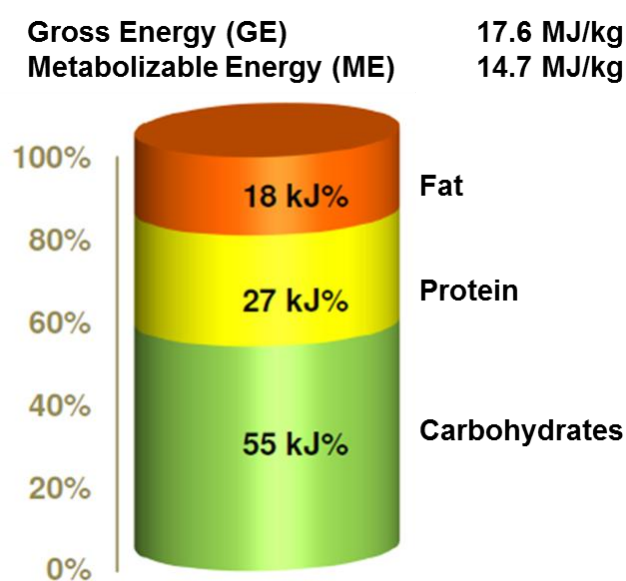
Figure 13: Energy content and distribution of ingredients [88].

67 kJ%). This led consistently to the development of Type 2 diabetes in the ZDF fa/fa strain, as they are homozygous for the leptin receptor gene deficiency. Before the start of the experiments all rats were housed in sets of two and three until reaching the age of 12 weeks, when they were separated and kept in individual cages. Food and water was provided *ad libitum.* The rats were exposed to a 12-hour light/dark cycle.

2.4.2 Study design for testing the effects of blue light on diabetic and non-diabetic rats

From *in vitro* studies different doses of blue light were identified for different treatment purposes. One of these is using a fluence of 10.35 J/cm² to achieve a proliferative effect, enhancing the epidermisation of a wound and faster wound closure. Further, 41.40 J/cm² were tested to induce an anti-proliferative effect, preventing premature wound closure. In addition, 82.80 J/cm² of blue light were tested. This fluence was found to not only induce anti-proliferative effects, but also to lead to anti-bacterial effects (separate project and experimenter). First, the doses had to be tested individually, leading to the design of short-term experiments. As no adverse effects were found, the whole light schedule, with all individual treatments included, was tested in a long-term study. To be able to apply the wound healing therapy in patients, the newly developed MEDILIGHT prototype was tested for its efficacy in a separate long-term study.

2.4.2.1 Short-term blue light irradiation of non-diabetic rats

To compare the short-term effects of blue light after a single irradiation with different doses of blue light, non-diabetic ZDF fa/+ rats were used. The rats were ordered at the age of around 8 weeks (no older rats were available) and housed until reaching the age of 12 weeks. Then, the experiment was started (Figure 14). Blood glucose measurements (see section 2.4.3) were performed weekly as well as monitoring of

body weight, until rats reached the desired age. Part of the back of the rats was depilated with an electric shaver for small rodents under short isoflurane anaesthesia to prepare it for application of the biopsy punch. As their skin was irritated from the shaving, all experiments were started on the next day.
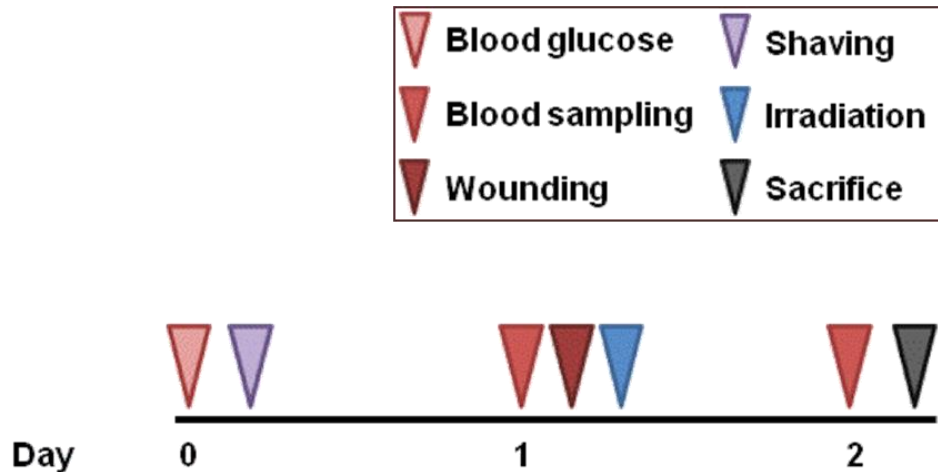
Figure 14: Experimental schedule for short-term irradiation with the ENMECH board.

Here, blood sampling took place under isoflurane anaesthesia and around 500 µL of blood were extracted from the retro-orbital venous plexus (section 2.4.4). While still under isoflurane anaesthesia, ketamine/xylazine was injected by intraperitoneal administration. The rats were relocated back into their cages for a quiet and dark environment. As soon as anaesthesia set in the skin surface was disinfected and two discs of skin were removed (Figure 15).
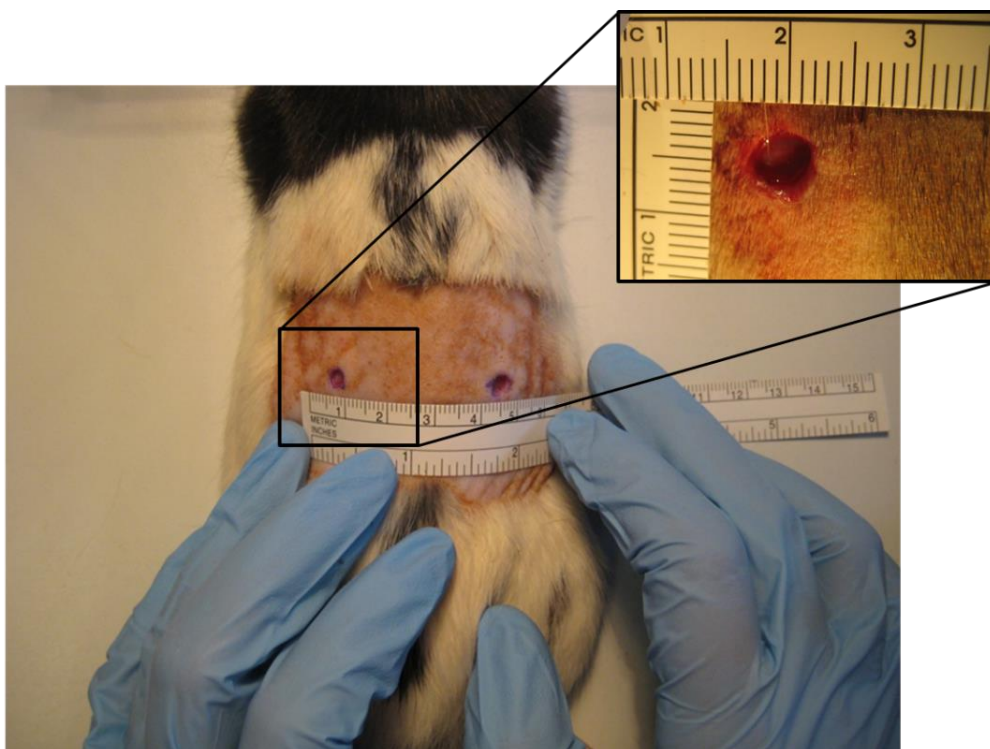
Figure 15: Two wounds created by a biopsy punch with a diameter of 6mm at a distance of 3 cm.

To create the wounds AcuPunch Skin biopsy punches from Acuderm were used with a size of 6 mm. Skin disks were extracted at a distance of 3 cm and consisted of full thickness skin while not causing any injury of the fascia. Images were taken with two rulers (x- and y-axis), to be able to later evaluate the area of the wounds with Fiji (see section 2.4.5).

Following 30 min waiting time, rats were irradiated either for 7.5 min (10.35 J/cm²), 30 min (41.40 J/cm²) or 60 min (82.80 J/cm²), excluding the control rats. In this set-up, the ENMECH board was used at a power density of 23 mW/cm² and a distance of 5 cm. Control rats were placed on a heating mat to simulate the heat development under the lamp, to keep the conditions as equal as possible. For better air circulation, rats were irradiated in a steel cage (Figure 16).

Figure 16: Irradiation of rats in a steel cage with rigid ENMECH board placed on top. One of the wounds is covered with a lightproof foil.

To test possible systemic effects one of the wounds was covered with aluminum foil during irradiation. To avoid falsifying the data due to anti-bacterial properties of the aluminum foil, the foil itself was covered with Leukosilk, in case it got into contact with the wound. A thermometer was placed under the rat to keep track of the temperature. The heating pad was turned on in case the rat was cooling out as a result of the anaesthesia.

After irradiation 1.5 mL of 0.9% NaCl-solution were injected subcutaneously to compensate for dehydration during anaesthesia. Also an analgesic (Carprofen 5 mg/kg BW) was administered subcutaneously to reduce pain. Carprofen was applied after irradiation due to phototoxicity of the pharmaceutical. After becoming conscious, indicated by first directed movements, wound dressings from URGO RID were applied. A flexible bandage (MaiMed Medical) was added on top of the wound

dressings to keep them in place (Figure 17). 24 h post irradiation blood sampling was performed under isoflurane and images of the wounds were taken again.

Figure 17: Rat with wound dressing from URGO RID and flexible bandage.

For organ collection, rats were deeply anaesthetized with ketamine/xylazin (100 mg/kg, 5 mg/kg) and samples for RNA isolation (for gene expression analyses) were extracted (section 2.4.6). Thereafter the rat was perfused (section 2.4.8).

2.4.2.2 Long-term blue light irradiation of diabetic and non-diabetic rats

For long-term irradiation 12 ZDF fa/fa (obese) and 6 ZDF fa/+ (lean) rats were ordered at the age of 6 weeks. All of the rats were fed a special diet (PMI 5008 mod.), a diet high in proteins and fat. While the lean strain of these rats did not show any effects from this diet, the obese strain developed Type 2 diabetes.

This could be tracked during the induction phase of 6 weeks by increased blood glucose levels, which were measured once to twice a week (section 2.4.3). As soon as the rats had reached the age of 12 weeks, the experiment was started (to be comparable to the previous study: 2.4.2.1 Short-term blue light irradiation of non-diabetic rats). The workflow followed the experimental schedule shown in Figure 18. One day before applying the wounds, another blood glucose measurement was performed and the backs of the rats were depilated. One day later, blood sampling took place. Ketamine/xylazine anaesthesia was applied intraperitoneally and the wounds were created with a biopsy punch. Images were taken after waiting for

30 min, followed by an irradiation with 82.80 J/cm² of blue light at a power density of 23 mW/cm² with the ENMECH board. On day two and three, irradiations with the same dose took place under MMF anaesthesia (Midazolam 0.5 mg/kg, Medetomidine 0.0375 mg/kg, Fentanyl 0.00125 mg/kg). The following three days an irradiation with 41.40 J/cm² of blue light was applied, followed by three days of irradiating with 10.35 J/cm². The last three days only every second day blue light was applied, meaning only on day 11 irradiation took place. With decreasing doses of blue light, and therefore irradiation times, the concentration of MMF anaesthesia was reduced accordingly (half of dose for 41.40 J/cm², quarter of dose for 10.35 J/cm²) for control and irradiated rats equally. Before every irradiation images of the wounds were taken. After irradiation treatment remained as in the previous experiment, meaning Carprofen was applied for a total of 3 days and NaCl solution was injected after each irradiation.
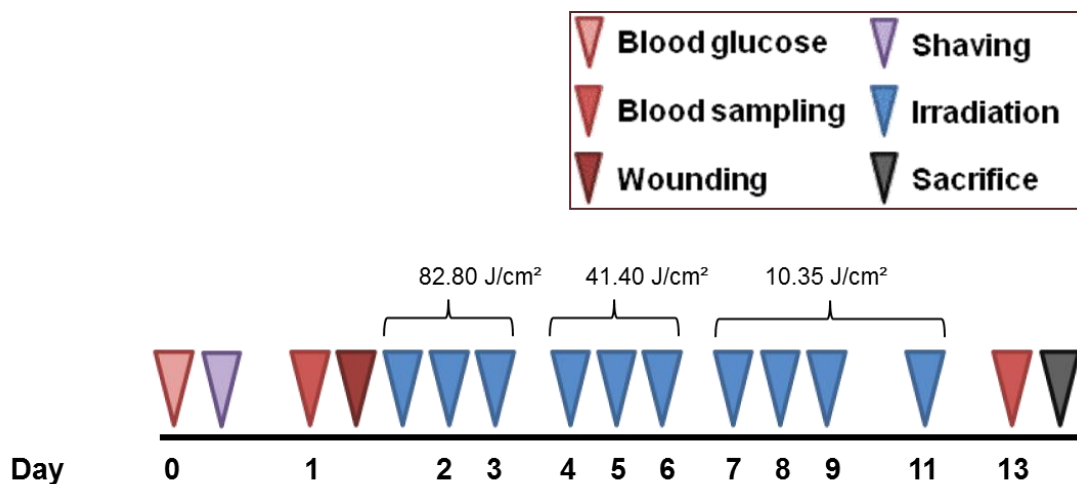
Figure 18: Experimental schedule for long-term irradiation with the ENMECH board.

24 h after the last irradiation retro-orbital blood sampling took place under isoflurane and images of the wounds were taken again. For organ collection rats were deeply anesthetized with ketamine/xylazin and samples for RNA isolation (for gene expression analyses) extracted. Thereafter the rat was perfused (section 2.4.8).

2.4.2.3 Long-term blue light irradiation of diabetic and non-diabetic rats with the MEDILIGHT prototype

For long-term irradiation with the MEDILIGHT prototype the same experimental design was chosen as for the long-term irradiation with the rigid board from ENMECH (Figure 19). Also 12 diabetic rats were used in this experiment, of which 6 animals were assigned to the irradiated group and 6 animals served as the control group. They were irradiated during 12 consecutive days, where only the epidermisation

phase was tested. Hence, irradiation took place only every second day with 10.35 J/cm² of blue light under MMF anaesthesia. Another blood sampling was added in the middle of the experiment, to analyze possible differences immediately after irradiation.
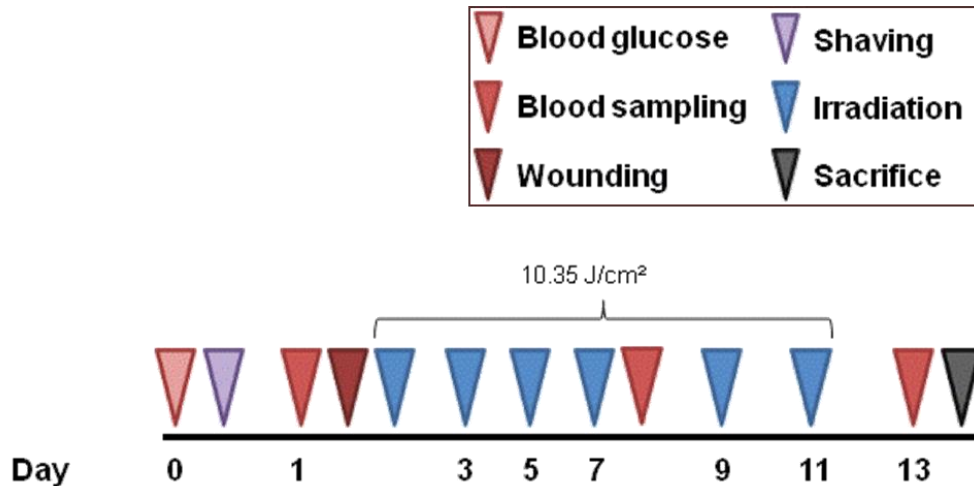
Figure 19: Experimental schedule for long-term irradiation with the MEDILIGHT prototype.

For irradiation the MEDILIGHT prototype was used at a duty cycle of 42%. To meet the requirements of the final product it was irradiated through the wound dressing (Figure 20).
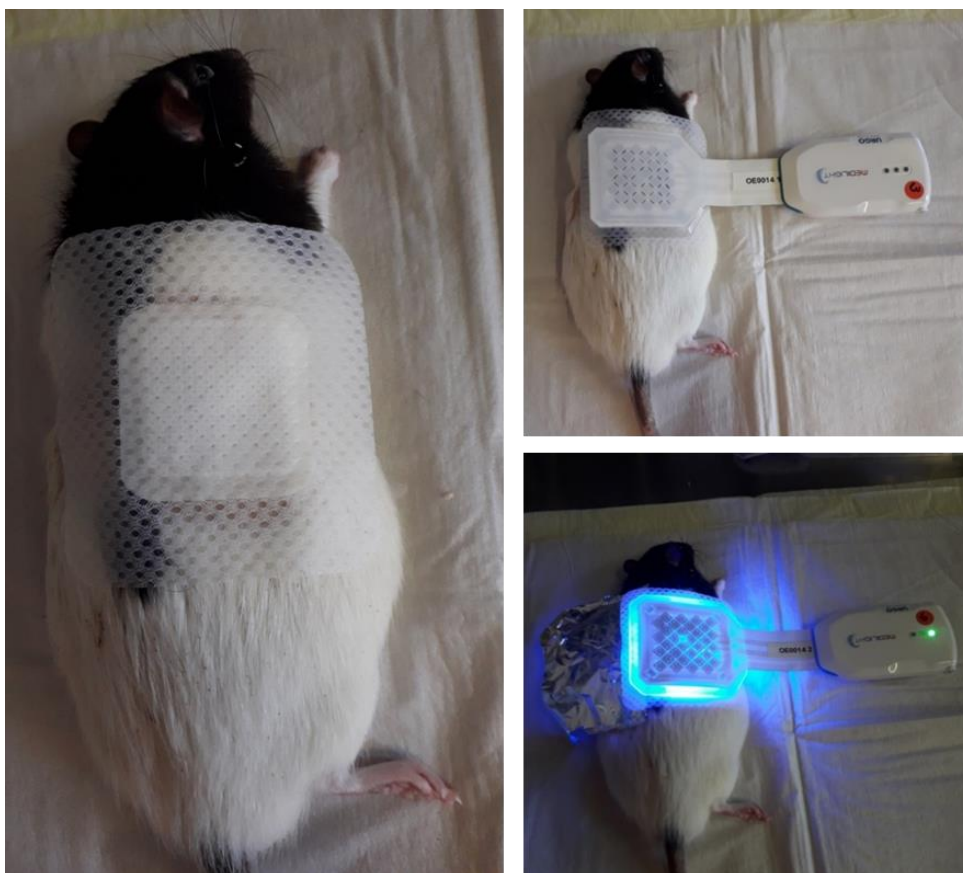
Figure 20: Experimental set-up for blue light irradiation of rats with the MEDILIGHT prototype through the wound dressing. One of the wounds was covered with aluminum foil to test a possible systemic effect.

As the irradiation time was only 7.5 min, concentration of MMF was reduced accordingly. Other sampling procedures remained as described in 2.4.2.1, with retrograde perfusion on the last day.

2.4.3 Blood glucose measurement

For blood glucose measurement, the tails of animals were punctured with a needle. A drop of blood was measured with the glucose test strips and the ACCU-CHEK® Compact Plus blood glucose meter from Roche Diagnostics. The bleeding was stopped by applying pressure with a tissue and the glucose concentrations were noted down.

High glucose concentrations (over 600 mg/dL) were a criterion to exclude animals from the study. If consistently high values occurred, animals were sacrificed before the start of the experiment.

2.4.4 Blood sampling from the retro-orbital venous plexus, plasma separation and analysis of plasma

Blood samples were taken with a glass capillary from the retro-orbital venous plexus. The blood was collected in lithium-heparinized reaction tubes (Sarstedt, Nümbrecht, Germany). Directly after sampling, the blood was distributed evenly in the tube by inverting it. The samples were cooled on ice immediately and centrifuged at 500 rpm for 5 min. By centrifugation the plasma was separated from the erythrocytes. The plasma was placed into a fresh tube while the remains were discarded. Samples were frozen at -80°C until further processing either with the Cobas c 311 analyzer from Roche or in an ELISA kit for C-reactive protein (CRP) from Abcam.

With the Cobas analyzer a full plasma profile (cholesterol, protein, triglycerides) was tested including kidney (urea, creatinine, sodium, potassium, calcium, phosphate) and liver function profiles (Alanine Aminotransferase (ALT), Aspartate Aminotransferase (AST), Glutamate Dehydrogenase (GLDH)).

To test for CRP plasma samples had to be diluted 1:60.000 and the experiment was performed according to the manufacturer's instruction. Triple determination was performed for each sample.

2.4.5 Wound area evaluation with Fiji

Images of wounds were taken every day to be able to compare wound areas between the different groups of an experiment. Images were evaluated with the freehand selection of Fiji, which is an open source image processing package based on ImageJ. With this tool the pixel size could be associated with the rulers, thus allowing to convert the wound area to mm^2 (Figure 21).
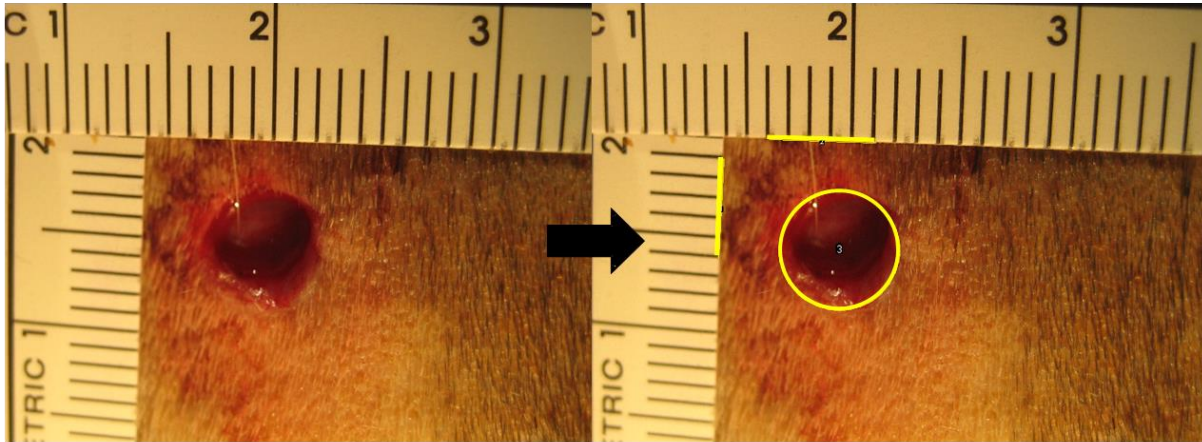
Figure 21: Image processing with Fiji software using the freehand tool to measure wound areas.

2.4.6 Homogenization and RNA extraction from tissue samples

Tissue samples for RNA extraction were taken from both sides of the skin (control and irradiated), including tissue from the wound site. Samples were cut into cubes measuring 1 mm³, snap frozen in liquid nitrogen and stored at -80°C. One of the pre-cut cubes was taken at a time to be homogenized in the Qiagen TissueLyser II. A reaction tube was filled with RLT lysis buffer from RNeasy fibrous tissue mini kit from Qiagen and a steel bead. The reaction tubes were transferred to the Qiagen TissueLyser II and shaken at 30 Hz for 3 min to disrupt the tissue. Every 30 s the reaction tubes were cooled down on ice preventing degradation of RNA. Afterwards RNA was isolated from the homogenized tissue with the RNeasy fibrous tissue mini kit, following the manufacturer's instructions.

For that the homogenized tissue was incubated with protease K for 10 min at 55°C. Then, the RNA was separated from cell debris, DNA and protein by 3 min centrifugation at 10000xg. The upper aqueous phase was transferred into a fresh reaction tube. Adding ethanol to the aqueous phase, it was centrifuged through the spin column, where the RNA bound to a silica-membrane. Genomic DNA was digested with DNase and the membrane washed with RW1 and RPE buffer. Finally

RNA was eluted with RNase-free water from the membrane. In the end the RNA concentration was determined spectrophotometrically by using an Infinite® 200 PRO microplate reader from Tecan Group AG (Männedorf, Switzerland). Here, the A260/A280 ratio was measured and acceptable ratios for samples to be included in experiments were 1.9 to 2.1. Samples were further analyzed by testing the RNA integrity using an Agilent 2100 Bioanalyzer and RNA 6000 Nano Chip.

2.4.7   Gene expression analysis with Affymetrix GeneChips

From 100 ng of isolated RNA, biotinylated antisense cDNA was obtained by using the GeneChip® WT Plus Reagent Kit and the GeneChip® Hybridization, Wash and Stain Kit from Thermo Fisher Scientific. Then, cDNA was fragmented and labeled to be hybridized onto GeneChip® Rat Genome 230 2.0 microarrays with an incubation time of 16 h at 45°C. For gene expression profiling, chips were dyed in a GeneChip® Fluidics station 450 and scanned with a GeneChip® Scanner 3000, both obtained from Affymetrix.

Custom CDF version 18 with ENTREZ based gene definitions was used for annotation. Applying quantile normalization and RMA background correction, the raw fluorescence intensity values were normalized. Based on OneWay-ANOVA, differential gene expression was analyzed using a commercial software package: JMP Genomics, version 7, from SAS Institute. A false positive rate of a = 0.05 with FDR correction was defined as the level of significance.

Gene set enrichment analysis (GSEA) was performed to determine whether defined lists (or sets) of genes exhibit a statistically significant bias in their distribution within a ranked gene list (see http://www.broadinstitute.org/gsea). Pathways belonging to various cell functions were obtained from the public database KEGG.

2.4.8   Retrograde Body Perfusion

As preparation for the retrograde perfusion heparinized saline and 4% PFA were prepared and pH adjusted to 7.4. The solutions were filled into perfusion bottles and the tubes were connected to a compressor. Then, the compressor was started and the pressure adjusted to 280 mbar.

The abdomen of the animal was opened. The organs were pushed aside with a swab and the aorta and *vena cava* were located and dissected from surrounding tissue. A butterfly needle, connected to the perfusion bottles, was inserted into the aorta near

the kidney vessels and clamped. The *vena cava* then was cut. The animal was flushed with heparinized saline for 3 min followed by flushing with 4% PFA for additional 3 min. Finally organs were collected.

2.4.9 Sample collection and processing for evaluation of histology

Organs that were removed from the perfused animals were cut into axial slices with a thickness of around 5 mm. After fixation in 4% PFA for 24 h, they were stored in diluted 2% PFA. Then, they were dehydrated in the automatic tissue processor TP1020 Leica Biosystems and embedded in paraffin. From these paraffin blocks slices with a thickness of 3 µm were cut with a semi-automated rotary microtome from Leica Biosystems. After fixation in a heat chamber for 1 h at 60°C they were stained with hematoxylin and eosin (H&E) in the Leica Biosystems Autostainer XL. Finally, they were covered with Eukitt and sealed with a cover slip.

The histology slides were imaged with the Axio Scan.Z1 microscope from Carl Zeiss using a 40x objective. To analyze morphological structures, images were exported from the ZEN software (Carl Zeiss) and segmented into different classes (inflammatory site, fibrin, leukocytes, and epidermis) with the ilastik software. The segmented images were quantified by pixels in ImageJ with the Countpix macro. The areas of the classes were determined in pixels and transferred to mm² through the resolution of the image.

2.5 EU project MEDILIGHT: prototype temperature testing on a skin polymer mode and pigs

During development of the MEDILIGHT prototype, 5 temperature sensors (one in the center, 4 on each corner) were integrated into the flexible LED foil. They were added to track the heat build-up caused by the LEDs as a safety measure to later avoid burns on the patient's skin. The efficacy of these sensors had to be tested and verified. As initial experiments, the sensors were tested on a skin model consisting of a dyed gelatin polymer provided by Laboratoires URGO S.A. To imitate the human body temperature, the polymer was placed on a ThermoStat Plus heat block from Eppendorf and was heated to 35°C. As reference, two external sensors were placed on top of the polymer, one sensor in the center and one on the rim. To be in line with the final set-up, the wound dressing E2723 from URGO, followed by the flexible LED foil and the pocket, were added. While the prototypes were changing (flexible LED

foil, back reflector, silicone encapsulation, wound dressing, pocket), the set-up remained the same (compare Figure 22).

Figure 22: Experimental set-up for temperature measurements on skin polymer model with MEDILIGHT prototypes.

The temperature was tracked over 1 hour by the sensors placed on the prototype as well as by the external sensors, while the LEDs of the MEDILIGHT prototype were switched on.

For the prototype the MEDILIGHT App V2.5 for Android was used on a Samsung Galaxy J3 DUOS smartphone to track and store the data via Bluetooth. The external temperature sensors were driven by Thermocouple Data Logger USB TC-08 from Pico Technology and the data transmitted via USB to a computer. To track and save the data the PicoLog 6 data logging software from Pico Technology was used.

While the MEDILIGHT prototype was developed, the software was updated continuously. New features were integrated into the software such as the possibility to regulate irradiation cycles with breaks in between. Also on/off times of the LEDs in relation to a definable minimum or maximum temperature could be adjusted. With these safety measures it was possible to define a maximum temperature where the LEDs of the flexible foil were turned off automatically. This gave the opportunity to test the efficacy of the MEDILIGHT prototype on the skin of Aachen minipigs with the permission number G-78/18. Male Aachen minipigs (Heinrichs Tierzucht, Heinsberg, Germany) were used, weighting around 25 kg. The experimental set-up on the flank of the pig is displayed in Figure 23.
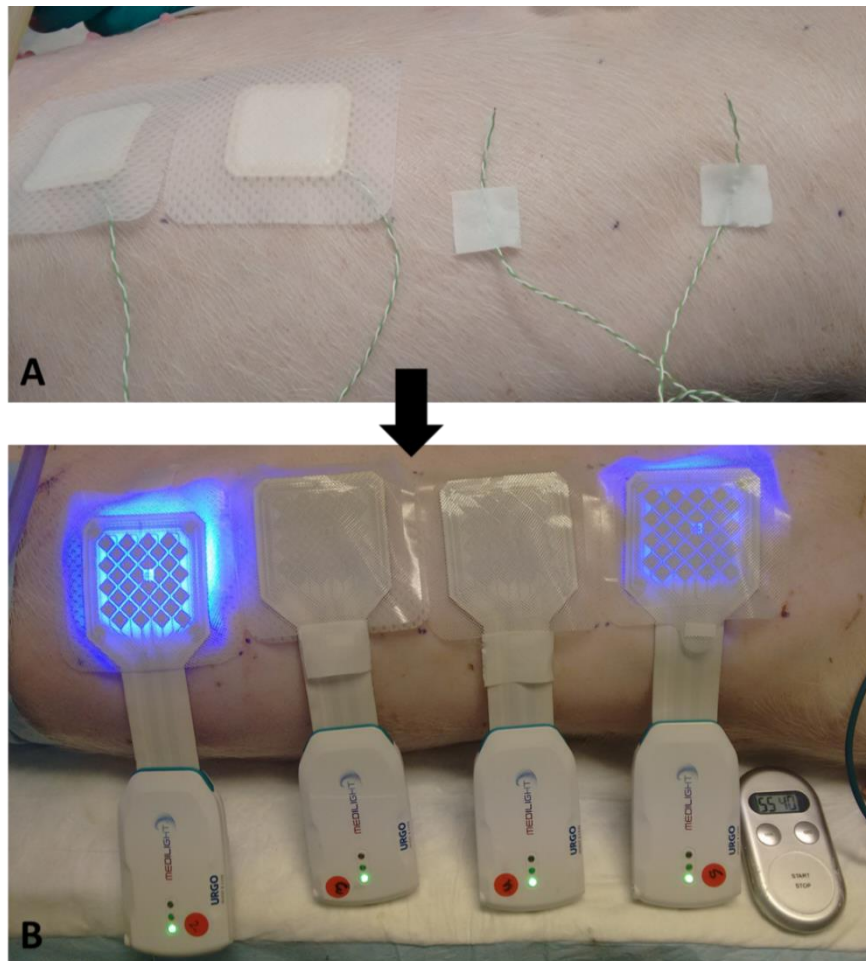
Figure 23: Set-up for experiments on pigs with four MEDILIGHT prototypes. The external sensor was placed directly on the skin surface, partially with the wound dressing E2723 included.

Four external sensors were placed directly in contact with the skin, to track the surface temperature (Figure 23 A). Two of these prototypes were placed on the wound dressing E2723 to test the differences for each condition on the heat-build up. When involving the wound dressing in the experiments, the irradiance, and therefore the duty cycle, of the prototype had to be increased to make up for the loss of power by the additional layer. This led to a higher power input which subsequently could result in an increased build-up of heat.

The MEDILIGHT prototypes were fixed with the pockets (Laboratoires URGO) on top of the wound dressings and external sensors (Figure 23 B). Two of the four prototypes were used to track the heat build-up, one with the wound dressing and one without, respectively, during irradiation. Both of these prototypes were adjusted to have an irradiance of 23 mW/cm² on the surface of the skin. They were run not only run in continuous but also in cycled mode, turning off at a maximum temperature of 40°C and turning on at a minimum temperature of 37°C. The other two prototypes tracked the temperature to obtain a reference measurement.

The experiment was carried out for a period of 1 hour. Data from the 5 sensors of the MEDILIGHT prototypes was tracked with the MEDILIGHT App via Bluetooth. For the external sensors, data was recorded with the PicoLog 6 data logging software. As a maximal tolerable temperature on the skin surface it was decided to use a threshold of 40°C. An external sensor was used to track the temperature on the skin surface as well. For the first test on porcine skin it was possible to do point measurements every 5 min only.

For all experiments measurements were set into relation to each other, comparing the differences between the temperatures observed on the surface of the skin and on the flexible LED foil. The on/off times were recorded and key cycles were used for *in vitro* testing to verify the effectiveness of the cycled mode. Possible impacts of the temperature on the porcine skin were controlled by visual comparison with untreated skin. Additionally, tissue from the experimental sites was extracted and analyzed by histology, fixating the skin samples at RT in 37% formalin and following the procedure described in 2.4.9.

2.6   Statistical analyses

All statistical analyses were done with JMP Genomics, version 7, from SAS Institute. The distribution analysis was used to determine whether the data is normally distributed. For that the normal quantile plot and the normal distribution curve was used to compare the eccentricity of the data points and a Goodness of Fit test (Shapiro-Wilk W test) was applied. For small p-values the H0 hypothesis, where the data would be normally distributed, was rejected.

For normally distributed data the Students t-test was applied; for others the non-parametric Wilcoxon signed-rank test was used. Statistical significance was defined as $p < 0.05$.

3   RESULTS

3.1   *In vitro* and *in vivo* testing of blue light irradiation on different skin models

The effects of blue light irradiation were tested with different *in vitro* skin models, which are described in the following chapters.

3.1.1   Irradiation of co-cultures with blue light

Keratinocytes and fibroblasts were irradiated with different doses of blue light in a co-culture set-up and XTT performed after separating the cells in 96-well plates. In Figure 24 not only the results with 41.40 J/cm² of blue light from previous work [89] are shown, but also the addition of 10.35 J/cm².
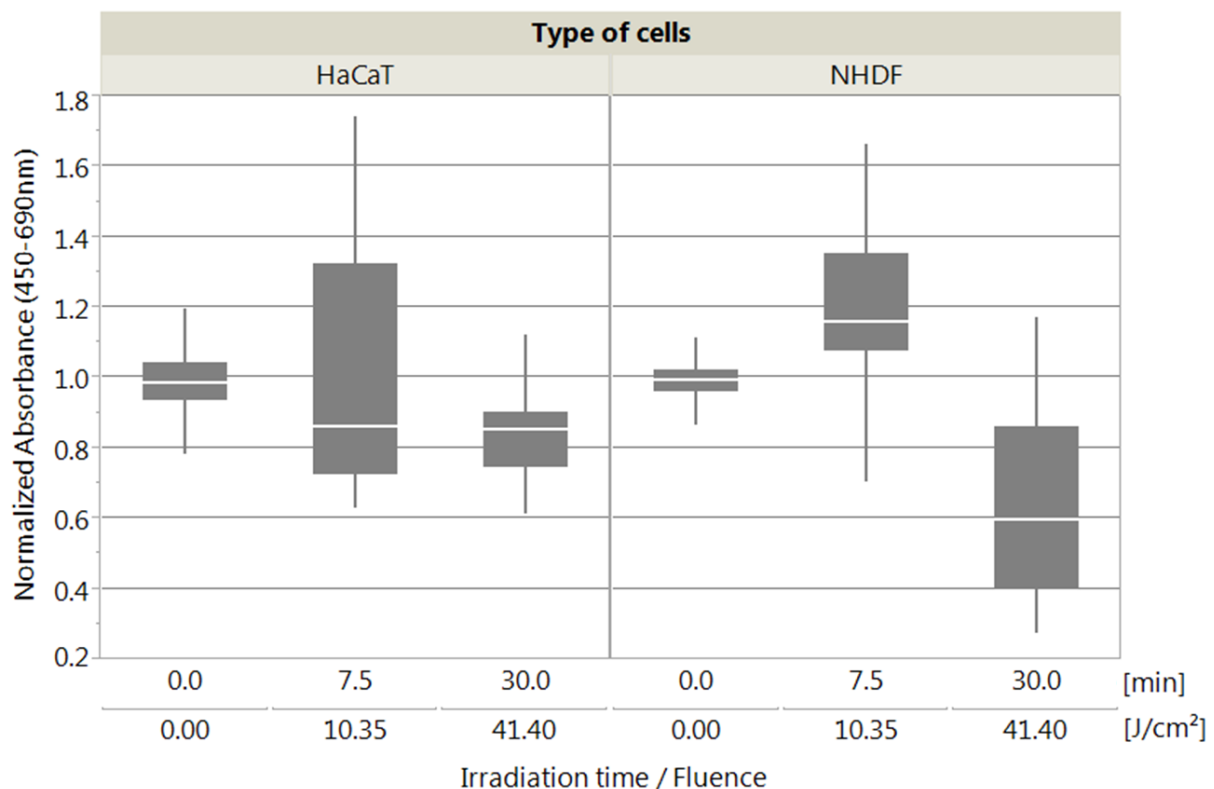
Figure 24: XTT assay results for keratinocytes and fibroblasts from co-cultures treated with 10.35 and 41.40 J/cm² of blue light using the Philips lamp. Assay was performed 24 h after irradiation. Data are shown as box plots with the median, upper and lower quartile (interquartile range (IQR)) and whiskers (1.5 x IQR). Each box plot represents n=3 repetitions.

For keratinocytes doses of 10.35 J/cm² as well as 41.40 J/cm² of blue light lead to a decrease of metabolic activity to around 0.85 compared to the control, where the results for 10.35 J/cm² have a high degree of variation. For the lower dose of blue light the results are not significant (p = 0.8307), but for 41.40 J/cm² they are

significant (p < 0.0001). Fibroblasts irradiated with 10.35 J/cm² of blue light on the other hand show an increase of metabolic activity to 1.15 (p < 0.0001) compared to the control. A dose of 41.40 J/cm² of blue light on fibroblasts leads to a decrease of metabolic activity to 0.6 (p < 0.0001) compared to the control.

Due to the high variance and only partial significance of these experiments, it was decided to take a different approach on *in vitro* skin models.

3.1.2 Irradiation of mixed cultures with blue light

As experiments on co-cultures did not result in stable results, it was decided to test the overall metabolic activity of both cells in a mixed culture. The main fluences of 10.35 J/cm² and 41.40 J/cm² were tested in an XTT assay (Figure 25).
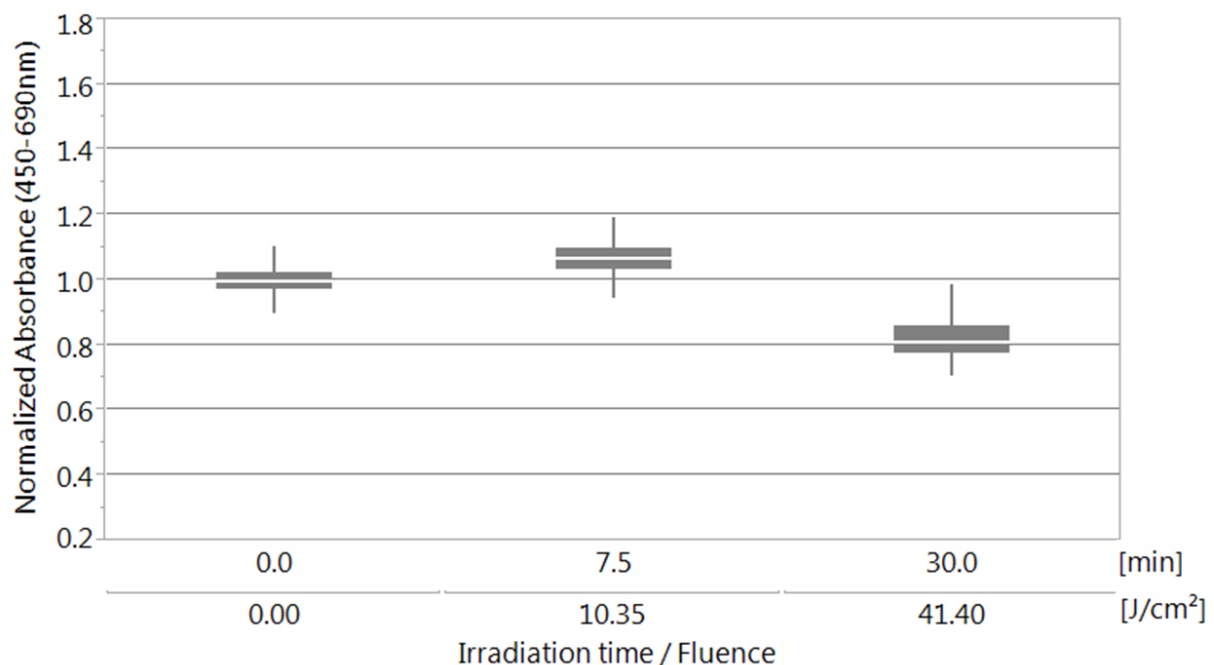
Figure 25: XTT assay results of mixed cultures treated with 10.35 and 41.40 J/cm² of blue light using the Philips lamp. Assay was performed 24 h after irradiation. Data are shown as box plots with the median, upper and lower quartile (interquartile range (IQR)) and whiskers (1.5 x IQR). Each box plot represents n=3 plates with 5 repetitions.

The experiment revealed an increase in metabolic activity to 1.05 after irradiation with 10.35 J/cm² and a decrease to 0.80 with 41.40 J/cm² with p-values < 0.0001 for both conditions.

3.1.3 Scratch wound healing assays

To confirm results of XTT assays, scratch wound healing assays were performed. While results for the XTT assays give information on metabolic activity, the scratch assay reveals changes in migration and proliferation of cells. First, experiments were

performed for mono-cultures of the respective cell lines individually and in a second step, cells were cultivated together and tested again in a mixed culture model.

3.1.3.1 Scratch wound healing assays of fibroblasts

In initial experiments, different cell concentrations (45,000; 60,000; 75,000 cells/well) were seeded to investigate the optimal values for this set-up (data not shown).

The cell concentration of 60,000 cells/well led to the most stable results with a linear decrease in scratch size and a relatively small standard deviation, compared to other seeding concentrations. Therefore, the cell concentration of 60,000 cells/well and an incubation time of 48 h was chosen for the following experiments.

Images were acquired at different time points after scratching, to narrow the time intervals required for evaluation. In Figure 26 exemplary images are shown, taken at 0, 12, 15, 18, 21 and 24 h. Most cell proliferation takes place between 12 and 18 h, meaning that a time interval of 3 h between image acquisitions is not specific enough and had to be decreased.
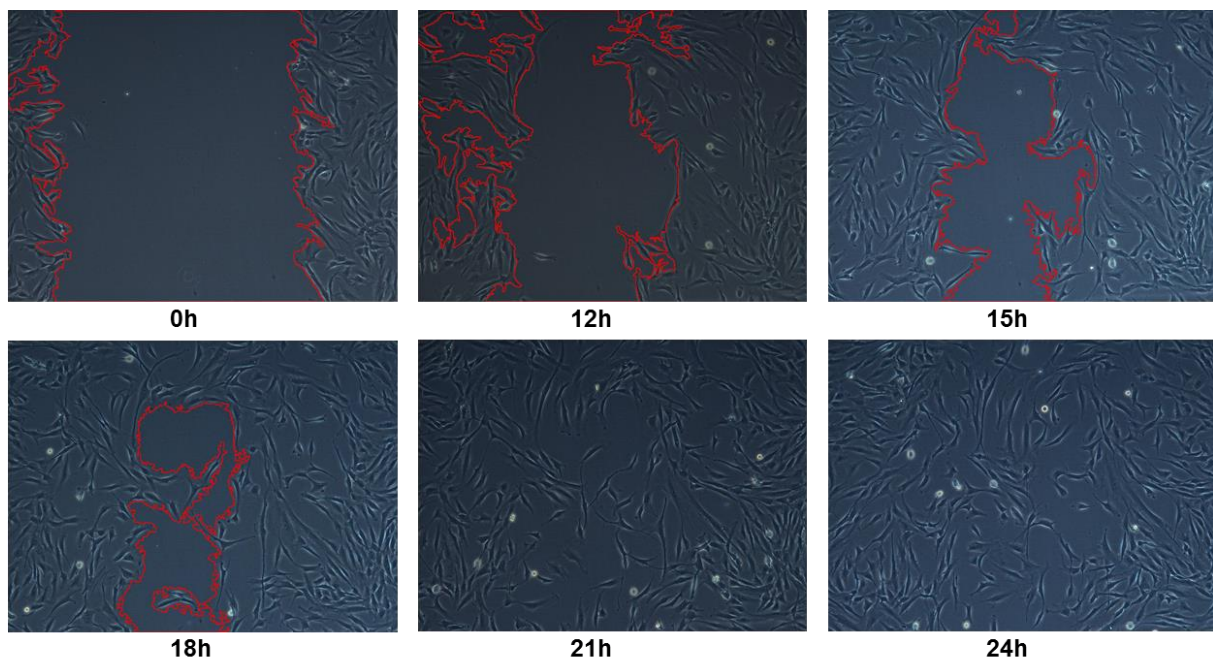
Figure 26: Exemplary microscopic images of fibroblasts seeded at a concentration of 60,000 cells/well with images taken at 0, 12, 15, 18, 21 and 24 h after creating the artificial wound. Evaluation was done with the AutoScratchSeg program.

To be able to take images with shorter intervals, the IncuCyte system was used. Here, it was possible to acquire images while leaving cell culture plates in the incubator and without stressing them. Images were taken at a time interval of 1 hour and results where cells were irradiated with 10.35 J/cm² of blue light are shown in Figure 27.
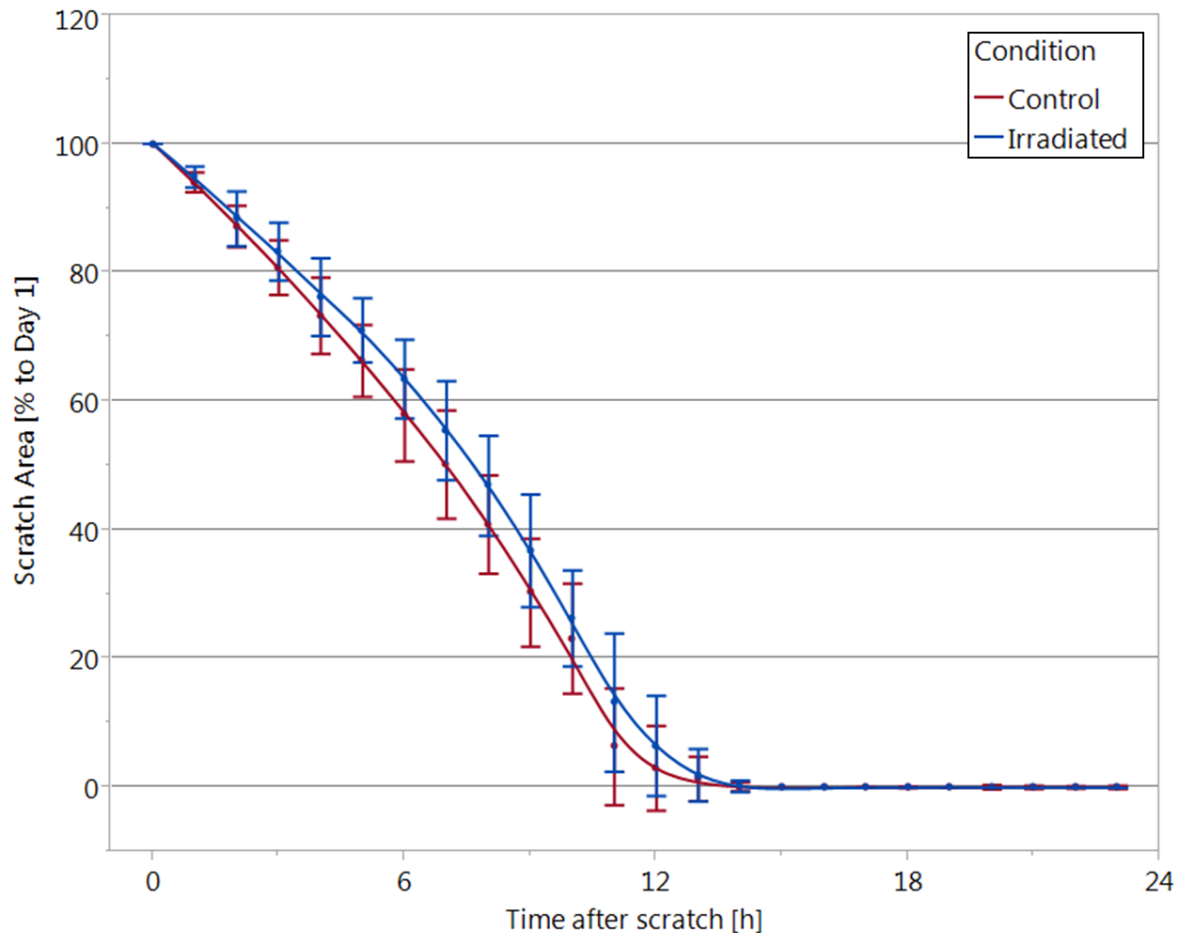
Figure 27: Scratch assay results of NHDF cells treated with 10.35 J/cm² (7.5 min) of blue light. Evaluation of microscopic images was done every hour from 0 up to 23 h after the scratch and compared to the initial wound size (100%). Images were analyzed using the AutoScratchSeg program. Data are shown as means ± SD from three independent experiments with n=3 per condition and 24 images per plate.

Differences can be seen already 1 hour after the scratch, where control cells close the artificial wound significantly faster than irradiated cells. This effect holds until time point 12 h ($p < 0.05$, 2 h and 10 h not significant). Differences between irradiated and control cells amount to 1 to 7%. Afterwards the wound sizes are nearly identical again and wounds are closed completely at time point 15 h for both conditions. All in all blue light irradiation with a dose of 10.35 J/cm² leads to a disadvantage of 1 h regarding wound closure.

The same experiment was performed for NHDF cells, but irradiation with a dose of 41.40 J/cm² of blue light took place (Figure 28).
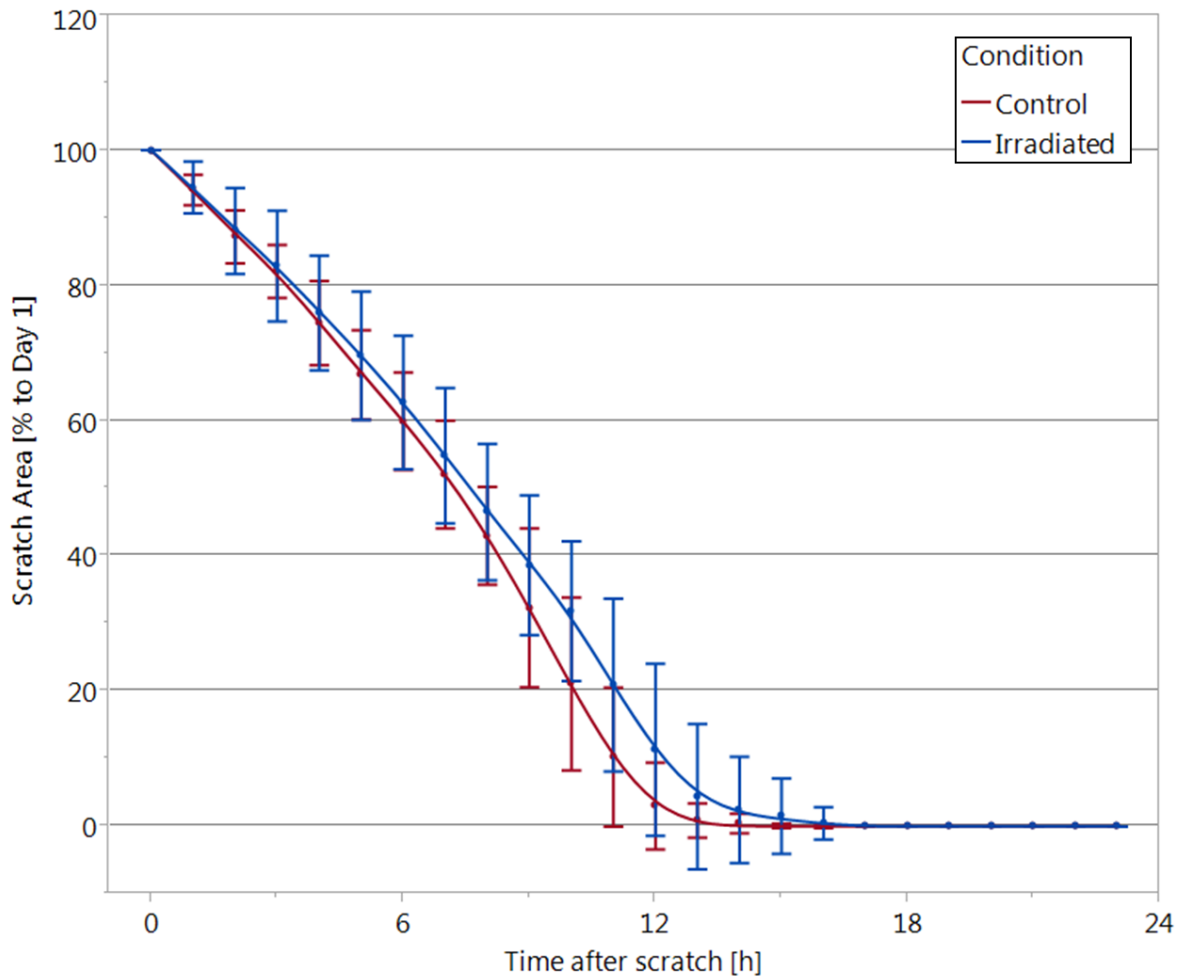
Figure 28: Scratch assay results of NHDF cells treated with 41.40 J/cm² (30 min) of blue light. Evaluation of microscopic images was done every hour from 0 up to 23 h after the scratch and compared to the initial wound size (100%). Images were analyzed using the AutoScratchSeg program. Data are shown as means ± SD from three independent experiments with n=3 per condition and 24 images per plate.

At the beginning of the experiment, only small differences can be seen. The artificial wound is closing linearly for both conditions in the first 8 h. After this time point the control cells continue closing the empty space linearly. In contrast to that, irradiated cells reduce this behavior. This can be seen from time points 9 to 12 h, indicated by significant differences ($p < 0.05$) of 6 to 10%. Afterwards, irradiated cells and control cells have the same wound sizes again without statistical significance. Artificial wounds are closed completely at time point 13 h for control cells, while irradiated wounds stay open until 16 h. This presents a difference of 3 h.

3.1.3.2 Scratch wound healing assays of keratinocytes

Scratch wound healing assays were also performed with mono-cultures of keratinocytes. For initial experiments different cell numbers were seeded, where 300,000 cells/well and a cultivation of 24 h were chosen as the optimal parameters. Exemplary images are shown in Figure 29.
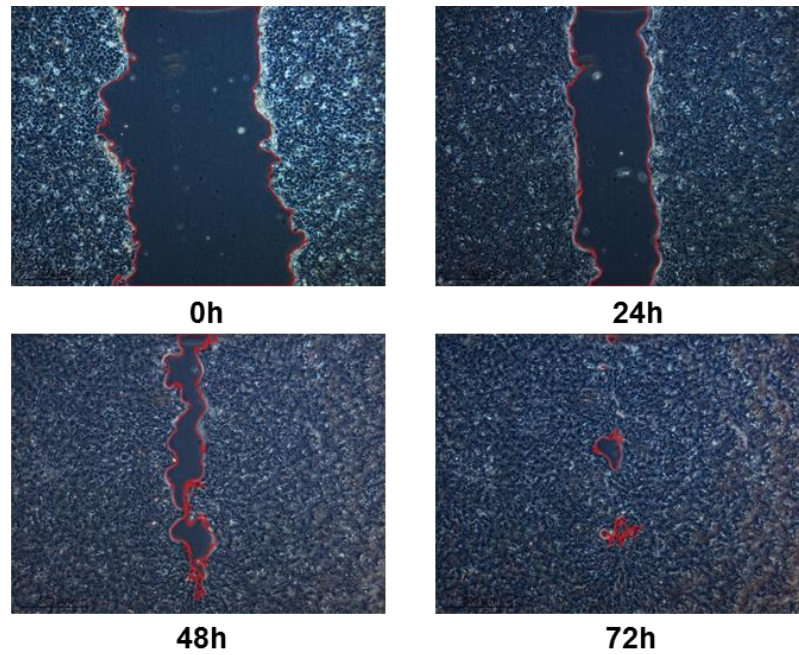
Figure 29: Exemplary microscopic images of keratinocytes seeded at a concentration of 300,000 cells/well at time points 0, 24, 48 and 72 h after creating the artificial wound and evaluated with AutoScratchSeg.

Effects of 10.35 J/cm² of blue light on HaCaT cells are shown in Figure 30.
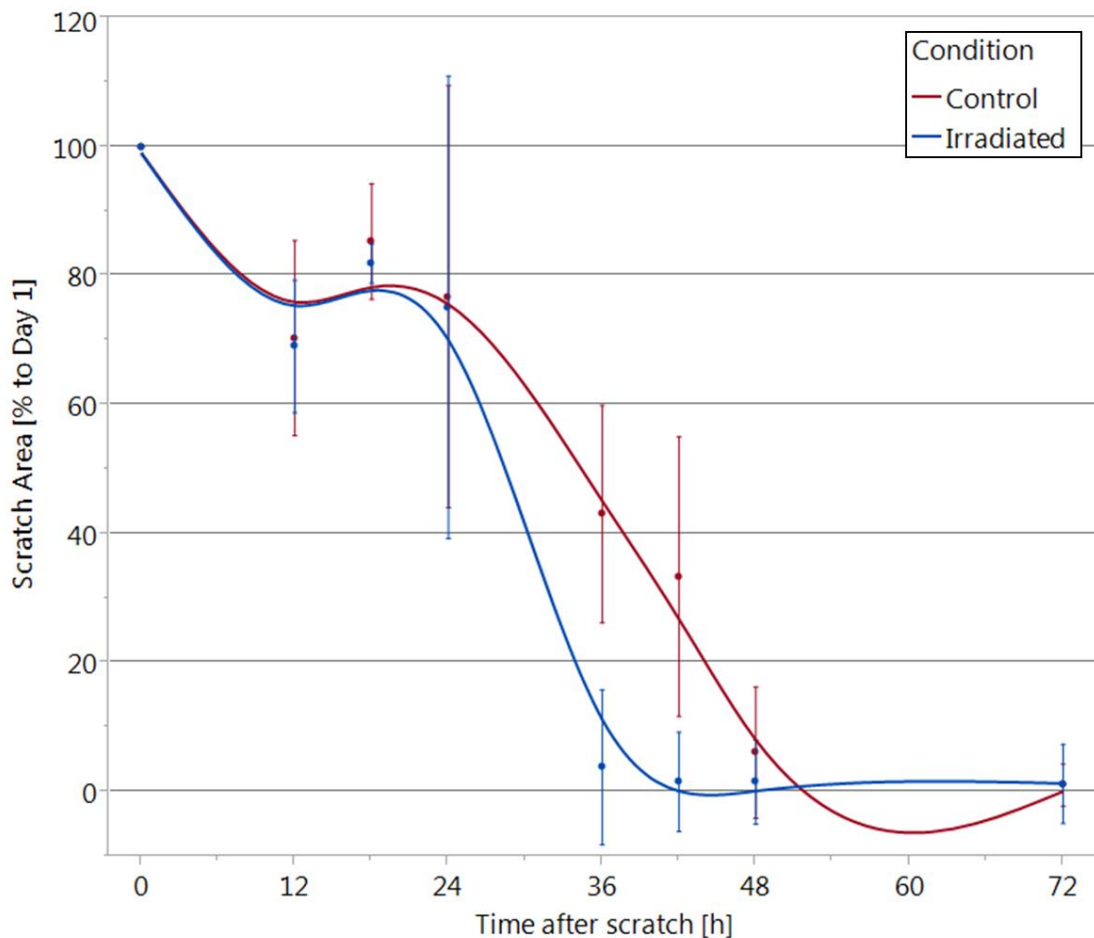
Figure 30: Scratch assay results of HaCaT cells treated with 10.35 J/cm² (7.5 min) of blue light. Evaluation of microscopic images was done at different time points (0, 12, 18, 24, 36, 42, 48 and 72 h) after the scratch and compared to the initial wound size (100%). Images were analyzed using the AutoScratchSeg program. Data are shown as means ± SD from three independent experiments with n=3 per condition and 24 images per plate.

For time points 0 and 12 h there are no significant differences between irradiated and control HaCaT cells. First effects can be seen at time point 18 h, where irradiated wounds are significantly ($p < 0.05$) smaller by 3%. At the 24 hour time point, wounds have nearly the same size again. Throughout the following time points at 36, 42 and 48 h wound sizes differ significantly ($p < 0.0001$) again, where irradiated HaCaT cells close wounds faster compared to the control. At time point 72 h both wounds are closed completely. The difference between irradiated and control cells amounts to around 9 h.

The same experiment was performed for HaCaT cells with a dose of 41.40 J/cm² of blue light (Figure 31).
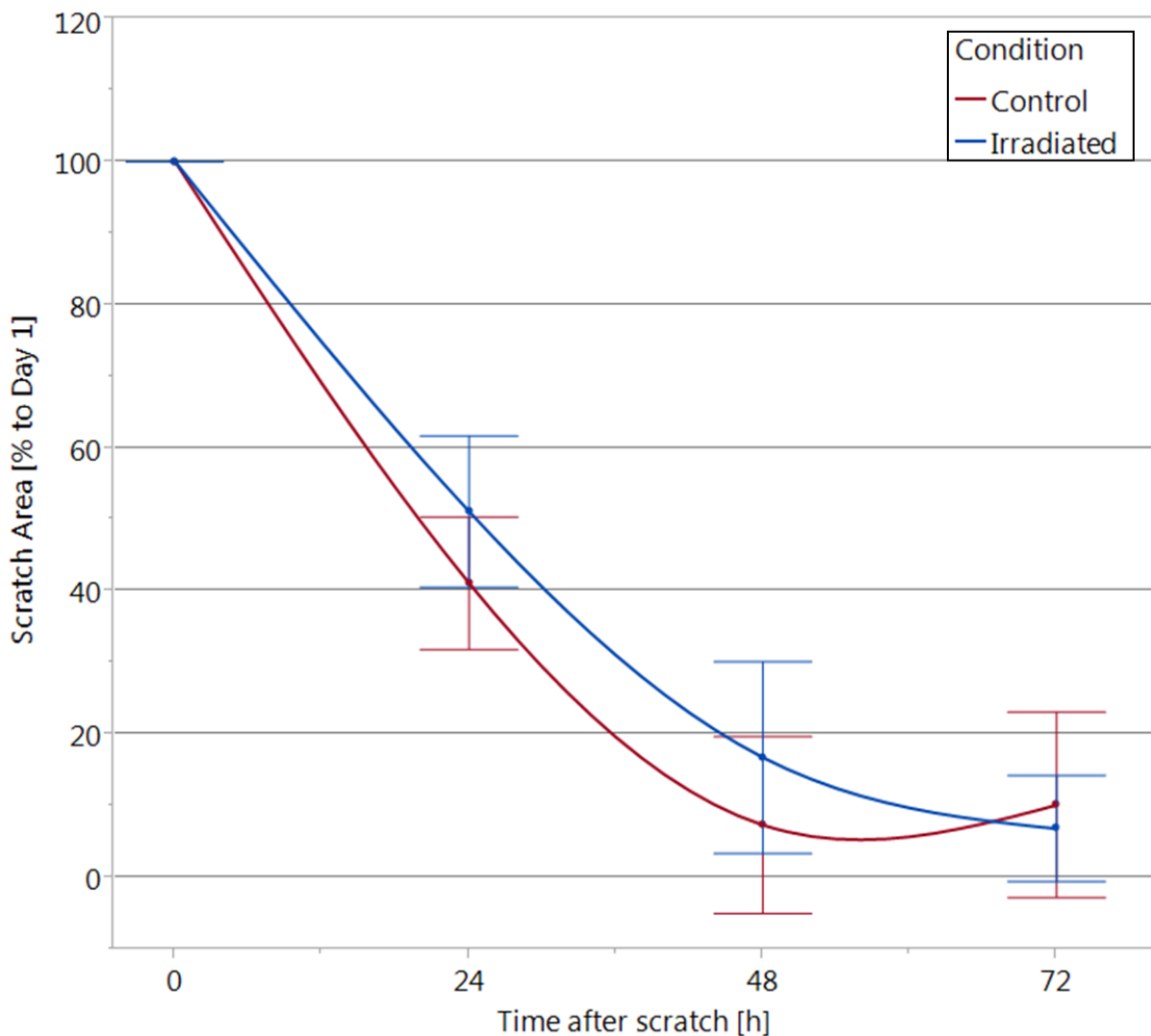


Figure 31: Scratch assay results of HaCaT cells treated with 41.40 J/cm² (30 min) of blue light. Evaluation of microscopic images was done at different time points (0, 24, 48 and 72 h) after the scratch and compared to the initial wound size (100%). Images were analyzed using the AutoScratchSeg program. Data are shown as means ± SD from three independent experiments with n=3 per condition and 24 images per plate.

The results demonstrate significant differences ($p < 0.0001$) between irradiated and control cells at 24 and 48 h. The differences between the means of the curves amount to 10%, respectively for both time points. At time point 72 h after the scratch, the curves exhibit the same wound area with around 10% of the wound still open. Therefore the delay of wound closure adds up to 24 h.

3.1.3.3 Scratch wound healing assays on mixed cultures

To test whether wound healing properties change for keratinocytes and fibroblasts when cultivated together mixed cultures were seeded and the influence of blue light irradiation was investigated.

First, different cell numbers were tested and the optimal cell concentration was determined (Figure 32). Cell concentrations were seeded with equal amounts of keratinocytes and fibroblasts, respectively. To reach confluence, a concentration of 90,000 cells/well in total (HaCaT and NHDF cells) was required.
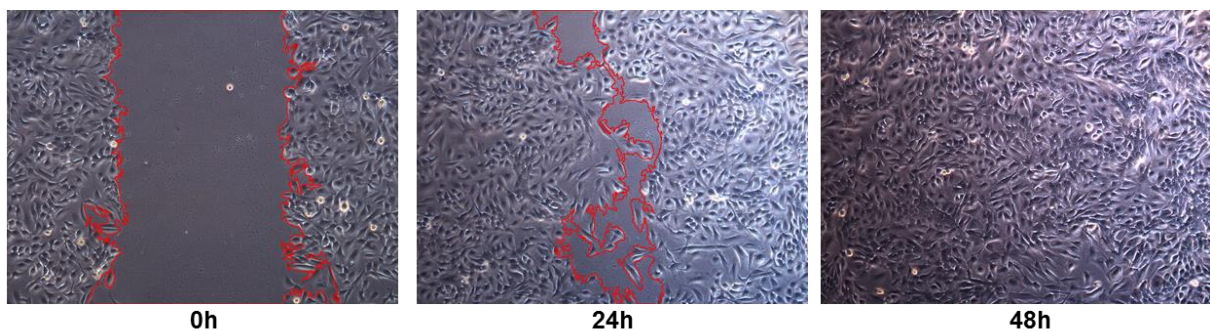
Figure 32: Exemplary microscopic images of mixed cultures seeded at a concentration of 90,000 cells/well with images taken at 0, 24 and 48 h after creating the artificial wound. Evaluation was done with the AutoScratchSeg program.

After determining the optimal cell number, a treatment of 10.35 J/cm² of blue light was applied. Images were taken at 0, 24, 48 and 72 h. Results of artificial wound sizes are displayed in Figure 33.

24 h after the scratch and irradiation, wound sizes stay the same for control and irradiated cells at 93%. At 48 h post irradiation, a significant difference can be seen, where the gap size of control cells is at 91% while irradiated wounds are closed to 76% ($p < 0.0001$). After 72 h the wound sizes are approximately of the same size again with 80% for control and 85% for irradiated cells. In total, with an irradiation of 10.35 J/cm², an advantage in wound closure of 24 h can be achieved.
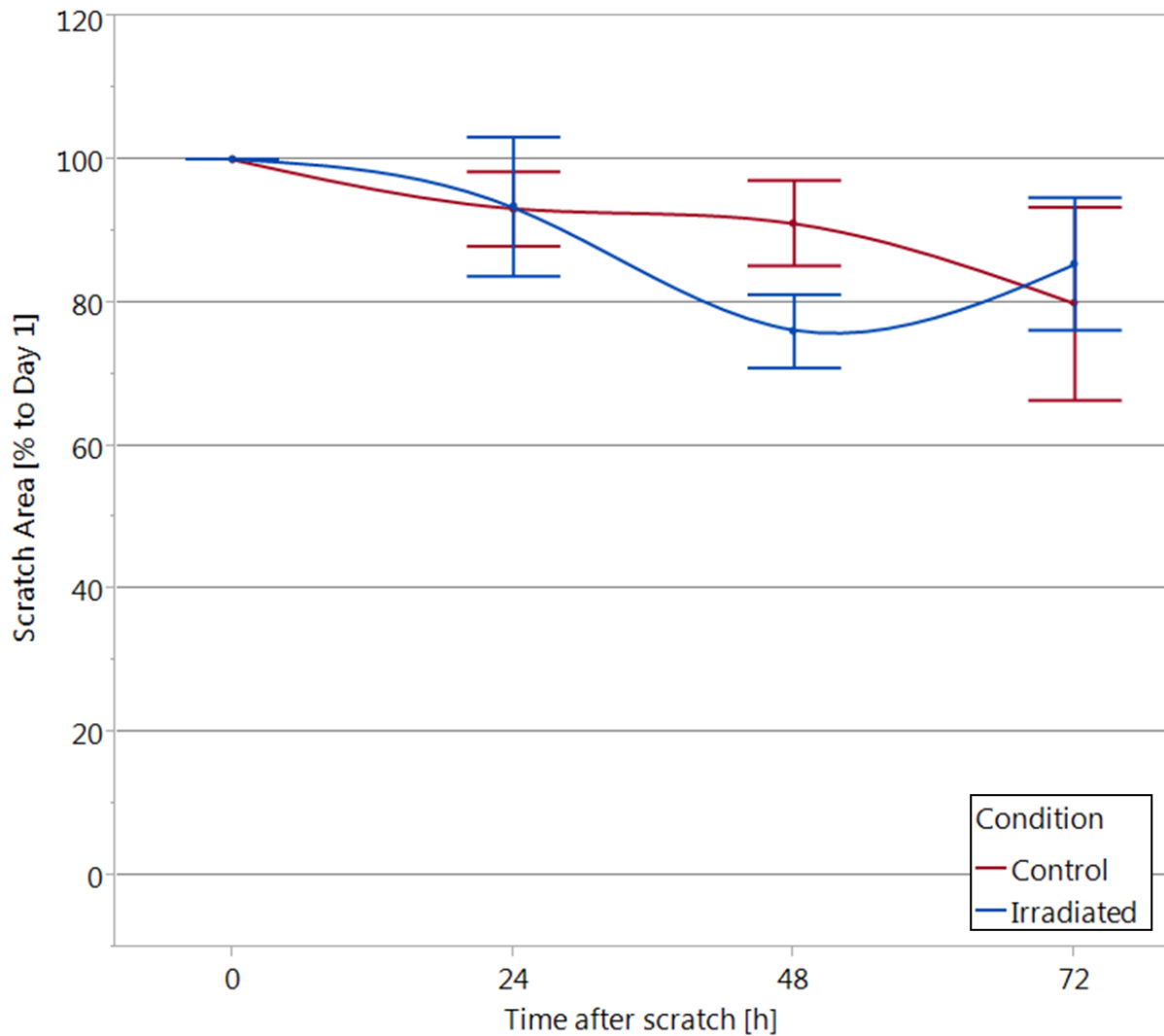
Figure 33: Scratch assay results of mixed cultures treated with 10.35 J/cm² (7.5 min) of blue light. Evaluation of microscopic images was done at different time points (0, 24, 48 and 72 h) after the scratch and compared to the initial wound size (100%). Images were analyzed using the AutoScratchSeg program. Data are shown as means ± SD from three independent experiments with n=3 per condition and 24 images per plate.

An irradiation with a dose of 41.40 J/cm² was tested (Figure 34). Images were compared at time points 0, 24 and 48 h.

Significant differences were noted. For the control the wound closes linearly from time point 0 until 48 h. At 48 h after the scratch was performed, the artificial wound area is reduced by 30% of the initial size. In contrast to that, the wound area of the irradiated cells stays open at 100% over the whole time course. Differences are significant for both 24 and 48 h after the scratch (p < 0.0001). This shows an effect of blue light not only on the migration, but also on the proliferation of cells.
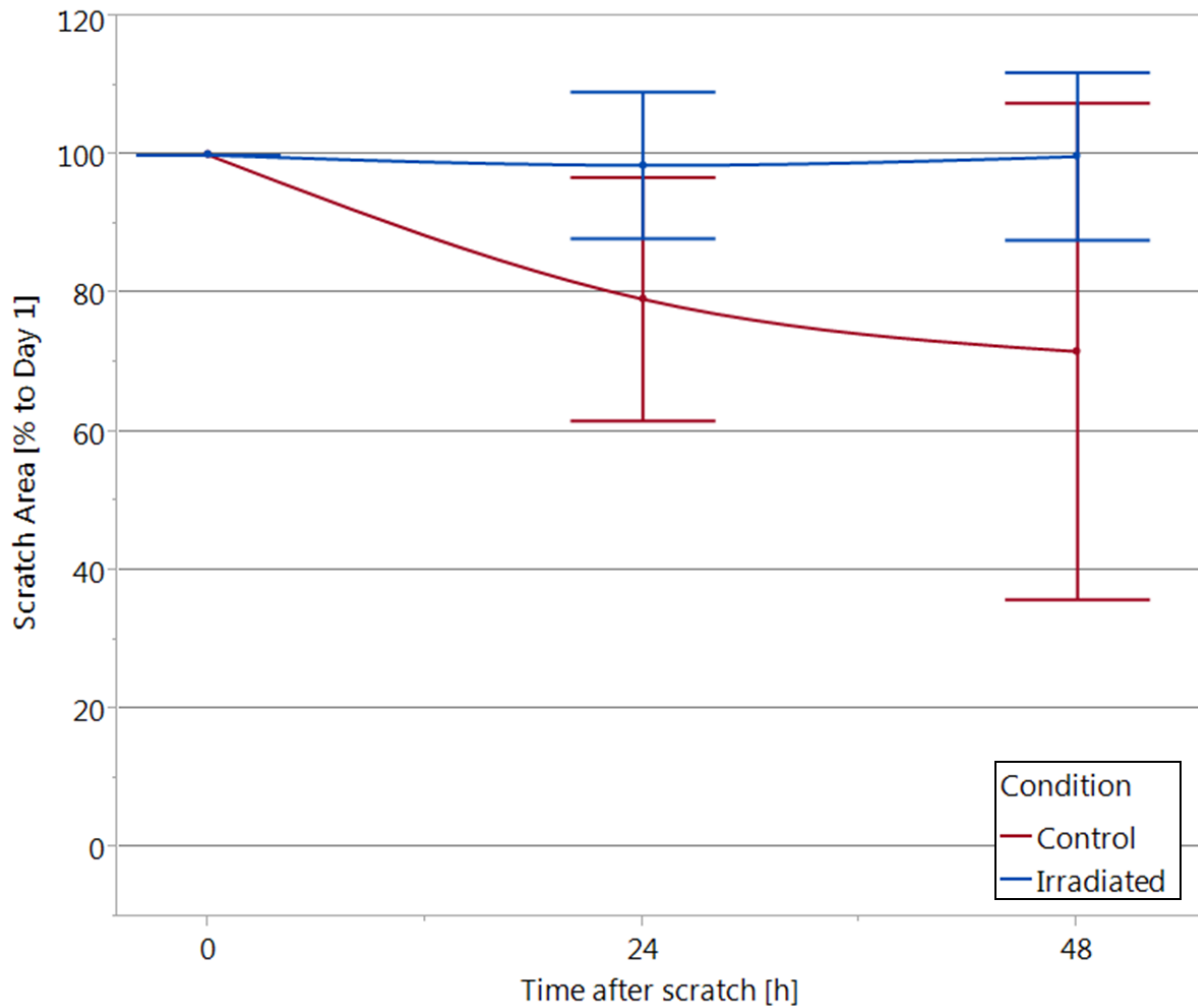
Figure 34: Scratch assay results of mixed cultures treated with 41.40 J/cm² (30 min) of blue light. Evaluation of microscopic images was done at different time points (0, 24 and 48 h) after the scratch and compared to the initial wound size (100%). Images were analyzed using the AutoScratchSeg program. Data are shown as means ± SD from three independent experiments with n=3 per condition and 24 images per plate.

3.1.4 Short-term irradiation of non-diabetic rats with ENMECH board

To analyse effects of the different doses identified for different wound healing stages *in vivo*, first, the individual fluences were tested on non-diabetic rats. For later comparison, reference values were measured for blood glucose concentrations of the healthy rats. Mean values for the glucose concentration is 137 mg/dL and the standard deviation accounts to 10 mg/dL.

Plasma samples were collected processed with the Cobas c 311 analyzer. Full kidney and liver profiles were tested as well as CRP (Table 6).

Table 6: Plasma parameters of non-diabetic rats (ZDF fa/+) irradiated with different fluences of blue light.
Baseline (n=24) was created from plasma samples taken before the experiment was started. Plasma samples for irradiated rats were taken 24 h post-irradiation (n=6 for each group respectively). Data are expressed as means ± SD. Values significantly different from the baseline are indicated as *$p < 0.05$, **$p < 0.01$.

Parameter	Baseline	Fluence [J/cm²]			
		0.00	10.35	41.40	82.80
ALT [U/L]	35 ± 14	52 ± 34	22 ± 15	34 ± 21	37 ± 9
AST [U/L]	78 ± 16	221 ± 184*	141 ± 52**	148 ± 116*	125 ± 33**
Calcium [mmol/L]	2.68 ± 0.08	2.65 ± 0.05	2.62 ± 0.09	2.68 ± 0.06	2.66 ± 0.05
Cholesterol [mg/dL]	102 ± 8	93 ± 2*	92 ± 2**	90 ± 8*	94 ± 6*
Creatinine [mg/dL]	0.28 ± 0.04	0.26 ± 0.03	0.30 ± 0.04	0.24 ± 0.05	0.25 ± 0.02
GLDH [U/L]	9.72 ± 6.59	7.75 ± 2.23	8.55 ± 1.90	7.98 ± 1.70	10.17 ± 1.64
Potassium [mmol/L]	4.67 ± 0.35	4.60 ± 0.19	4.56 ± 0.13	4.90 ± 0.63	4.62 ± 0.44
Sodium [mmol/L]	141 ± 2	141 ± 1	141 ± 2	142 ± 2	142 ± 3
Phosphate [mmol/L]	2.03 ± 0.20	2.00 ± 0.06	1.98 ± 0.08	2.02 ± 0.20	2.05 ± 0.14
Protein [mg/dL]	63 ± 3	60 ± 1*	62 ± 5	61 ± 2	62 ± 3
Triglycerides [mg/dL]	97 ± 30	77 ± 30	99 ± 25	87 ± 29	76 ± 23
Urea [mg/dL]	39.0 ± 2.7	36.3 ± 3.2	36.2 ± 3.3	36.6 ± 4.4	35.8 ± 2.6*

Differences can be seen for AST. AST is significantly increased for all groups post-treatment including control animals that were not irradiated. For control animals AST is increased by 3-fold ($p < 0.05$) and for all irradiated groups it is increased by 2-fold ($p < 0.05$ for 41.40 J/cm² and $p < 0.01$ for 10.35 J/cm² and 82.80 J/cm²).

Also cholesterol levels differ for all groups. Cholesterol is significantly decreased by approximately 10% ($p < 0.01$).

Some small changes can be seen for protein, where control rats have a significantly decreased protein concentration after the experiment compared to the baseline. The decrease amounts to 5% and is significant with $p < 0.05$.

Another parameter, urea, is decreased after treatment, but only for rats that received 82.80 J/cm² of blue light. The concentration is decreased by 8% ($p < 0.05$).

An ELISA test for the CRP concentration was performed (Figure 35).
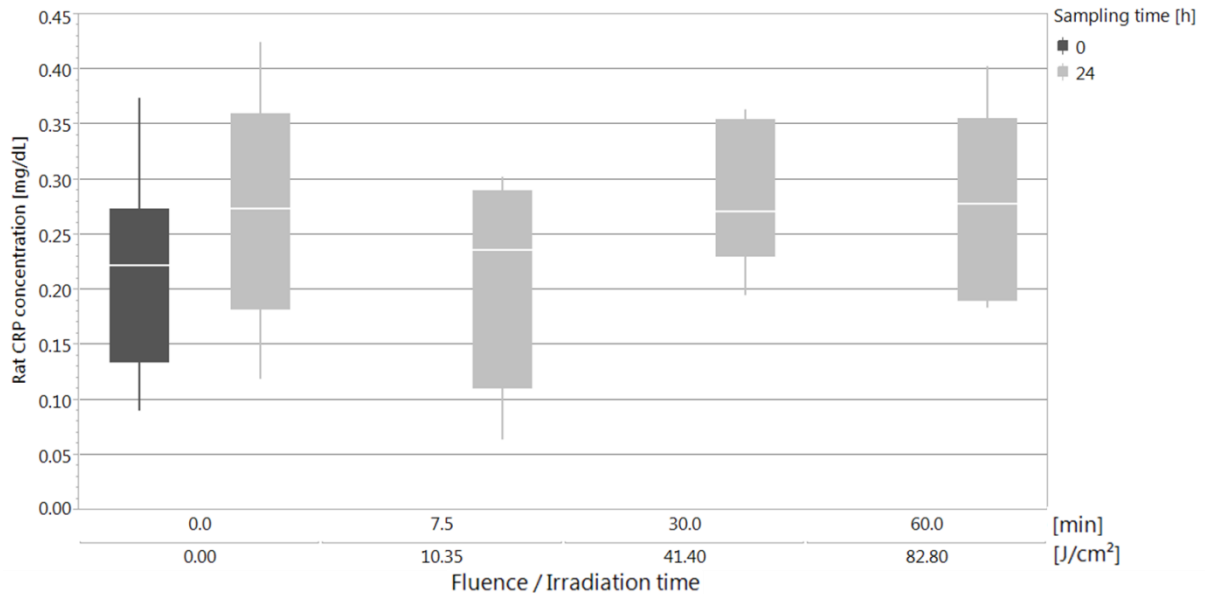
Figure 35: CRP concentration in rat plasma determined by ELISA of non-diabetic rats (ZDF fa/+). Samples were taken for all rats on day 0 before single irradiation with fluences of 10.35, 41.40, 82.80 J/cm² or no irradiation followed. 24 h post light treatment samples were taken again. Data are shown as box plots with the median, upper and lower quartile (interquartile range (IQR)) and whiskers (1.5 x IQR). Each box plot represents n=6 plasma samples.

The baseline CRP concentration was 0.22 mg/dL at time point 0 h before wounding. After 24 h the CRP increased to 0.27 mg/dL for control rats as well as for rats treated with 41.40 and 82.80 J/cm² of blue light. A small difference can be noticed when rats were treated with a dose of 10.35 J/cm² of blue light, where the CRP concentration drops to 0.23 mg/dL compared to other fluences. This concentration is nearly the same as for the baseline and is even lower than control rats after the experiment, but without statistical significance due to high standard deviation.

At the end of the experiment, skin samples were taken, embedded in paraffin, sliced and stained with H&E (section 2.4.9). These histology slides were imaged with the Axio Scan. First, the area of the inflammatory site was compared between groups (Figure 36). Criteria of identifying the inflammatory site were the lack of thick collagen fibers and increased presence of leukocytes and fibrin.
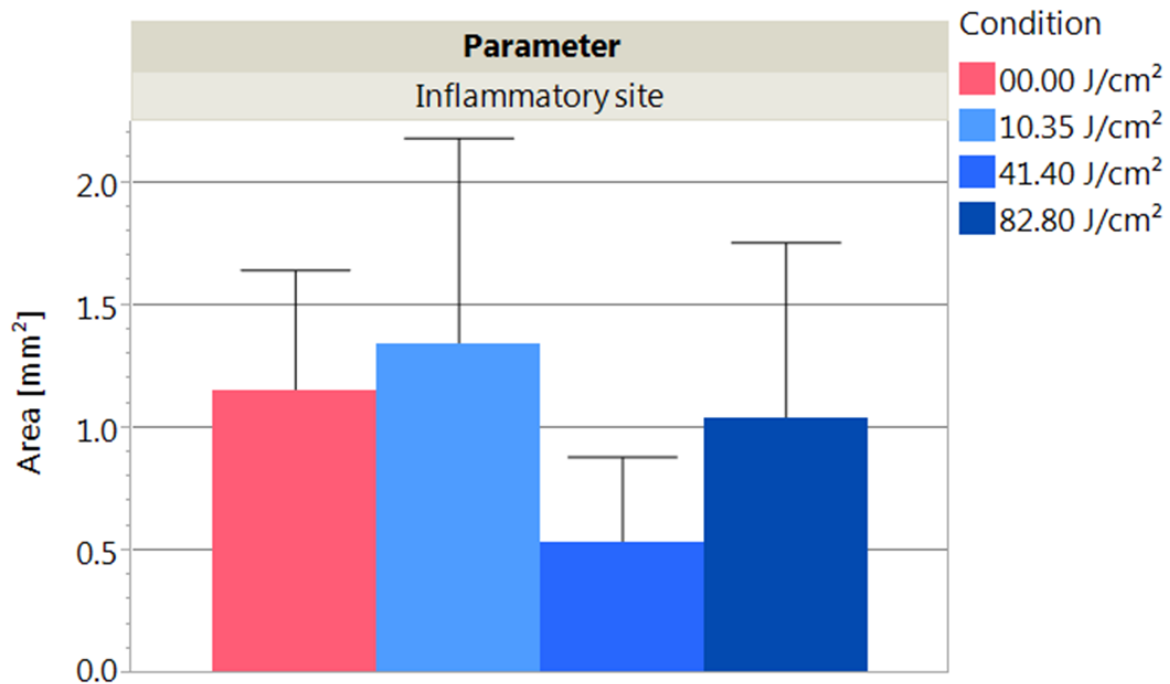
Figure 36: Results of image evaluation by ilastik segmentation are shown, divided into either control groups or irradiation with 10.35, 41.40 or 82.80 J/cm² of blue light. Data are displayed in mm² with means ± SD. Each group represents values from n=6 animals.

Areas of the groups do not differ significantly due to high standard deviations. The control group and groups irradiated with 10.35 J/cm² and 82.80 J/cm² have an inflammatory area of 1.0 to 1.3 mm². The group irradiated with 41.40 J/cm² shows a decrease to 0.54 mm² (p = 0.0656).

After determining the area of the inflammatory sites, they were inspected in regard to their fibrin and leukocyte content. As there are no significant differences between the four groups, data is not shown.

With another approach, possible differences between the groups were investigated, not considering the covered area by leukocytes, but the number of leukocytes in relation to the inflammatory site (Figure 37).

Significant differences between groups cannot be seen. With 11,000 leukocytes/mm² the control group and groups irradiated with 10.35 and 41.40 J/cm² have nearly the same number of leukocytes per mm². Animals irradiated with 82.80 J/cm² show a decrease of leukocytes per mm² with around 8,500 (p = 0.0712).

No differences between non-irradiated wounds of irradiated animals and the control wounds of non-irradiated animals could be seen, therefore the data is not shown.
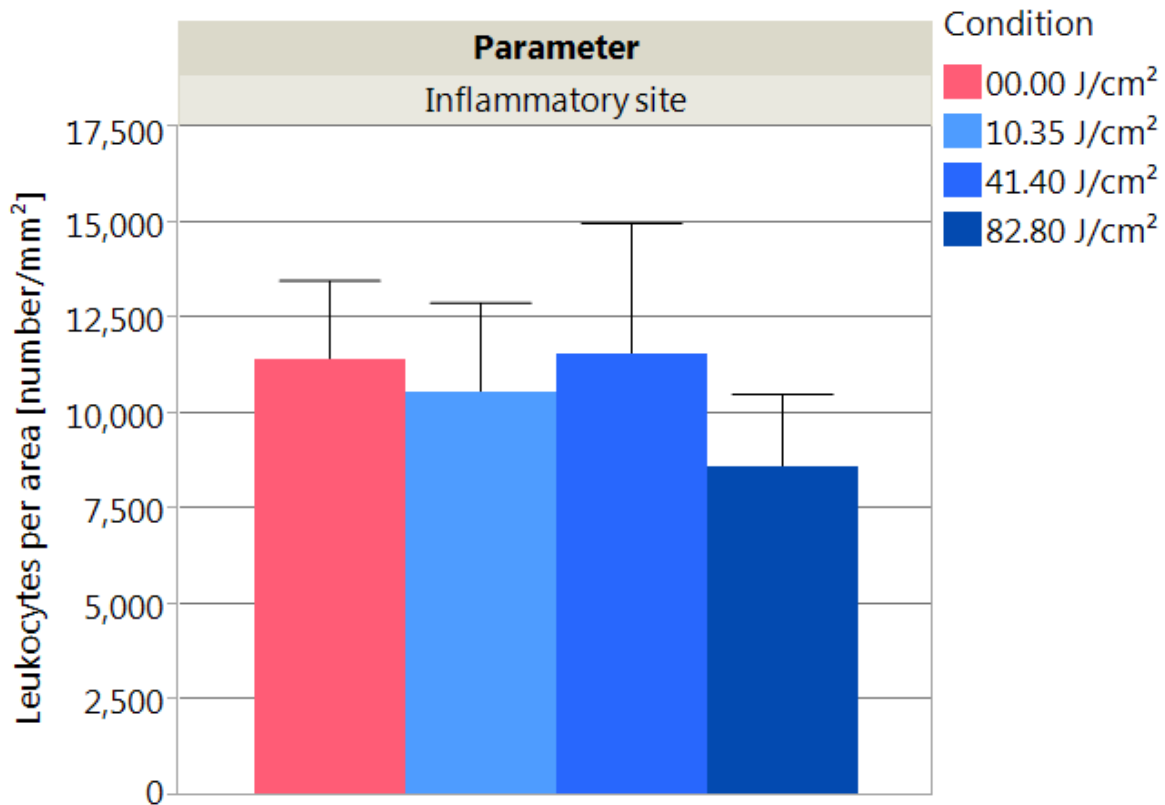
Figure 37: Results of image evaluation by ilastik segmentation are shown, divided into either control groups or irradiation with 10.35, 41.40 or 82.80 J/cm² of blue light. Data are displayed in number per area in mm² with means ± SD in relation to the area of the respective inflammatory site. Each group represents values from n=6 animals.

Gene set enrichment analysis (GSEA) was performed according to section 2.4.7. Selected genes were sorted into expression patterns according to the KEGG database and a ranked list was created. By comparing the normalized enrichment scores (NES) up- and down-regulated pathways were identified (Table 7).

Table 7: Overview of GSEA displaying the numbers of deregulated pathways for rats irradiated with 10.35 J/cm² (7.5 min), 41.40 J/cm² (30 min) and 82.80 J/cm² (60 min) of blue light. Genes were sorted into a total of 313 pathways. Fluorescence intensities of light treated samples are normalized to the control. Level of significances was defined as $p \leq 0.05$ for nominal and adjusted (FDR ≤ 0.25) p-values respectively.

Fluence	10.35 J/cm²	41.40 J/cm²	82.80 J/cm²
Pathways containing up-regulated genes	163	203	83
Significantly up-regulated pathways (nominal p-value < 0.05)	38	66	18
Significantly up-regulated pathways (adjusted p-value < 0.05)	8	41	13
Pathways containing down-regulated genes	150	110	230
Significantly down-regulated pathways (nominal p-value < 0.05)	22	30	76
Significantly down-regulated pathways (adjusted p-value < 0.05)	2	19	41

For 10.35 J/cm² and 41.40 J/cm² of blue light there is a shift to more pathways being up-regulated. For 82.80 J/cm² of blue light it is the opposite: more pathways are down-regulated.

In a further step, deregulated pathways with an adjusted p-value ≤ 0.05 were analysed in detail. KEGG sorts gene sets into 6 main categories. The distribution of pathways that are significantly deregulated according to these main categories is shown in Figure 38.
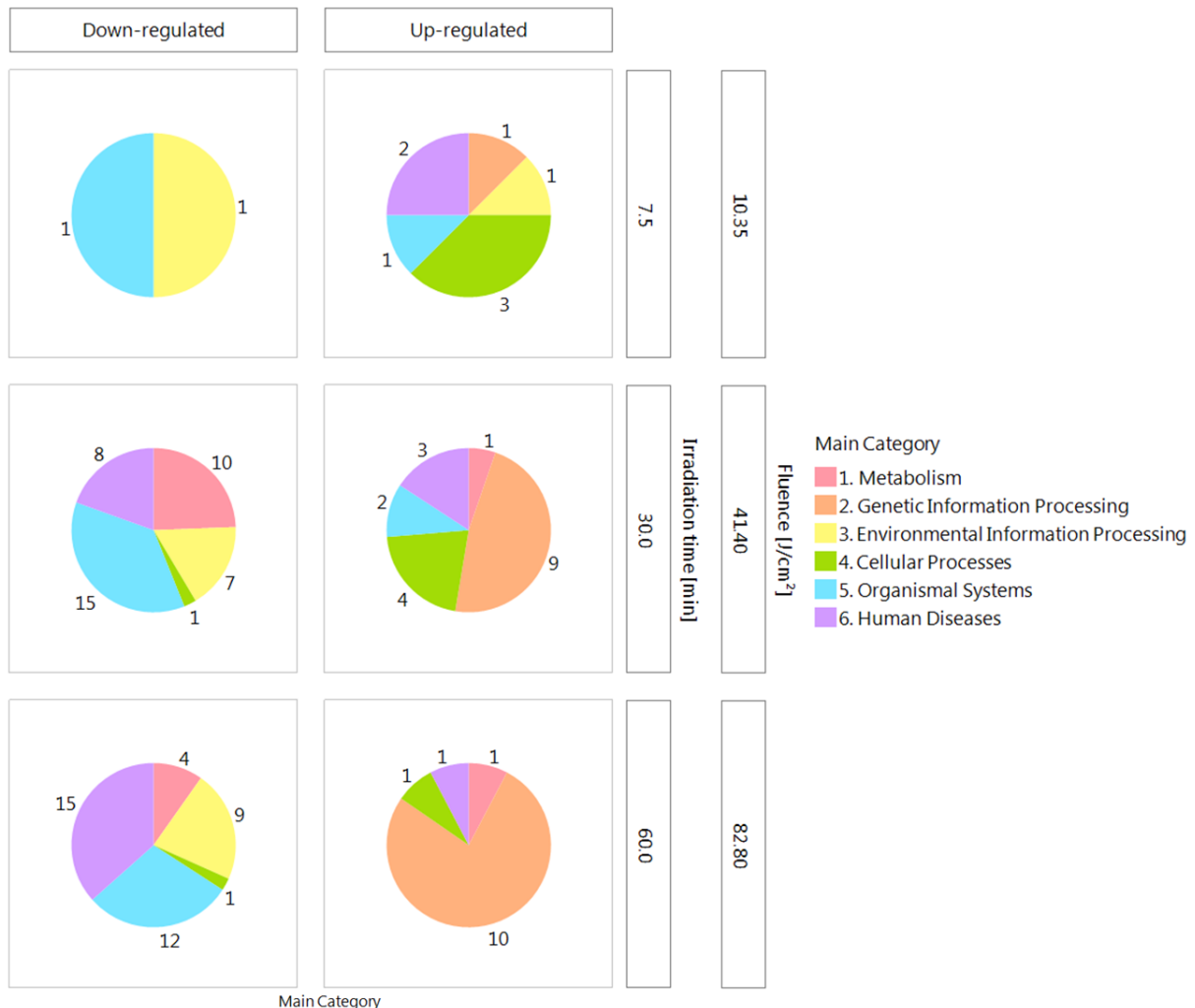
Figure 38: Pie chart showing the distribution of pathways containing significantly up- and down-regulated genes sorted by main categories of KEGG. Groups are formed by the respective fluences/irradiation times. The numbers around the pie charts indicate the number of deregulated pathways contained in each category.

Pathways belonging to the main category 'Metabolism' seem to be down-regulated strongest with 41.40 J/cm² and less so with 82.80 J/cm². 'Genetic Information Processing' is slightly up-regulated already with a fluence of 10.35 J/cm². Higher fluences increase the up-regulation of pathways belonging to this category with 9 pathways up-regulated with 41.40 J/cm² and 10 pathways up-regulated with 82.80 J/cm². The category 'Environmental Information Processing' is down-regulated

with 10.35 J/cm² and is down-regulated by a higher extent with 41.40 J/cm² (7 pathways) and 82.80 J/cm² (9 pathways). 10.35 J/cm² of blue light cause an up-regulation of cellular processes (3 pathways), and 41.40 J/cm² an even stronger effect with 4 pathways up-regulated. 82.80 J/cm² of blue light cause only a slight up-regulation of cellular processes (1 pathway). Pathways related to organismal systems and human diseases are strongly down-regulated for 41.40 J/cm² and 82.80 J/cm².

The KEGG database further divides the main categories in subcategories. To get a clearer picture of which processes are affected by blue light, the significantly deregulated pathways are displayed according to these subgroups.

In Figure 39 the main category 'Metabolism' with the corresponding deregulated subcategories is shown.
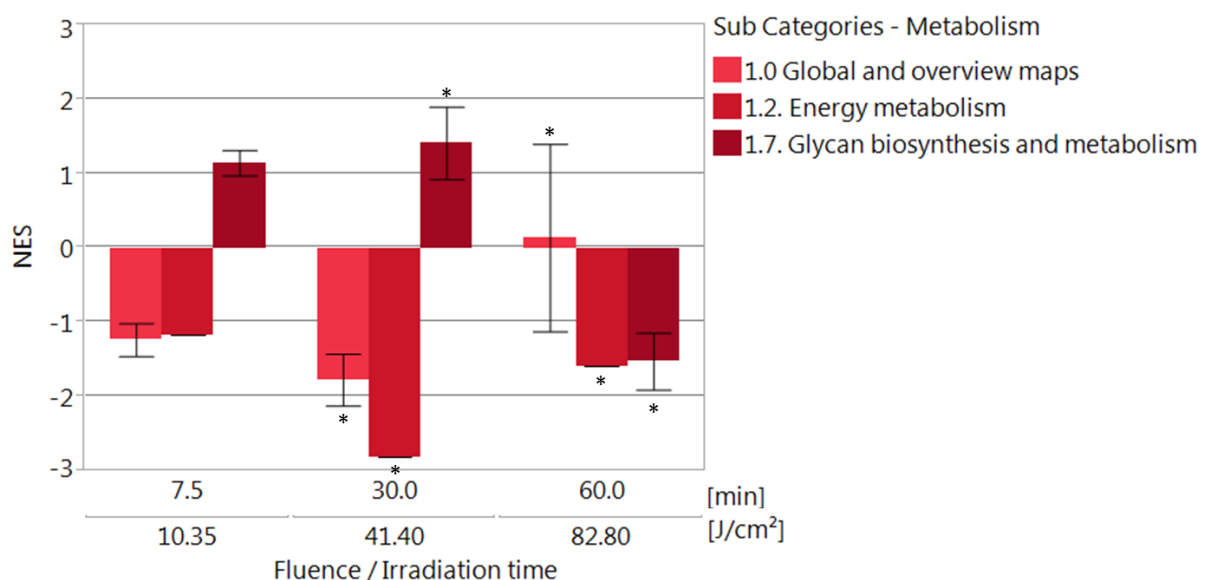
Figure 39: Main category "Metabolism' with subcategories containing deregulated pathways. The fluence and irradiation time is depicted by the NES. Values > 0 (< 0) indicate an up-regulation (down-regulation). Bar charts are shown with the mean and ± standard deviation. As not all pathways were significantly deregulated for each fluence and subcategory they were added for a complete summary. The distinction between up- and down-regulation was not made to get a better overview; therefore standard deviations can be high, if subcategories contain both significantly up- and down-regulated pathways.

While 10.35 J/cm² and 41.40 J/cm² induce down-regulation of global and overview maps, for 82.80 J/cm² of blue light expression remains unchanged. Energy metabolism is down-regulated for all fluences with the strongest effect at 41.40 J/cm². Glycan biosynthesis and metabolism is up-regulated for both 10.35 J/cm² and 41.40 J/cm² and is down-regulated for 82.80 J/cm².

The individual significantly up- and down-regulated pathways associated with the subcategories are summarized in Table 8.

By irradiation with 41.40 J/cm² metabolic pathways were down-regulated. The carbon metabolism as well as the biosynthesis of amino acids was found to be down-

regulated by this fluence as well. Oxidative phosphorylation was also down-regulated with higher fluences. The glycan biosynthesis was found to be up-regulated by a fluence of 41.40 J/cm² and the degradation down-regulated with 82.80 J/cm².

Table 8: Significantly deregulated pathways belonging to KEGG's main category 'Metabolism'. The main category is divided into 13 subcategories. Three of these categories contain significantly deregulated pathways, which are shown in the table with their respective NES and adjusted p-values. Up-regulated pathways are indicated by the positive NES colored in red and down-regulated pathways are indicated by the negative NES colored in green.

1. Metabolism						
Irradiation time		7.5 min		30.0 min		60.0 min
Fluence		10.35 J/cm²		41.40 J/cm²		82.80 J/cm²
	NES	**Adjusted p-value**	**NES**	**Adjusted p-value**	**NES**	**Adjusted p-value**
1.0. Global and overview maps						
Metabolic pathways	-1.04	0.5906	-1.54	0.0028	-1.32	0.0086
Carbon metabolism	-1.48	0.1112	-2.18	0.0028	0.78	0.9614
Biosynthesis of amino acids	-1.20	0.4522	-1.62	0.0272	0.94	0.7174
1.2. Energy metabolism						
Oxidative phosphorylation	-1.17	0.4680	-2.81	0.0028	-1.60	0.0255
1.7. Glycan biosynthesis and metabolism						
N – glycan biosynthesis	1.26	0.4014	1.75	0.0209	-1.26	0.2764
Glycosaminoglycan degradation	1.02	0.6931	1.06	0.5834	-1.80	0.0338

In the main category 'Genetic Information Processing', pathways of all subcategories are slightly up-regulated with 10.35 J/cm² and significantly stronger up-regulated with higher fluences. An overview graph is shown in Figure 40.
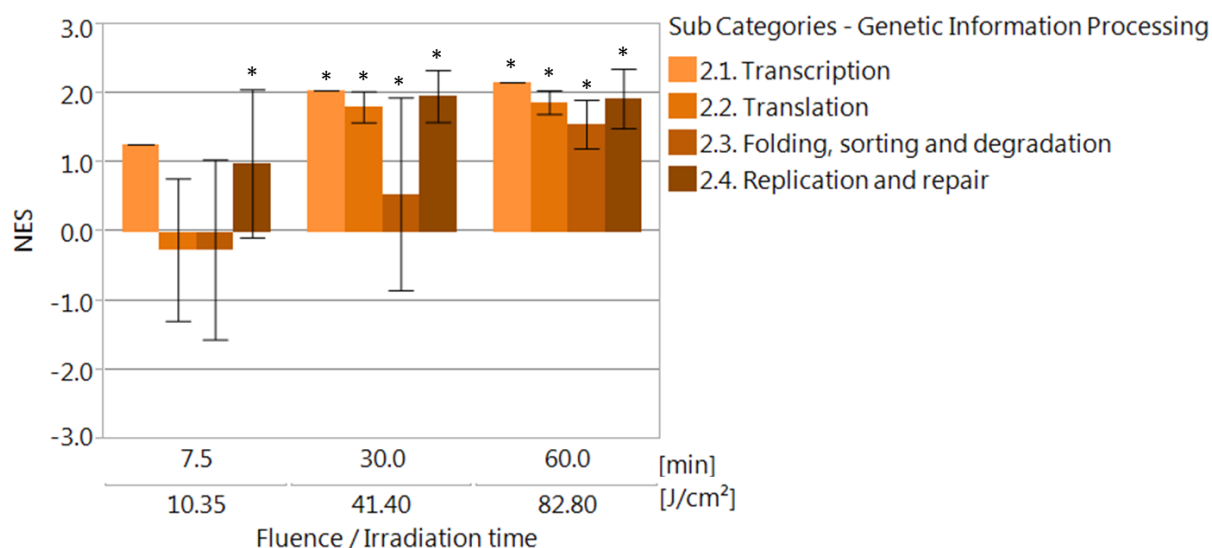
Figure 40: Main category 'Genetic Information Processing' with subcategories containing deregulated pathways. The fluence and irradiation time is depicted by the NES. Values > 0 (< 0) indicate an up-regulation (down-regulation). Bar charts are shown with the mean and ± standard deviation. As not all pathways were significantly deregulated for each fluence and subcategory they were added for a complete summary. The distinction between up- and down-regulation was not made to get a better overview; therefore standard deviations can be high, if subcategories contain both significantly up- and down-regulated pathways.

The individual significantly up- and down-regulated pathways associated with the subcategories are summarized in Table 9.

**Table 9: Significantly deregulated pathways belonging to KEGG's main category 'Genetic Information Processing'.** The main category is divided into 4 subcategories; all of the categories contain significantly deregulated pathways, which are shown in the table with their respective NES and adjusted p-values. Up-regulated pathways are indicated by the positive NES colored in red and down-regulated pathways are indicated by the negative NES colored in green.

2. Genetic Information Processing						
Irradiation time	7.5 min		30.0 min		60.0 min	
Fluence	10.35 J/cm²		41.40 J/cm²		82.80 J/cm²	
	NES	Adjusted p-value	NES	Adjusted p-value	NES	Adjusted p-value
2.1. Transcription						
Spliceosome	1.26	0.2613	2.05	0.0035	2.15	0.0053
2.2. Translation						
Ribosome biogenesis in eukaryotes	0.93	0.7858	-2.81	0.0028	1.88	0.0053
RNA transport	-0.84	0.8340	1.96	0.0035	2.04	0.0053
mRNA surveillance pathway	-0.87	0.7344	1.55	0.0341	1.70	0.0157
2.3. Folding, sorting and degradation						
Ubiquitin mediated proteolysis	-1.18	0.4283	-1.06	0.5750	1.51	0.0359
SNARE interactions in vesicular transport	1.23	0.1674	1.24	0.3503	1.93	0.0137
Protein processing in endoplasmatic reticulum	-0.83	0.9378	1.46	0.0304	1.23	0.2265
2.4. Replication and repair						
DNA replication	1.87	0.0494	2.26	0.0035	2.04	0.0086
Nucleotide excision repair	-0.86	0.8503	1.36	0.2176	2.19	0.0053
Mismatch repair	1.48	0.2559	1.98	0.0075	2.30	0.0053
Homologous recombination	1.38	0.2677	2.30	0.0035	1.90	0.0111
Fanconi anemia pathway	1.06	0.6279	1.91	0.0052	1.21	0.3260

In the first subcategory '2.1. Transcription', the splicing process is significantly up-regulated. Also translation processes are mostly up-regulated except for the ribosome biogenesis after irradiation with 41.40 J/cm² of blue light. In the subcategory of '2.3. Folding, sorting and degradation', proteolysis, vesicular transport and protein processing are up-regulated. Pathways associated with replication and repair were also found to be up-regulated.

In Figure 41 the main category 'Environmental Information Processing' with the corresponding deregulated subcategories is shown.

Pathways belonging to the signal transduction are up- and down-regulated with 10.35 J/cm², resulting in no overall change. With 41.40 J/cm² and 82.80 J/cm² down-regulation of pathways of this subcategory is induced. Pathways of the subcategory '3.3. Signaling molecules and interaction' are up-regulated at 10.35 J/cm², 41.40 J/cm² shows no change while containing up- and down-regulated pathways and is down-regulated for 82.80 J/cm².
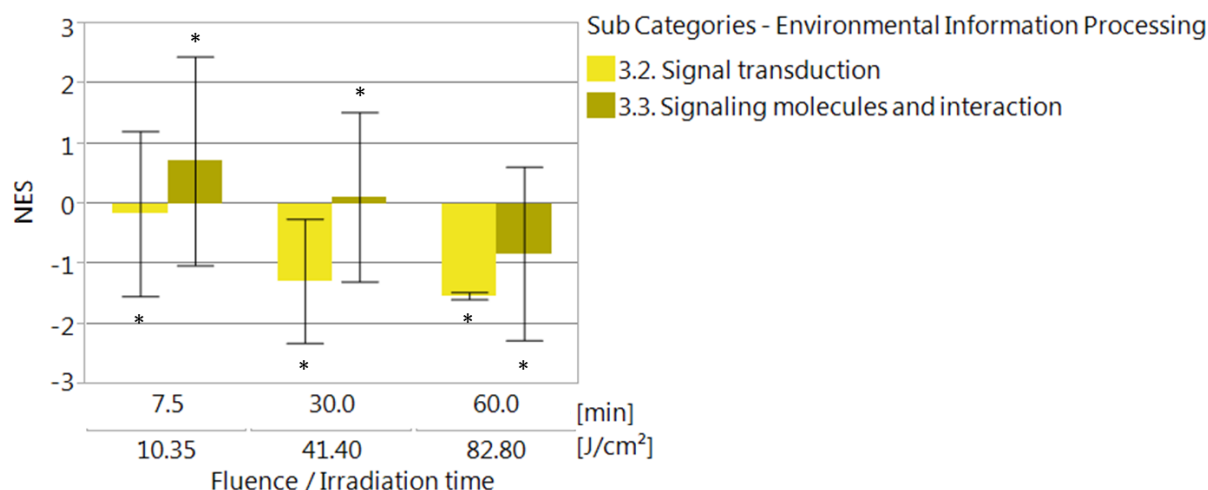
Figure 41: Main category 'Environmental Information Processing' with subcategories containing deregulated pathways. The fluence and irradiation time is depicted by the NES. Values > 0 (< 0) indicate an up-regulation (down-regulation). Bar charts are shown with the mean and ± standard deviation. As not all pathways were significantly deregulated for each fluence and subcategory they were added for a complete summary. The distinction between up- and down-regulation was not made to get a better overview; therefore standard deviations can be high, if subcategories contain both significantly up- and down-regulated pathways.

The individual significantly up- and down-regulated pathways associated with the subcategories are summarized in Table 10.

Table 10: Significantly deregulated pathways belonging to KEGG's main category 'Environmental Information Processes'. The main category is divided into 3 subcategories. Two of the categories contain significantly deregulated pathways, which are shown in the table with their respective NES and adjusted p-values. Up-regulated pathways are indicated by the positive NES colored in red and down-regulated pathways are indicated by the negative NES colored in green.

3. Environmental Information Processes						
Irradiation time	7.5 min		30.0 min		60.0 min	
Fluence	10.35 J/cm²		41.40 J/cm²		82.80 J/cm²	
	NES	Adjusted p-value	NES	Adjusted p-value	NES	Adjusted p-value
3.2. Signal transduction						
MAPK signaling pathway	1.14	0.4014	-1.48	0.0090	-1.41	0.0390
Calcium signaling pathway	-0.99	0.7310	-1.82	0.0028	-1.55	0.0243
cGMP_PKG signaling pathway	-1.07	0.5906	-1.92	0.0028	-1.57	0.0243
cAMP signaling pathway	0.94	0.8138	-1.48	0.0219	-1.50	0.0285
AMPK signaling pathway	-1.71	0.0277	-1.69	0.0055	-1.58	0.0278
Apelin signaling pathway	-1.17	0.4516	-1.62	0.0115	-1.55	0.0338
3.3. Signaling molecules and interaction						
Viral protein interaction with cytokine and cytokine receptor	1.67	0.0532	0.70	0.9975	-1.68	0.0236
Neuroactive ligand-receptor interaction	-1.29	0.1603	-1.49	0.0035	-1.64	0.0053
Cell adhesion molecules (CAMs)	1.76	0.0269	1.14	0.3503	0.84	0.9158

The subcategory '3.2. Signal transduction' shows that for 10.35 J/cm² only the AMPK signaling pathway is significantly down-regulated. For higher fluences all other pathways are significantly down-regulated. The third subcategory shows down-regulation of cell adhesion molecules for 10.35 J/cm², while for 41.40 J/cm² neuroactive ligand-receptor interaction is down-regulated. For 82.80 J/cm² the same

pathway is down-regulated, but to a higher extent. Also the viral protein interaction with cytokines is down-regulated.

In Figure 42 the main category 'Cellular Processes' with the corresponding deregulated subcategories is shown.
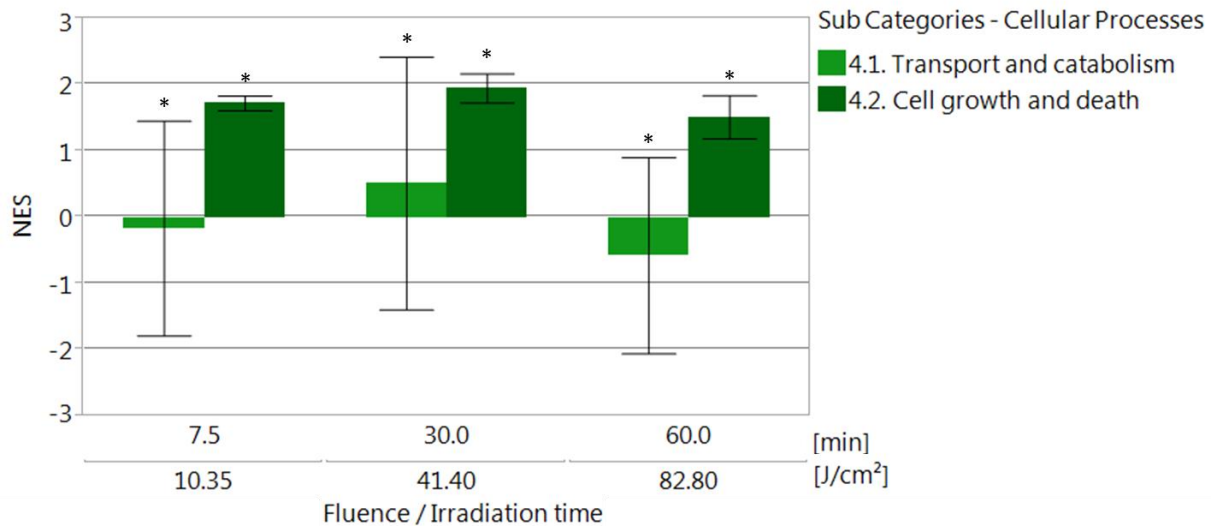
Figure 42: Main category 'Cellular Processes' with subcategories containing deregulated pathways. The fluence and irradiation time is depicted by the NES. Values > 0 (< 0) indicate an up-regulation (down-regulation). Bar charts are shown with the mean and ± standard deviation. As not all pathways were significantly deregulated for each fluence and subcategory they were added for a complete summary. The distinction between up- and down-regulation was not made to get a better overview; therefore standard deviations can be high, if subcategories contain both significantly up- and down-regulated pathways.

For the subcategory '4.1. Transport and catabolism' the differential expression of genes by 10.35 J/cm² results in no overall change. For 41.40 J/cm² there is a slight up-regulation and for 82.80 J/cm² a slight down-regulation. The significantly up- or down-regulated pathways belonging to this main category are summarized in Table 11.

Table 11: Significantly deregulated pathways belonging to KEGG's main category 'Cellular Processes'. The main category is divided into 5 subcategories. Two of the categories contain significantly deregulated pathways, which are shown in the table with their respective NES and adjusted p-values. Up-regulated pathways are indicated by the positive NES colored in red and down-regulated pathways are indicated by the negative NES colored in green.

4. Cellular Processes						
Irradiation time	**7.5 min**		**30.0 min**		**60.0 min**	
Fluence	**10.35 J/cm²**		**41.40 J/cm²**		**82.80 J/cm²**	
	NES	Adjusted p-value	NES	Adjusted p-value	NES	Adjusted p-value
4.1. Transport and catabolism						
Lysosome	-0.93	0.7858	1.41	0.0820	-1.84	0.0053
Phagosome	1.69	0.0269	1.80	0.0035	1.05	0.5080
Peroxisome	-1.27	0.3423	-1.68	0.0118	-0.95	0.7097
4.2. Cell growth and death						
Cell cycle	1.80	0.0277	2.10	0.0035	1.74	0.0053
p53 signaling pathway	1.64	0.0699	1.79	0.0067	1.28	0.2299

Lysosomal transport and catabolism is down-regulated for 82.80 J/cm². For phagosomes these processes are up-regulated for 10.35 J/cm² and 41.40 J/cm². Additionally with 41.40 J/cm² transport related to peroxisomes is down-regulated. Concerning the subcategory '4.2. Cell growth and death' the cell cycle and the p53 signaling pathway are up-regulated for all fluences.

The main category 'Organismal Systems' is divided into 10 subcategories. 5 of these subcategories contain deregulated pathways, which are shown in Figure 43.
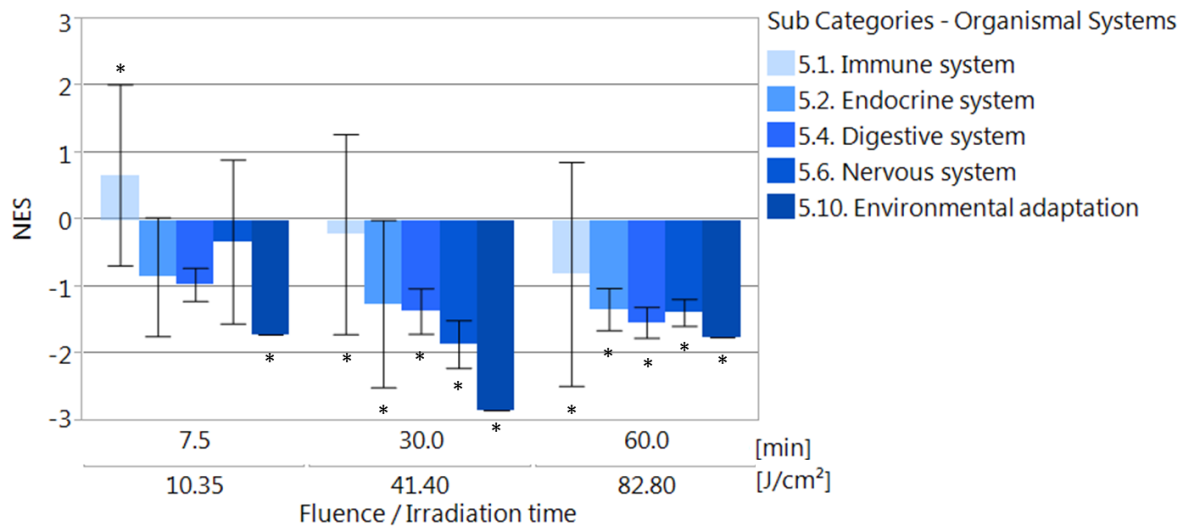
Figure 43: Main category 'Organismal Systems' with subcategories containing deregulated pathways. The fluence and irradiation time is depicted by the NES. Values > 0 (< 0) indicate an up-regulation (down-regulation). Bar charts are shown with the mean and ± standard deviation. As not all pathways were significantly deregulated for each fluence and subcategory they were added for a complete summary. The distinction between up- and down-regulation was not made to get a better overview; therefore standard deviations can be high, if subcategories contain both significantly up- and down-regulated pathways.

Pathways for the regulation of the immune system appear to be up-regulated by 10.35 J/cm², while for 41.40 J/cm² and 82.80 J/cm² the pathways are mostly down-regulated. The endocrine and digestive systems are down-regulated for all fluences with the strongest down-regulation at 82.80 J/cm². The nervous system and the environmental adaptation are also down-regulated for all fluences, but the strongest down-regulation is achieved with 41.40 J/cm².

To analyze the significantly deregulated pathways in detail, a summary table was created (Table 12).

Changes in gene expression of the immune system with 10.35 J/cm² appears by the up-regulation of the leukocyte transendothelial migration. For 82.80 J/cm² the toll-like receptor signaling and the cytosolic DNA-sensing pathway are down-regulated.

For the endocrine system the melanogenesis and aldosterone synthesis and secretion is down-regulated for 41.40 J/cm² and 82.80 J/cm². Also the thyroid hormone signaling pathway is down-regulated for 82.80 J/cm².

Table 12: Significantly deregulated pathways belonging to KEGG's main category 'Organismal Systems'. The main category is divided into 10 subcategories. Five of the categories contain significantly deregulated pathways, which are shown in the table with their respective NES and adjusted p-values. Up-regulated pathways are indicated by the positive NES colored in red and down-regulated pathways are indicated by the negative NES colored in green.

5. Organismal Systems						
Irradiation time	7.5 min		30.0 min		60.0 min	
Fluence	10.35 J/cm²		41.40 J/cm²		82.80 J/cm²	
	NES	Adjusted p-value	NES	Adjusted p-value	NES	Adjusted p-value
5.1. Immune system						
Toll-like receptor signaling pathway	1.12	0.5266	-1.12	0.4783	-1.83	0.0111
Cytosolic DNA-sensing pathway	-0.85	0.8571	-1.03	0.6133	-1.71	0.0243
Leukocyte transendothelial migration	1.74	0.0348	1.51	0.0367	1.12	0.3848
5.2. Endocrine system						
Melanogenesis	-1.30	0.2836	-1.55	0.0304	-1.68	0.0157
Thyroid hormone signaling pathway	-1.28	0.2836	0.92	0.8074	-1.56	0.0308
Aldosterone synthesis and secretion	-0.97	0.7310	-1.60	0.0227	-1.66	0.0199
5.4. Digestive system						
Salivary secretion	-1.02	0.6915	-1.65	0.0152	-1.49	0.0757
Gastric acid secretion	-1.03	0.6698	-1.67	0.0146	-1.15	0.3622
Pancreatic secretion	-1.12	0.5394	-1.41	0.1001	-1.61	0.0308
Fat digestion and absorption	-0.53	0.9937	-0.85	0.8381	-1.69	0.0409
Bile secretion	-1.12	0.5658	-1.22	0.3503	-1.71	0.0243
5.6. Nervous system						
Long-term potentation	-0.90	0.8255	-1.83	0.0055	-1.19	0.3260
Retrograde endocannabinoid signaling	-1.15	0.4812	-2.22	0.0028	-1.59	0.0243
Cholinergic synapse	1.08	0.5842	-1.51	0.0446	-1.36	0.1353
5.10. Environmental adaptation						
Thermogenesis	-1.72	0.0269	-2.84	0.0028	-1.76	0.0053

Relevant pathways belonging to the digestive system are the pancreatic secretion, fat digestion and absorption, and bile secretion, which are down-regulated for 82.80 J/cm². 41.40 J/cm² show a significant effect on the nervous system, where pathways of long-term potentiation, retrograde endocannabinoid signaling and cholinergic synapse are down-regulated. In the subcategory of environmental adaptation, thermogenesis is down-regulated for all fluences.

In the main category 'Human Diseases' 12 subcategories are listed in KEGG of which four were found to be deregulated after irradiation with blue light (Figure 44). Immune diseases are up-regulated by all fluences with the strongest effect after 10.35 J/cm² of blue light. Neurodegenerative, endocrine and metabolic diseases are down-regulated for all fluences as well, but with the strongest effect after 41.40 J/cm². Pathways linked to bacterial infectious diseases are up-regulated by 10.35 J/cm² and less so by 41.40 J/cm². 82.80 J/cm² of blue light induces the opposite, where pathways connected to bacterial infectious diseases are down-regulated.
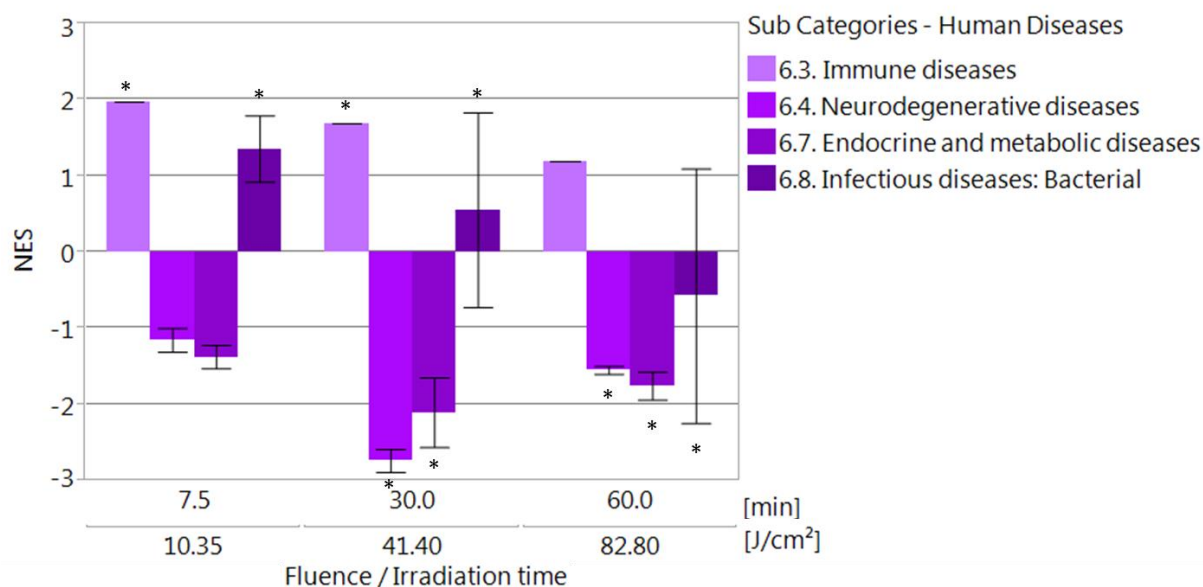
Figure 44: Main category 'Human Diseases' with subcategories containing deregulated pathways. The fluence and irradiation time is depicted by the NES. Values > 0 (< 0) indicate an up-regulation (down-regulation). Bar charts are shown with the mean and ± standard deviation. As not all pathways were significantly deregulated for each fluence and subcategory they were added for a complete summary. The distinction between up- and down-regulation was not made to get a better overview; therefore standard deviations can be high, if subcategories contain both significantly up- and down-regulated pathways.

A summary list of all pathways deregulated in the main category 'Human Diseases' divided by their subcategory is shown in Table 13.

Table 13: Significantly deregulated pathways belonging to KEGG's main category 'Human Diseases'. The main category is divided into 12 subcategories. Four of the categories contain significantly deregulated pathways, which are shown in the table with their respective NES and adjusted p-values. Up-regulated pathways are indicated by the positive NES colored in red and down-regulated pathways are indicated by the negative NES colored in green.

6. Human Diseases						
Irradiation time	7.5 min		30.0 min		60.0 min	
Fluence	10.35 J/cm²		41.40 J/cm²		82.80 J/cm²	
	NES	Adjusted p-value	NES	Adjusted p-value	NES	Adjusted p-value
6.3. Immune diseases						
Systemic lupus erythematosus	1.97	0.0277	1.68	0.0118	1.19	0.3150
6.4. Neurodegenerative diseases						
Alzheimer disease	-1.00	0.7141	-2.69	0.0028	-1.53	0.0267
Parkinson disease	-1.31	0.2613	-2.91	0.0028	-1.61	0.0243
Huntington disease	-1.16	0.4403	-2.62	0.0028	-1.51	0.0308
6.7. Endocrine and metabolic diseases						
Type II diabetes mellitus	-1.51	0.1669	-1.96	0.0035	-1.66	0.0402
Insulin resistance	-1.41	0.1669	-1.74	0.0046	-1.64	0.0243
Non-alcoholic fatty liver disease (NAFLD)	-1.21	0.4013	-2.62	0.0028	-1.97	0.0053
6.8. Infectious diseases: Bacterial						
Bacterial invasion of epithelial cells	1.82	0.0277	1.63	0.0300	1.35	0.1657
Pertussis	1.29	0.2973	0.89	0.8354	-1.62	0.0402
Tuberculosis	0.96	0.7682	-0.86	0.8898	-1.46	0.0476

In the category of immune diseases, pathways of systemic lupus erythematosus are up-regulated for all fluences. Neurodegenerative diseases as Alzheimer, Parkinson

and Huntington disease are down-regulated for 41.40 J/cm² and 82.80 J/cm². Endocrine and metabolic diseases as type II diabetes, insulin resistance and non-alcoholic fatty liver disease are down-regulated for the same fluences. For bacterial infectious diseases the bacterial invasion of epithelial cells is up-regulated for 10.35 J/cm² and 41.40 J/cm². Pertussis and Tuberculosis are down-regulated with 82.80 J/cm².

3.1.5 Long-term irradiation of diabetic and non-diabetic rats with ENMECH board

After single irradiations were tested on animals, a schedule for light therapy was generated (Table 14).

Table 14: Light schedule for long-term irradiation as a possible therapy against diabetic foot ulcers.

Healing stage	Infection (Bacteria)	Cleansing (Macrophages)	Granulation (Fibroblasts)	Epidermisation (Keratinocytes)
Irradiation time	Blue light 60 min	Blue light 30 min	Blue light 7.5 min	Blue light 7.5 min
Frequency	24 h	24 h	24 h	48 h

The light schedule includes all irradiation times that were tested in short-term experiments (section 3.1.4). Every phase was tested for 3 consecutive days. ZDF fa/fa rats were fed with a special diet causing diabetes. To follow the progress of the disease blood glucose concentrations were tested weekly (Figure 45).
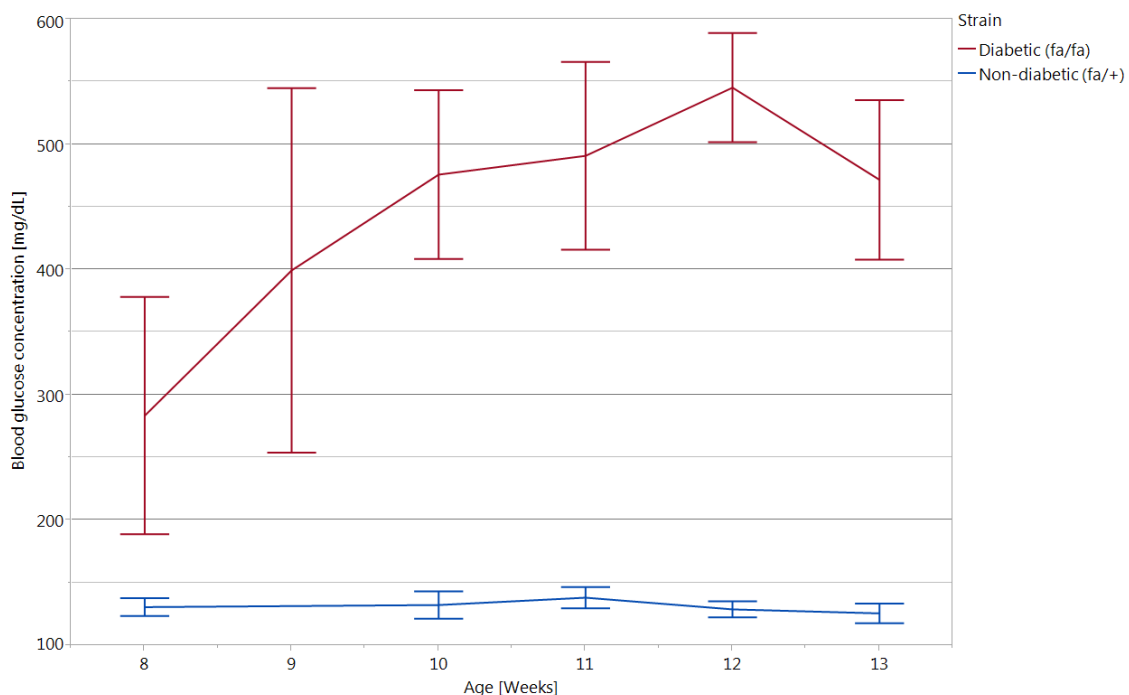
Figure 45: Blood glucose concentrations [mg/dL] of rats which are to be irradiated over the course of 12 days. The graph shows values for diabetic rats (fa/fa) in red and for healthy rats (fa/+) in blue. The measurements started shortly after arrival of the rats and continued until the end of the experiment. Data are displayed as mean values ± SD with n=18 animals.

As a reference ZDF fa/+ rats were included. For healthy ZDF fa/+ rats gaps between measurements were bigger due to stable results throughout the experiment. The glucose concentration of ZDF fa/fa rats is steadily increasing over time, starting at approximately 280 mg/dL at the age of 8 weeks. The peak is reached at the age of 12 weeks with a concentration of 550 mg/dL. These rising glucose levels are accompanied by polyuria and polydipsia

After wounding with a biopsy punch (6 mm), images of the wounds were taken daily. The images were analysed with Fiji by using the freehand selection to measure the area of the wound in pixels. The area in pixels was then converted into mm²; the areas were divided by the initial wound areas to obtain percentages (Figure 46).
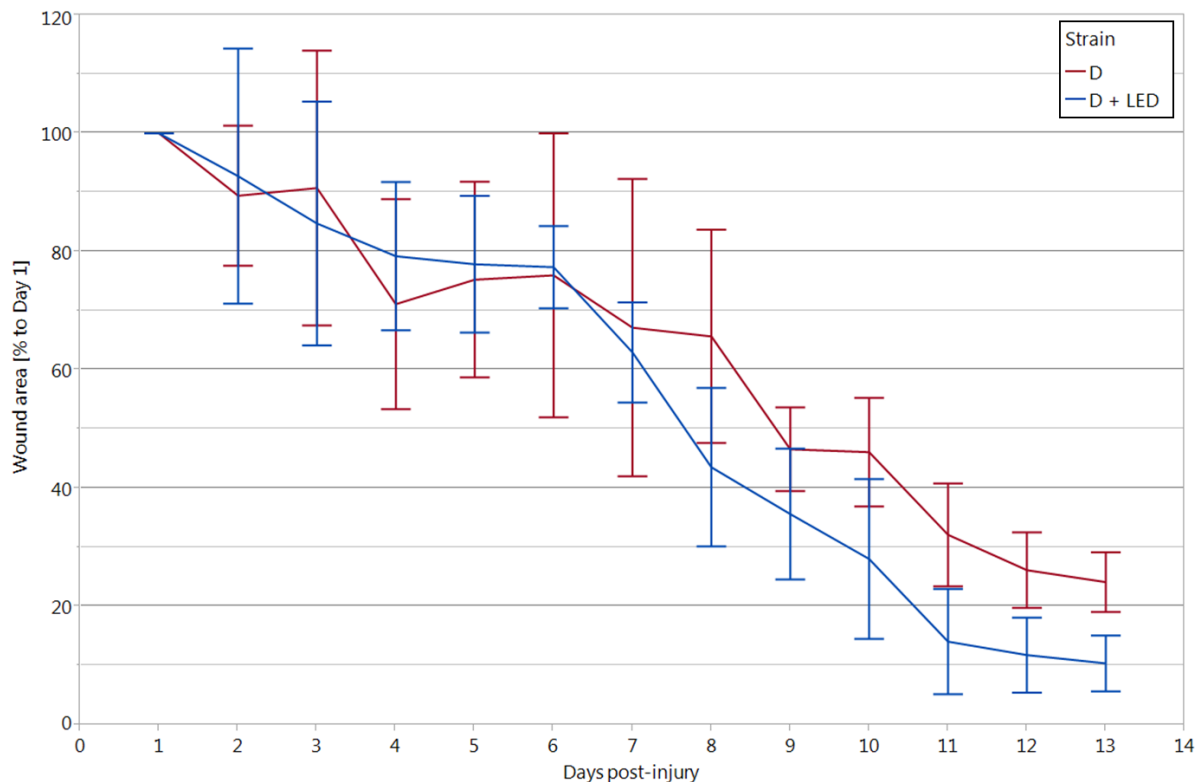
Figure 46: Wound areas displayed in % normalized to the wound area on day 1 (D = Diabetic ZDF fa/fa, LED = Light therapy). Rats were irradiated with blue light according to the light schedule: 82.80 J/cm² on day 1-3, 41.40 J/cm² on day 4-6, 10.35 J/cm² on day 7-9 and 10.35 J/cm² on day 11. Each curve represents n=6, data are displayed as mean values ± SD.

During irradiation with 82.80 and 41.40 J/cm² of blue light, there is no significant difference of the wound areas compared to the control rats. As soon as irradiation with 10.35 J/cm² starts, the wounds close faster for rats receiving the light treatment. On day 8 there is a significant difference of 20% ($p < 0.05$) and on day 9 of 10%, which is not significant. On days 10 to 13 the difference of wound areas is about 15% with statistical significance throughout (days 10 to 12 with $p < 0.05$ and day 13 with

p < 0.01). The wound area of control rats on day 13 approximately corresponds to the wound area of irradiated rats on day 10, revealing an advantage of 3 days when applying the light therapy.

Furthermore, the third group with non-diabetic rats was compared to diabetic rats, both receiving light treatment (Figure 47).
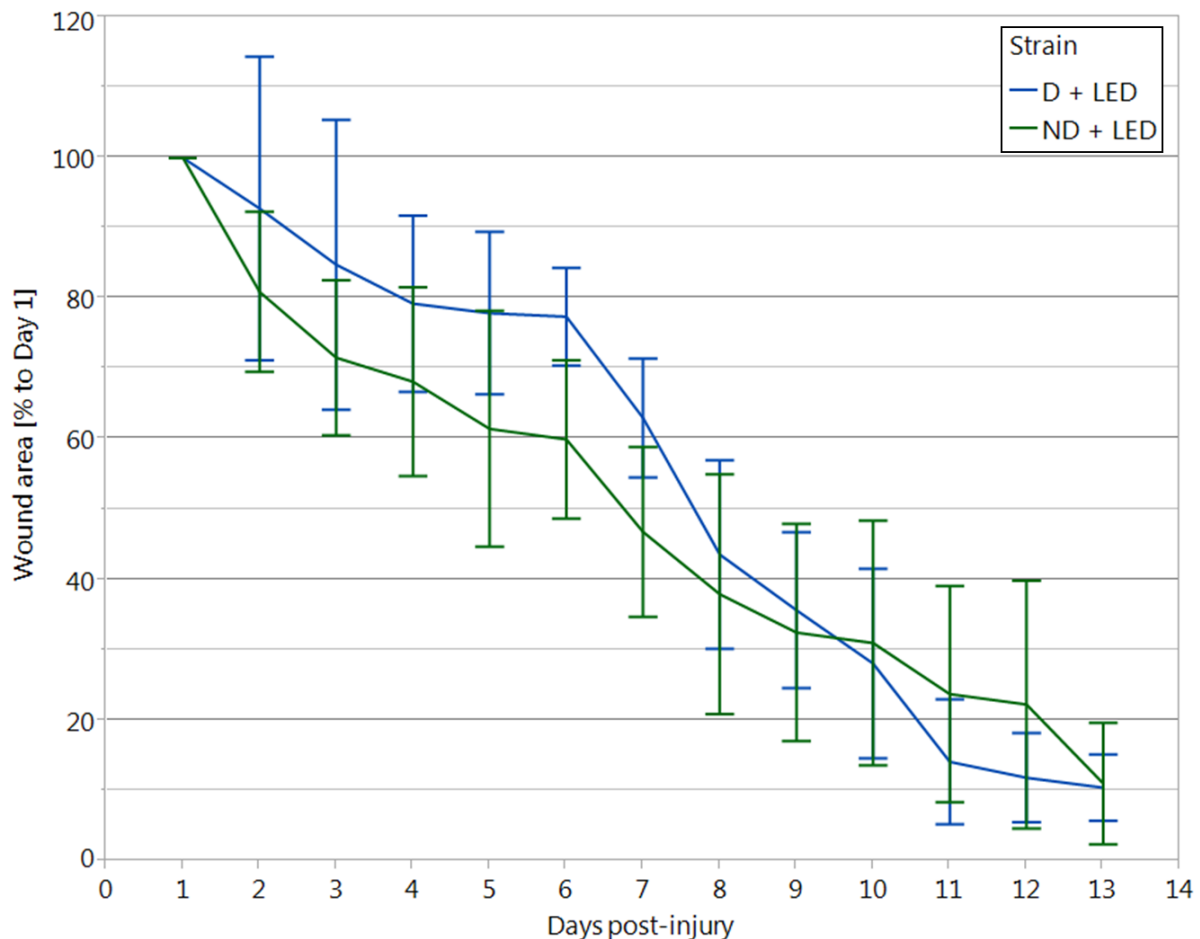
Figure 47: Wound areas displayed in % normalized to the wound area on day 1 (D = Diabetic ZDF fa/fa, ND = Non-diabetic ZDF fa/+, LED = Light therapy). Rats were irradiated with blue light according to the light schedule: 82.80 J/cm² on day 1-3, 41.40 J/cm² on day 4-6, 10.35 J/cm² on day 7-9 and 10.35 J/cm² on day 11. Each curve represents n=6, data are displayed in means ± SD.

Here, the wounds of non-diabetic rats healed faster on day 1 to 9 compared to diabetic rats. The differences are significant on days 5 to 7 with a significance of $p < 0.05$. Between day 9 and 10 the wounds are equal in size and afterwards the wounds of diabetic rats are smaller on day 11 and 12 without statistical significance. On the last day of the experiment wound areas are identical in size.

To analyse possible systemic effects, non-irradiated wounds of irradiated animals and the wounds of non-irradiated animals were compared. No differences could be seen; therefore the data is not shown.

Possible biochemical changes in plasma were tested with the Cobas c 311 analyzer. A full overview plasma profile was created including kidney and liver function profiles (Table 15).

Table 15: Plasma parameters of diabetic and non-diabetic rats irradiated with complete light schedule. Baseline (n=12 (D), n=6 (ND)) was created from plasma samples taken before the experiment was started on day 1. Plasma samples for irradiated rats were taken 24 h after the last irradiation on day 13. Data are expressed as means ± SD. Values significantly different are indicated as *$p < 0.05$, **$p < 0.01$, ***$p <0.001$. Comparisons on day 1 were done between non-diabetic and diabetic rats (ZDF fa/+ and ZDF fa/fa). Comparisons on day 13 were done in relation to their respective baseline on day 1.

Plasma parameter	Time point [days]	ZDF fa/+ rats Irradiated	ZDF fa/fa rats Control	ZDF fa/fa rats Irradiated
ALT [U/L]	1	38 ± 9	185 ± 134***	
	13	48 ± 8	75 ± 76*	53 ± 43**
AST [U/L]	1	77 ± 2	140 ± 109	
	13	105 ± 24**	99 ± 47	74 ± 19
Calcium [mmol/L]	1	2.72 ± 0.09	2.56 ± 0.56	
	13	2.64 ± 0.08	2.76 ± 0.19	2.85 ± 0.10
Cholesterol [mg/dL]	1	94 ± 6	127 ± 35	
	13	98 ± 6	121 ± 24	129 ± 15
Creatinine [mg/mL]	1	0.27 ± 0.03	0.19 ± 0.06***	
	13	0.28 ± 0.03	0.21 ± 0.03	0.19 ± 0.03
GLDH [U/L]	1	12.64 ± 8.64	79.36 ± 81.79*	
	13	7.98 ± 3.74	38.57 ± 33.34	23.37 ± 15.48
Phosphate [mmol/L]	1	2.13 ± 0.24	2.37 ± 0.15*	
	13	2.04 ± 0.16	2.35 ± 0.23	2.29 ± 0.15
Potassium [mmol/L]	1	4.67 ± 0.34	5.40 ± 1.03	
	13	4.56 ± 0.31	4.25 ± 0.26***	4.34 ± 0.22**
Protein [mg/mL]	1	63 ± 3	61 ± 11	
	13	62 ± 3	66 ± 5	66 ± 3
Sodium [mmol/L]	1	144 ± 3	125 ± 25***	
	13	146 ± 4	137 ± 9*	138 ± 2
Triglycerides [mg/dL]	1	73 ± 13	447 ± 142***	
	13	88 ± 39	302 ± 47**	303 ± 38*
Urea [mg/dL]	1	41.5 ± 2.1	51.0 ± 4.0**	
	13	46.9 ± 3.6*	45.2 ± 3.0*	46.8 ± 2.1

First, we compare the baselines, where plasma samples were taken before the start of the experiment for diabetic and healthy rats respectively, to evaluate if a diabetic

model was successfully implemented. Changes can be seen regarding ALT, which is significantly increased ($p < 0.001$) by 2-fold for diabetic rats. Further, GLDH, an indicator for liver damage, is significantly increased ($p < 0.05$) for diabetic rats by 6-fold as well as triglycerides ($p < 0.001$). Compared to healthy rats, also phosphate is significantly increased ($p < 0.05$) by 11% and urea ($p < 0.01$) by 23%. Lastly, creatinine, a kidney retention parameter, is significantly decreased ($p < 0.001$) by 30% as well as sodium ($p < 0.001$) by 13% for diabetic rats.

When comparing values for control and irradiated healthy rats, significant increases for AST by 36% ($p < 0.01$) and urea by 13% ($p < 0.05$) can be seen.

For diabetic controls, plasma parameters were compared before and after the experiment, to be able to estimate the influence of the experimental procedures. Decreases for ALT by 60% ($p < 0.05$), potassium by 21% ($p < 0.001$), triglycerides by 32% ($p < 0.01$) and urea by 11% ($p < 0.05$) can be noticed, as well as an increase in sodium concentration by 10% ($p < 0.05$).

The same effects can be seen when comparing irradiated diabetic rats to their control: there are decreases for ALT by 71% ($p < 0.01$), potassium by 20% ($p < 0.01$) and triglycerides by 32% ($p < 0.05$). In summary there are no differences between irradiated diabetic and control rats after the end of the experiment.

Additionally ELISA for rat CRP was performed (Figure 48).
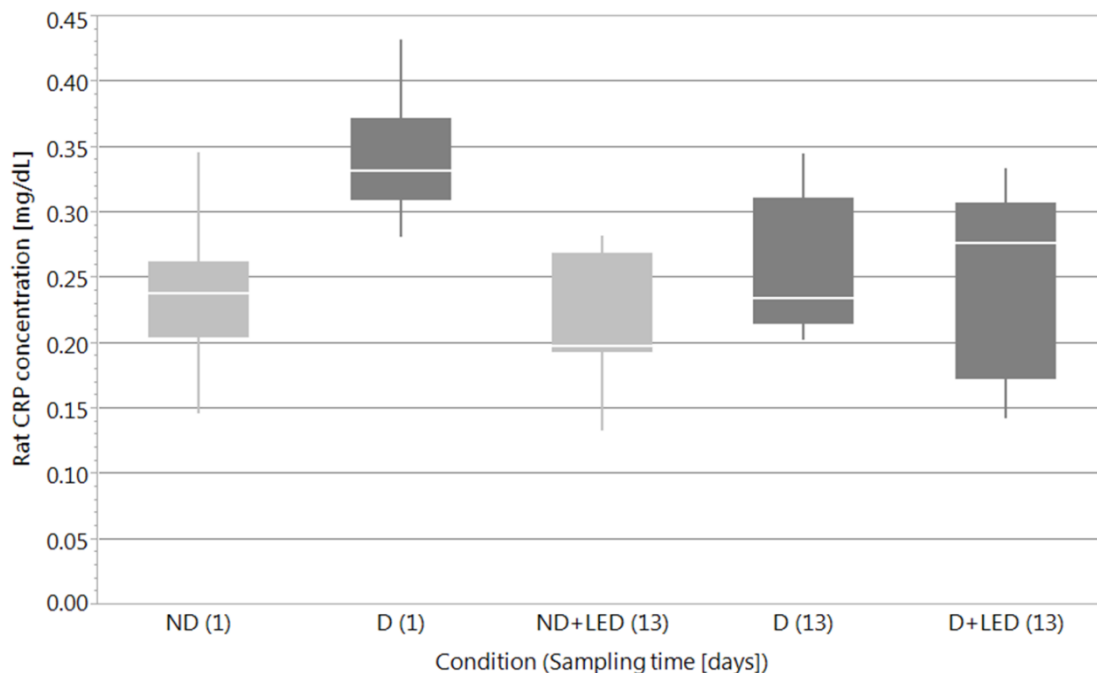
Figure 48: CRP concentration in rat plasma determined by ELISA of control (D) and light treated groups of diabetic rats (D+LED) and a light treated group of non-diabetic rats (ND+LED) in a long-term experiment. Samples were taken on day 1 and 13 indicated by the number in brackets. Data are shown as box plots with the median, upper and lower quartile (interquartile range (IQR)) and whiskers (1.5 x IQR). Each box plot represents n=6 plasma samples.

CRP results show significant differences between healthy and diabetic rats before the start of the experiment. While healthy rats have a normal CRP concentration of 0.24 mg/dL, the concentration of diabetic rats is increased to 0.33 mg/dL (i.e. +38%, $p < 0.0001$). Healthy rats do not show a significant difference after irradiation compared to their control. CRP concentrations of diabetic rats without treatment significantly drop to 23 mg/dL ($p < 0.001$) as well as for rats with light treatment to 28 mg/dL ($p < 0.001$). There is no significant difference between diabetic irradiated and control rats though.

Skin samples were taken from the wound site, embedded in paraffin, sliced and stained with H&E. Images were evaluated with the image segmentation software ilastik. First, thickness of the epidermis was compared between groups (Figure 49).
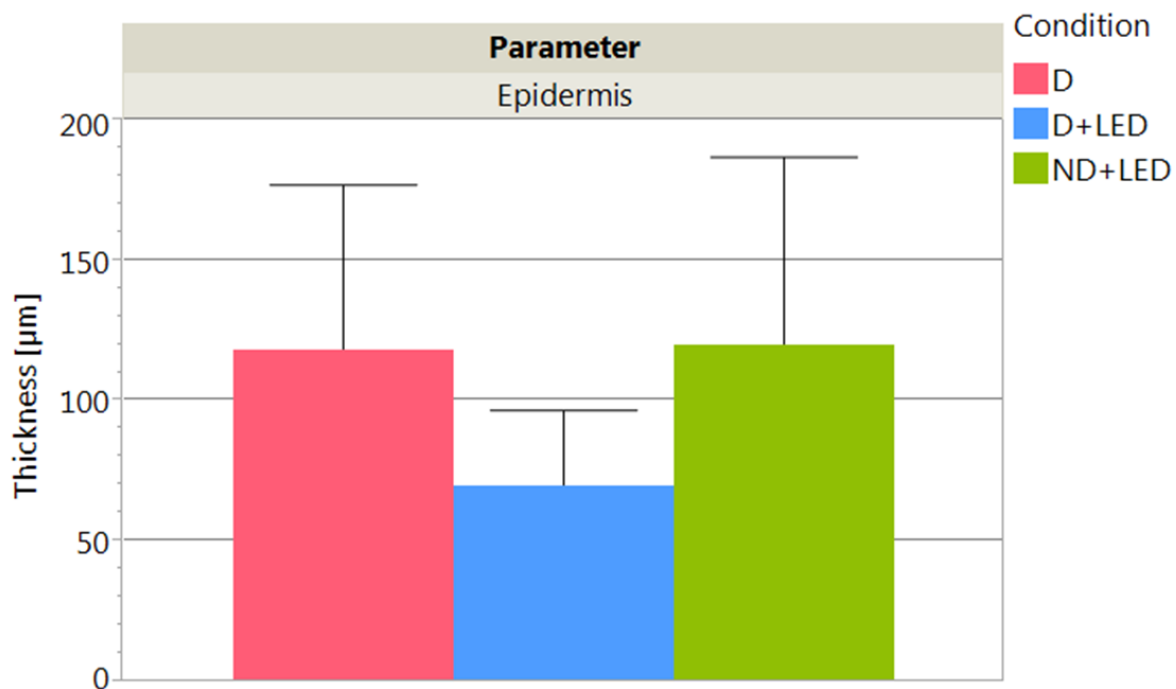
Figure 49: Results of image evaluation by ilastik segmentation. Data are displayed in µm with means ± SD. Each group represents values from n=6 animals.

The epidermal thicknesses of the groups do not differ significantly. A trend can be seen, where the skin of irradiated diabetic rats is slightly thinner ($p = 0.0983$) compared to non-irradiated rats. Thickness of the epidermis of non-diabetic rats that received light treatment is the same as for diabetic control rats, showing a similar difference compared to diabetic irradiated rats ($p = 0.0895$).

The inflammatory site of the injury was examined in respect to its area. Properties of identifying the inflammatory site were the lack of thick collagen fibers, increased

presence of leukocytes and fibrin. The areas of the different groups are compared in Figure 50.
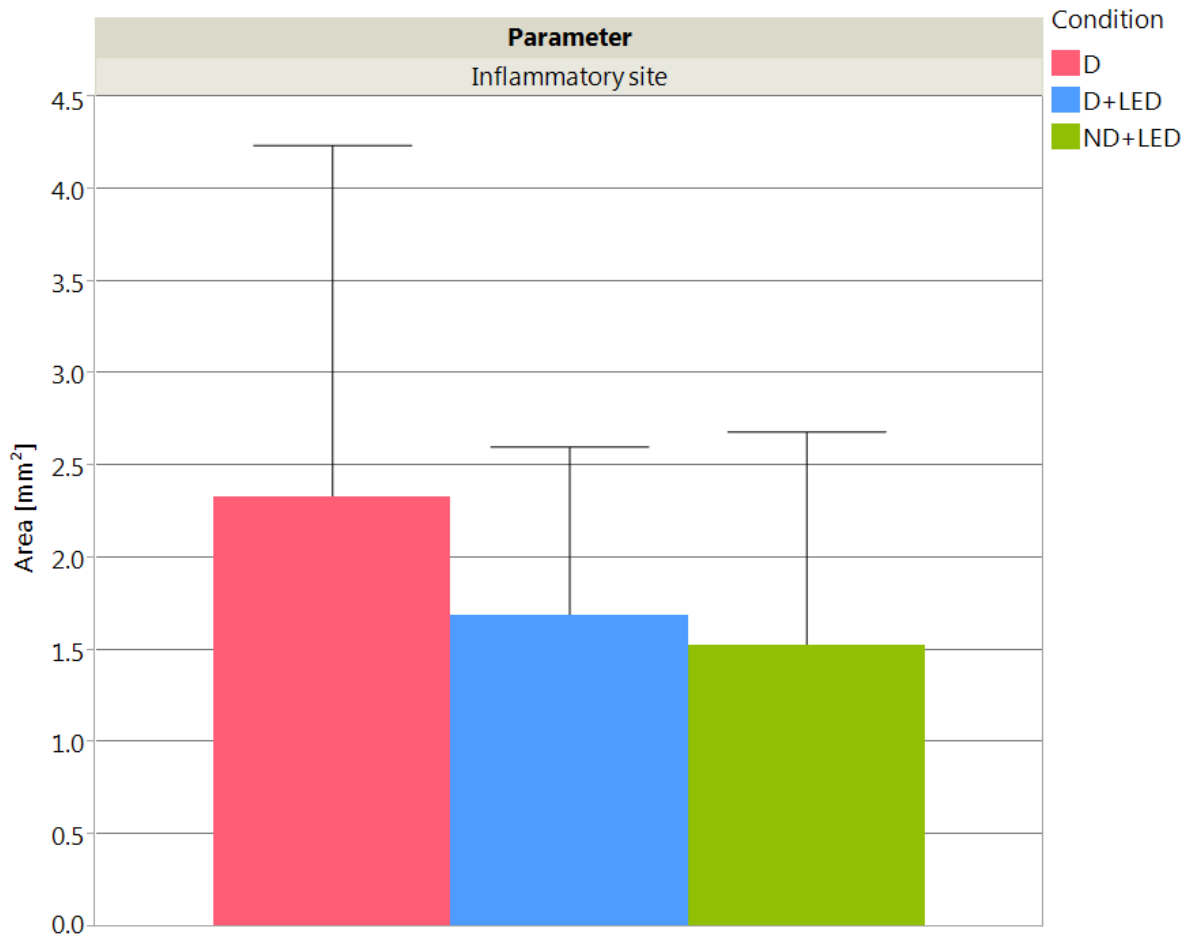
Figure 50: Results of image evaluation by ilastik segmentation. Data are displayed in mm² with means ± SD. Each group represents values from n=6 animals.

Areas of the groups do not differ significantly. Trends can be noticed, when groups of diabetic control and irradiated rats are compared.

In Figure 51 areas that are covered by fibrin and leukocytes are shown in relation to the inflammatory site.

For both parameters no significant changes can be detected, but again, trends can be identified. Both diabetic groups have the same area covered by fibrin with around 2%. The non-diabetic group has a lower fibrin content with only 0.5% (p = 0.0523).

For percentages of leukocytes a similar trend is observed, but again, without statistical significance.
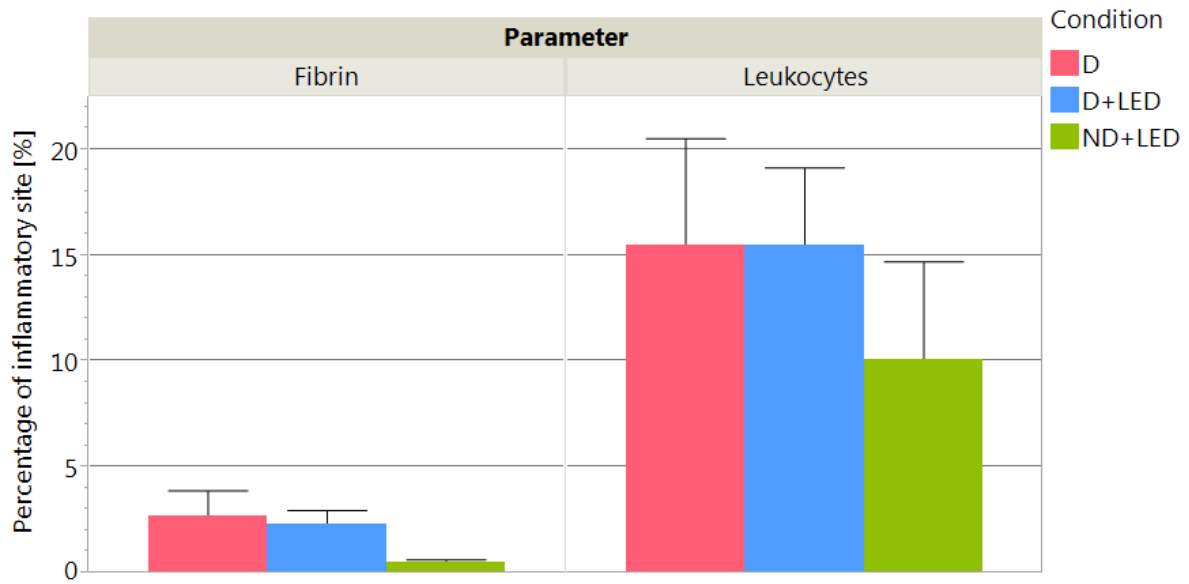
Figure 51: Results of image evaluation by ilastik segmentation. Data are displayed in % with means ± SD and were set in relation to the area of the inflammatory site of histological skin samples. Each group represents values from n=6 animals.

Another approach was tried to investigate possible differences between the groups, not considering the covered area by leukocytes, but the number of leukocytes in relation to the area (Figure 52).
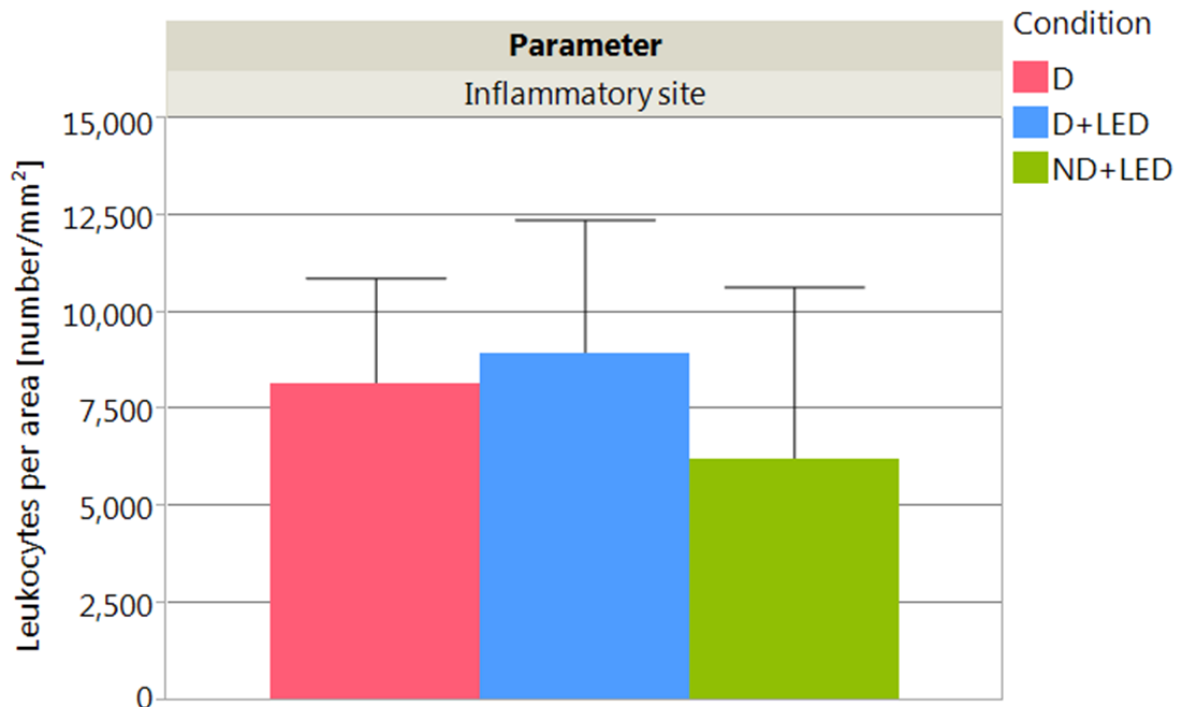
Figure 52: Results of image evaluation by ilastik segmentation Data are displayed in number per area in mm² with means ± SD in relation to the area of the respective inflammatory site. Each group represents values from n=6 animals.

Again, no statistical significance was detected.

No differences between non-irradiated wounds of irradiated animals and the control wounds of non-irradiated animals could be seen, therefore the data is not shown and no further analysis was pursued.

To study the effects of long-term blue light irradiation in detail, GSEA was performed by using the RNA of skin tissue samples. A ranked list was created and the number of significantly deregulated pathways were summarized in Table 16.

Only 3 genes were found to be significantly differentially expressed when comparing the diabetic control and diabetic light treated group. More pathways are up-regulated than down-regulated where 82 pathways are significantly up-regulated and 19 significantly down-regulated with an adjusted p-value of < 0.05.

Table 16: Overview of GSEA displaying the numbers of deregulated pathways for diabetic and non-diabetic rats treated with the complete light schedule. Genes were sorted in a total of 313 pathways. Fluorescence intensities of light treated samples are normalized to the control. Level of significances was defined as $p \leq 0.05$ for nominal and adjusted p-values (FDR ≤ 0.25) respectively.

	Diabetic control vs. Diabetic BL	Diabetic BL vs. Non-diabetic BL
Significantly differentially expressed genes	3	122
Significantly up-regulated genes	0	31
Pathways containing up-regulated genes	210	211
Significantly up-regulated pathways (nominal p-value < 0.05)	106	152
Significantly up-regulated pathways (adjusted p-value < 0.05)	82	143
Significantly down-regulated genes	3	91
Pathways containing down-regulated genes	103	102
Significantly down-regulated pathways (nominal p-value < 0.05)	26	48
Significantly down-regulated pathways (adjusted p-value < 0.05)	19	46

Comparing the diabetic light treated with the non-diabetic light treated group shows the same pattern, where more pathways are up-regulated than down-regulated. With a number of 122, more genes are significantly differentially expressed. Also more pathways are significantly up- and down-regulated, respectively, comparing by the adjusted p-value, but there are still more pathways up-regulated than down-regulated.

To better compare the deregulated pathways between the groups, the KEGG main categories were chosen as a criterion. The pathways are sorted into these 6 categories and separated by up- and down-regulation and the individual group comparisons (Figure 53).
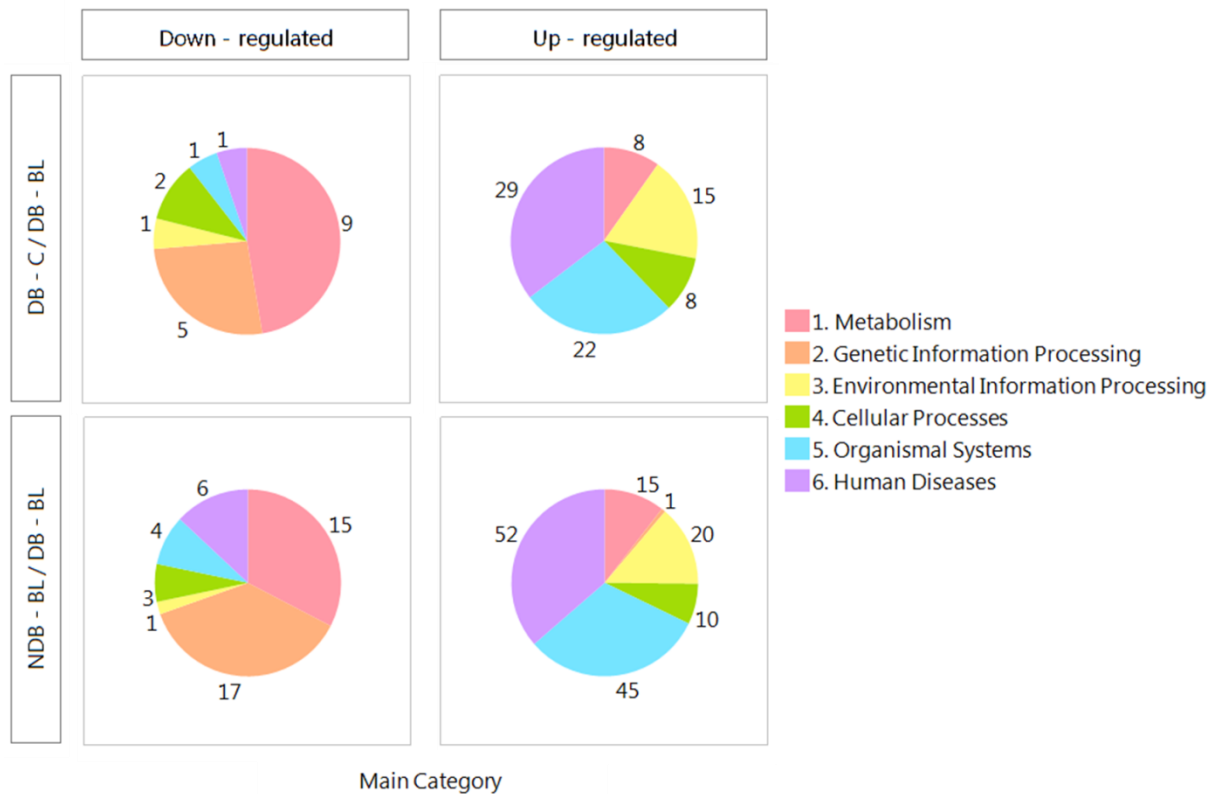
Figure 53: Pie chart showing the distribution of pathways containing significantly up- and down-regulated genes sorted by main categories of KEGG. Groups are formed by the respective conditions of diabetic (DB) or non-diabetic (NDB) rats and animals which received the light treatment (BL) or their control (C). The numbers around the pie charts indicate the number of deregulated pathways contained in each category.

In the comparison of control and light treated diabetic rats it is noticeable that most pathways are down-regulated belonging to the main categories 'Metabolism' and 'Genetic Information Processing' with 15 and 17 pathways. Mostly up-regulated pathways belong to the group of 'Organismal Systems' and 'Human Diseases' with 45 and 52 pathways. Also the categories of 'Metabolism', 'Environmental Information Processing' and 'Cellular Processes' have 10-20 up-regulated pathways.

When comparing the non-diabetic and diabetic light treated groups, the distribution of up- and down-regulated pathways between the categories is nearly the same, but with less individually deregulated pathways.

As only basic information can be gathered from this graph, summary tables were created, which indicate the deregulated pathways. The main categories were divided into KEGG's subcategories and the individual pathways shown.

Table 17 shows selected deregulated pathways of the main category 'Metabolism'; the complete list can be found in chapter '7 Appendix' in Table 24.

Table 17: Selected significantly deregulated pathways belonging to KEGG's main category 'Metabolism'. The main category is divided into 13 subcategories. Six of these categories were selected which contain significantly deregulated pathways. They are depicted with their respective NES and adjusted p-values. Up-regulated (Down-regulated) pathways are indicated by the positive (negative) NES colored in red (green). Comparisons were done by the respective conditions of diabetic (DB) or non-diabetic (NDB) rats and animals which received the light treatment (BL) or their control (C).

1. Metabolism	DB - C / DB - BL		NDB - BL / DB - BL	
	NES	Adjusted p-value	NES	Adjusted p-value
1.0. Global and overview maps				
Fatty acid metabolism	-1.76	0.0072	-1.67	0.0080
1.1. Carbohydrate metabolism				
Glycolysis and Gluconeogenesis	1.69	0.0173	-1.08	0.3913
Starch and sucrose metabolism	1.86	0.0102	0.87	0.6983
1.3. Lipid metabolism				
Steroid biosynthesis	-2.39	0.0055	-1.84	0.0040
Biosynthesis of unsaturated fatty acids	-2.07	0.0055	-1.10	0.3918
Fatty acid elongation	-1.94	0.0059	-1.38	0.1364
Steroid hormone biosynthesis	-1.82	0.0059	-0.64	0.9856
Sphingolipid metabolism	-1.67	0.0239	2.04	0.0012
Glycerolipid metabolism	1.63	0.0239	1.23	0.1437
1.4. Nucleotide metabolism				
Purine metabolism	1.54	0.0143	1.46	0.0162
1.6. Metabolism of other amino acids				
beta-Alanine metabolism	1.89	0.0086	0.94	0.6061
Glutathione metabolism	1.56	0.0409	-1.24	0.2056
1.7. Glycan biosynthesis and metabolism				
Mucin type O-glycan biosynthesis	1.97	0.0064	1.71	0.0151
Glycosylphosphatidylinositol (GPI)-anchor biosynthesis	-1.89	0.0084	-1.14	0.3513
Glycosaminoglycan biosynthesis	2.22	0.0012	2.22	0.0012

Many pathways were deregulated after long-term treatment with blue light. Where the fatty acid metabolism and nearly all pathways belonging to the lipid metabolism were found to be down-regulated, carbohydrate, nucleotide, amino acid and glycan metabolism were up-regulated. When comparing non-diabetic and diabetic light treated groups, only few pathways were significantly deregulated, e.g. fatty acid, steroid, sphingolipid, purine and glycan metabolism.

In the main category 'Genetic Information Processing' consisting of 4 subcategories, 3 were found to be significantly down-regulated. The affected pathways are the spliceosome, ribosome and its biogenesis, RNA degradation and proteasome. Changes in the fourth subcategory 'Replication and repair' were expected due to the

results of the short-term irradiation, but could only be found for the comparison of non-diabetic and diabetic light treated groups (full data set is shown in Table 25, chapter 7 Appendix)

Table 18: Selected significantly deregulated pathways belonging to KEGG's main category 'Genetic Information Processing'. The main category is divided into 4 subcategories. Three of these categories were selected which contain significantly deregulated pathways. They are depicted with their respective NES and adjusted p-values. Up-regulated pathways are indicated by the positive NES colored in red and down-regulated pathways are indicated by the negative NES colored in green. Comparisons were done by the respective conditions of diabetic (DB) or non-diabetic (NDB) rats and animals which received the light treatment (BL) or their control (C).

2. Genetic Information Processing	DB - C / DB - BL		NDB - BL / DB - BL	
	NES	Adjusted p-value	NES	Adjusted p-value
2.1. Transcription				
Spliceosome	-1.60	0.0096	-2.38	0.0012
2.2. Translation				
Ribosome	-1.89	0.0055	-2.60	0.0012
Ribosome biogenesis in eukaryotes	-1.68	0.0142	-2.30	0.0012
2.3. Folding, sorting and degradation				
RNA degradation	-1.75	0.0087	-2.12	0.0012
Proteasome	-1.70	0.0189	-2.25	0.0012

The category 'Environmental Information Processes' shows increases in expression patterns concerning signal transduction and signalling molecules (selected pathways are shown in Table 19, full data set is shown in Table 26, chapter 7 Appendix).

Table 19: Selected significantly deregulated pathways belonging to KEGG's main category 'Environmental Information Processes'. The main category is divided into 3 subcategories. Two of the categories contain significantly deregulated pathways, which are shown in the table with their respective NES and adjusted p-values. Up-regulated pathways are indicated by the positive NES colored in red and down-regulated pathways are indicated by the negative NES colored in green. Comparisons were done by the respective conditions of diabetic (DB) or non-diabetic (NDB) rats and animals which received the light treatment (BL) or their control (C).

3. Environmental Information Processes	DB - C / DB - BL		NDB - BL / DB - BL	
	NES	Adjusted p-value	NES	Adjusted p-value
3.2. Signal transduction				
Hippo signaling pathway	-1.93	0.0055	-1.25	0.1286
HIF-1 signaling pathway	1.76	0.0055	1.81	0.0012
TNF signaling pathway	1.99	0.0055	2.20	0.0012
FoxO signaling pathway	1.66	0.0055	1.31	0.0652
JAK-STAT signaling pathway	1.78	0.0055	2.16	0.0012
cAMP signaling pathway	1.60	0.0067	1.76	0.0012
MAPK signaling pathway	1.46	0.0074	1.70	0.0012
PI3K-Akt signaling pathway	1.42	0.0080	2.32	0.0012
Calcium signaling pathway	1.49	0.0096	1.41	0.0150
NF-kappa B signaling pathway	1.60	0.0156	2.49	0.0012

cGMP-PKG signaling pathway	1.49	0.0162	1.72	0.0012
Rap1 signaling pathway	1.41	0.0206	2.15	0.0012
Ras signaling pathway	1.37	0.0261	2.02	0.0012
3.3. Signaling molecules and interaction				
Viral protein interaction with cytokine and cytokine receptor	1.97	0.0055	2.92	0.0012
Cytokine-cytokine receptor interaction	1.53	0.0072	2.55	0.0012
Neuroactive ligand-receptor interaction	1.44	0.0096	1.33	0.0096

Conspicuously, TNF and NF-κB signaling pathways are up-regulated. Also, the calcium signaling pathway is up-regulated in the signal transduction. Here, MAPK and PI3K-Akt signaling pathway are up-regulated, too. Related to that, cytokine receptors and interaction seems to be affected by the long-term blue light treatment as well.

Table 20 shows the deregulated pathways in the main category 'Cellular Processes', where cell growth and death is deregulated (full data set is shown in Table 27, chapter 7 Appendix). Cell cycle pathways are down-regulated, whereas apoptosis, necroptosis and ferroptosis are up-regulated.

Linked to the immune response, affected pathways can be found in the subcategory 'Transport and catabolism'. Here, phagosome, lysosome and autophagy pathways are up-regulated.

Table 20: Selected significantly deregulated pathways belonging to KEGG's main category 'Cellular Processes'. The main category is divided into 5 subcategories. Three of the categories contain significantly deregulated pathways, which are shown in the table with their respective NES and adjusted p-values. Up-regulated pathways are indicated by the positive NES colored in red and down-regulated pathways are indicated by the negative NES colored in green. Comparisons were done by the respective conditions of diabetic (DB) or non-diabetic (NDB) rats and animals which received the light treatment (BL) or their control (C).

4. Cellular Processes				
	DB - C / DB - BL		NDB - BL / DB - BL	
	NES	Adjusted p-value	NES	Adjusted p-value
4.1. Transport and catabolism				
Peroxisome	-1.74	0.0096	-1.63	0.0078
Autophagy	1.52	0.0156	-1.48	0.0683
Lysosome	1.50	0.0188	2.89	0.0012
Phagosome	1.40	0.0394	2.68	0.0012
4.2. Cell growth and death				
Cell cycle	-1.80	0.0055	-2.08	0.0012
Apoptosis	1.69	0.0055	2.26	0.0012
Necroptosis	1.60	0.0064	1.81	0.0012
Ferroptosis	1.76	0.0162	1.43	0.0708
4.3. Cellular community				
Focal adhesion	1.83	0.0055	2.64	0.0012

Up-regulated pathways that are related to the immune response can also be found in the main category 'Organismal Systems' (Table 21, full data set is shown in Table 28, chapter 7 Appendix) including toll-like and NOD-like receptors. Many more immunological pathways are up-regulated, but also pathways involved in adipocyte metabolism are affected. The up-regulation of lipolysis can be noticed here, and also the adipocytokine signaling pathway is strongly active.

The nervous system shows effects as well, where the neurotrophin signaling pathway is up-regulated.

Table 21: Selected significantly deregulated pathways belonging to KEGG's main category 'Organismal Systems'. The main category is divided into 10 subcategories. Three of the categories contain significantly deregulated pathways, which are shown in the table with their respective NES and adjusted p-values. Up-regulated pathways are indicated by the positive NES colored in red and down-regulated pathways are indicated by the negative NES colored in green. Comparisons were done by the respective conditions of diabetic (DB) or non-diabetic (NDB) rats and animals which received the light treatment (BL) or their control (C).

5. Organismal Systems	DB - C / DB - BL		NDB - BL / DB - BL	
	NES	Adjusted p-value	NES	Adjusted p-value
5.1. Immune system				
Toll-like receptor signaling pathway	1.94	0.0055	2.17	0.0012
Natural killer cell mediated cytotoxicity	1.84	0.0055	2.06	0.0012
Chemokine signaling pathway	1.75	0.0055	2.72	0.0012
NOD-like receptor signaling pathway	1.64	0.0055	2.25	0.0012
Complement and coagulation cascades	1.78	0.0084	2.69	0.0012
Hematopoietic cell lineage	1.67	0.0119	2.77	0.0012
B cell receptor signaling pathway	1.70	0.0142	1.94	0.0012
Intestinal immune network for IgA production	1.67	0.0239	2.3	0.0012
Fc epsilon RI signaling pathway	1.60	0.0239	1.82	0.0015
IL-17 signaling pathway	1.55	0.0265	1.87	0.0012
5.2. Endocrine system				
Prolactin signaling pathway	1.82	0.0102	1.58	0.0138
Regulation of lipolysis in adipocytes	1.79	0.0124	2.02	0.0012
Adipocytokine signaling pathwaay	1.72	0.0164	1.33	0.0922
Glucagon signaling pathway	1.53	0.0241	1.03	0.4437
Aldosterone synthesis and secretion	1.50	0.0293	1.78	0.0023
5.6. Nervous system				
Neurotrophin signaling pathway	1.43	0.0386	1.57	0.0074

Even if they are connected to human diseases, pathways belonging to this main category were summarized in Table 22, as they could give an overview of which underlying effects the blue light treatment could be linked to (full data set is shown in Table 29, chapter 7 Appendix). Pathways of inflammatory diseases or infections as rheumatoid arthritis, atherosclerosis, Yersinia or human cytomegalovirus are

affected. The pathway of hypertrophic cardiomyopathy was up-regulated, which is linked to calcium sensitivity.

Table 22: Selected significantly deregulated pathways belonging to KEGG's main category 'Human Diseases'. The main category is divided into 12 subcategories. Seven of the categories contain significantly deregulated pathways, which are shown in the table with their respective NES and adjusted p-values. Up-regulated pathways are indicated by the positive NES colored in red and down-regulated pathways are indicated by the negative NES colored in green. Comparisons were done by the respective conditions of diabetic (DB) or non-diabetic (NDB) rats and animals which received the light treatment (BL) or their control (C).

6. Human Diseases	DB - C / DB - BL		NDB - BL / DB - BL	
	NES	Adjusted p-value	NES	Adjusted p-value
6.3. Immune diseases				
Rheumatoid arthritis	1.94	0.0059	2.85	0.0012
6.6. Cardiovascular diseases				
Fluid shear stress and atherosclerosis	1.96	0.0055	2.02	0.0012
Hypertrophic cardiomyopathy (HCM)	1.51	0.0328	1.42	0.0335
6.7. Endocrine and metabolic diseases				
AGE-RAGE signaling pathway in diabetic complications	2.02	0.0055	2.47	0.0012
6.8. Infectious diseases: Bacterial				
Yersinia infection	1.89	0.0055	2.20	0.0012
6.9. Infectious diseases: Viral				
Human cytomegalovirus infection	1.59	0.0058	2.18	0.0012
6.10. Infectious diseases: Parasitic				
Malaria	2.00	0.0059	2.87	0.0012
African trypanosomiasis	1.88	0.0086	2.26	0.0012
6.12. Drug resistance: Antineoplastic				
EGFR tyrosine kinase inhibitor resistance	1.48	0.0487	1.96	0.0012

All in all, many significantly deregulated pathways could be found. Some patterns can be seen by comparing the different categories of affected gene sets, but mainly they seem to belong to the same related cellular functions. These include cell proliferation, cellular repair mechanisms, apoptosis and inflammatory processes.

3.2 EU project MEDILIGHT: prototype development, testing of efficacy – *in vitro* and *in vivo*, including temperature sensor testing

To be able to apply the findings of the previous studies on patients, a device was developed during the EU-project MEDILIGHT. The goal was to transfer the effects seen *in vitro* and *in vivo* to humans. In the following subchapter different optimization and improvement steps are shown, as well as solutions to problems that occurred during testing.

3.2.1 Developing the set-up of the MEDILIGHT prototype

First MEDILIGHT prototypes consisted of boards with different numbers and distances between the LEDs. With XTT assays it was determined that the optimal distance between LEDs was 5 mm (data not shown). From these LED boards progress was made by constructing flexible foils with printed wiring and embedded LEDs. The first prototypes were tested *in vitro* and compared to the Philips lamp, (Figure 54).
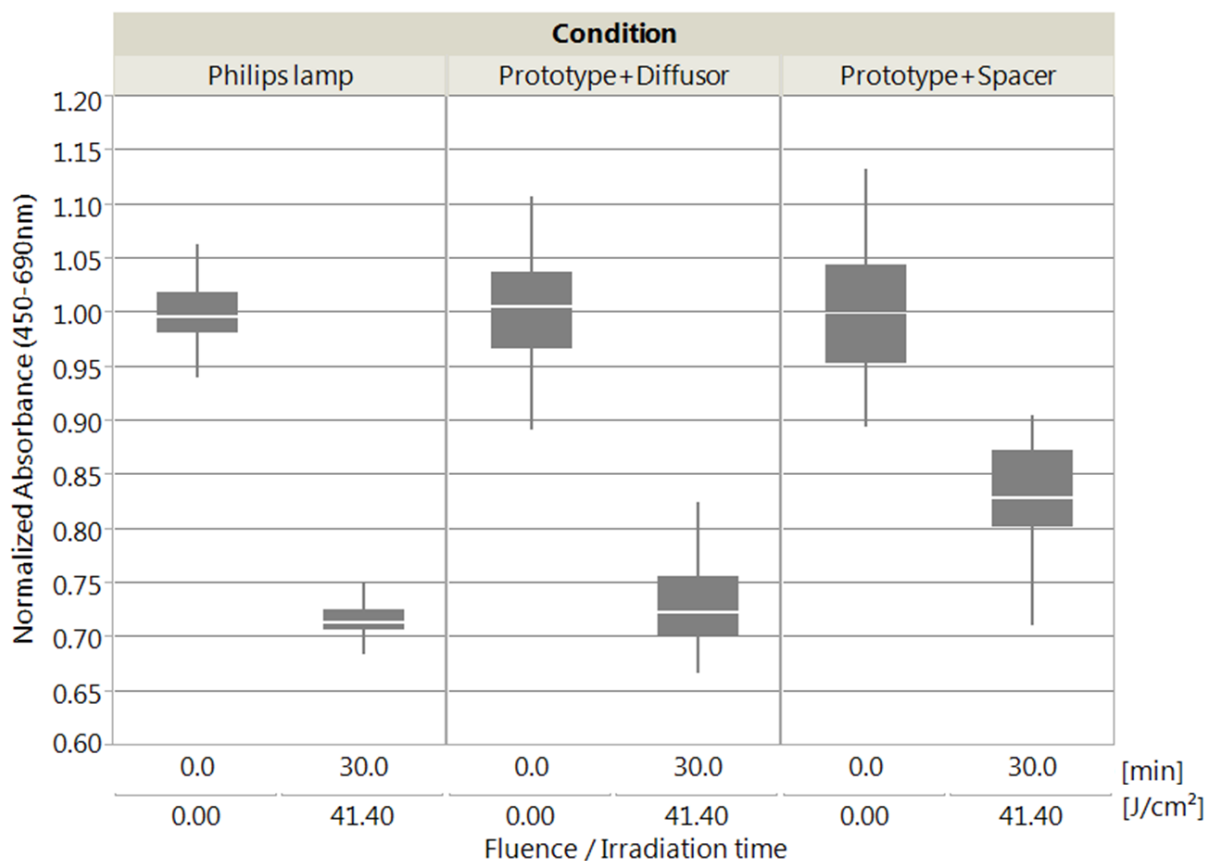
Figure 54: XTT results of keratinocytes irradiated with 41.40 J/cm² of blue light using the Philips lamp and MEDILIGHT prototypes, respectively. Assay was performed 24 h after irradiation. For experiments with prototypes a diffusor and spacer were included in the set-up. Data are shown as box plots with the median, upper and lower quartile (interquartile range (IQR)) and whiskers (1.5 x IQR). Each box plot represents n=3 plates.

For one of the set-ups a diffusor was used to create a more homogenous field of irradiation, as in previous experiments a lack thereof was noticed. Also with the use of a spacer that creates a distance of 5 mm to the plate surface, another set-up was tested. Evaluation area had to be adjusted for prototype experiments, as the irradiated area is smaller.

Irradiation with 41.40 J/cm² of blue light with the Philips lamp shows a significant decrease in metabolic activity by nearly 30% (p < 0.0001). The irradiation with MEDILIGHT prototype including the diffusor shows a similar effect (p < 0.0001).

When using the spacer with the MEDILIGHT prototype, the effect of irradiation is smaller with a significant decrease by 17% (p < 0.0001).

For further experiments the diffusor was included into the set-up with the prototypes, to have stable results, comparable to the effects of the Philips lamp. Different irradiation times were tested to prove the efficacy of the prototype (data not shown). As for the use case 'diabetic foot ulcer' a wound dressing should be used, it was attempted to replace the diffusor by a wound dressing that also has the ability to scatter light. The use of the prototype in combination with the wound dressing E2723 was compared to the prototype with the diffusor (Figure 55).
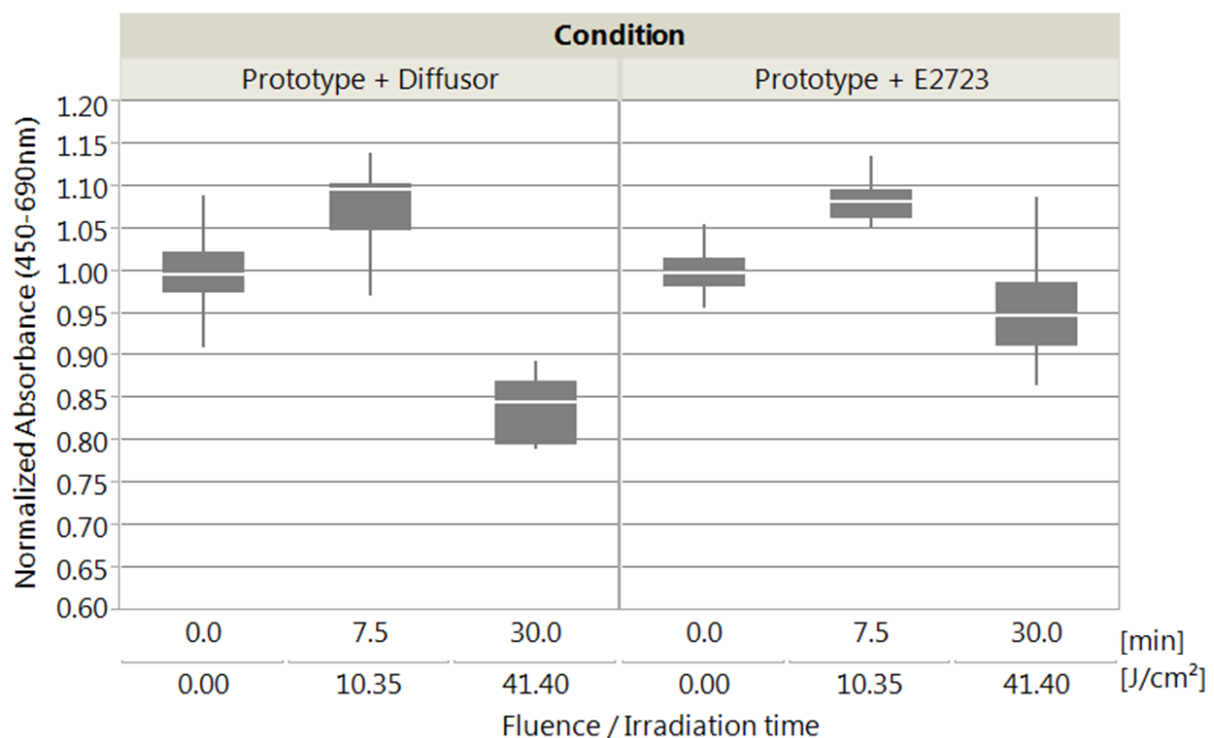
Figure 55: XTT results of keratinocytes irradiated with 10.35 and 41.40 J/cm² of blue light using MEDILIGHT prototypes. Assay was performed 24 h after irradiation. Comparative experiments between set-ups using a diffusor and the wound dressing E2723 were performed. Data are shown as box plots with the median, upper and lower quartile (interquartile range (IQR)) and whiskers (1.5 x IQR). Each box plot represents n=3 plates.

Results show a significant increase (p < 0.0001) by 10% for metabolic activity after irradiation with a fluence of 10.35 J/cm² of blue light, when using the prototype with the diffusor. With 41.40 J/cm² of blue light a significant decrease (p < 0.0001) in metabolic activity is observed, which is comparable to results from previous experiments (Figure 54) and results from the Philips lamp. When the prototype is used with the wound dressing E2723, a significant increase (p < 0.0001) by 8% in metabolic activity is observed after irradiation with 10.35 J/cm². There is also a

significant decrease (p < 0.0001) in metabolic activity after irradiation with 41.40 J/cm². But the extent of the decrease is lower than for all other experiments, accounting to a reduction by only 5%.

While the irradiation with 10.35 J/cm² showed to be effective, irradiation with 41.40 J/cm² had a reduced effect on cells. Therefore in future experiments, irradiation times had to be increased to obtain the desired effects.

3.2.2 Temperature sensor testing *in vitro* and vivo

After it was decided which components were necessary in the set-up for the MEDILIGHT prototype, the efficacy of the LEDs was tested. During these experiments it was noticed that the flexible foil was developing heat, rising so high that skin cells died during *in vitro* testing. To determine the extent of this heat development, experiments on a skin polymer model were performed. For that the skin polymer model was placed on a heating plate, with 35°C to simulate the body's core temperature. The flexible LED foil was placed on top and the temperature was tracked over 45 min (Figure 56).
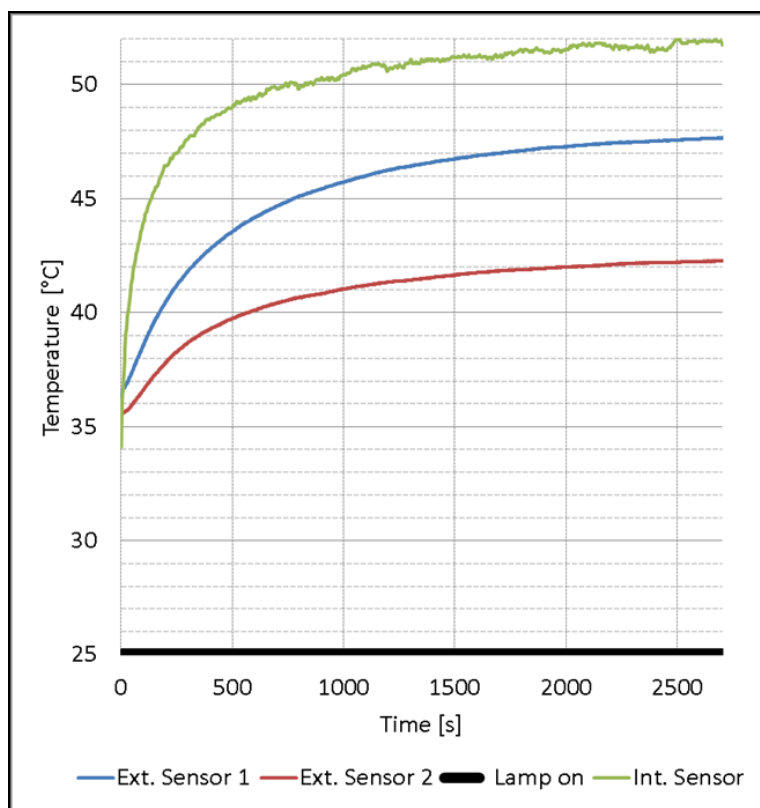
Diffusor	+
Backreflector	+
Irradiance	23 mW/cm²
Duty cycle	46%
Irradiation mode	continuous

Figure 56: Temperature measurement on skin polymer model during irradiation with the MEDILIGHT prototype. The irradiance was adjusted to 23 mW/cm² for which a duty cycle of 46% was necessary. Back reflector and diffusor were integrated into the set-up. The internal sensor is displayed in green, located on the flexible LED foil, while the two external sensors are between the wound dressing and the skin polymer model, one in the middle (blue) and one on the rim (red).

The maximum temperature on the flexible foil rises to 52°C during irradiation, while the temperature in the center of the skin polymer model reaches around 47°C. The temperature at the rim of the skin polymer model stays relatively low with a temperature of 42°C, compared to the center.

One approach to overcome this problem was to cycle the irradiation by turning the LEDs on for 1 min, followed by 1 min off (Figure 57).

Diffusor	+
Backreflector	+
Irradiance	23 mW/cm²
Duty cycle	46%
Irradiation mode	1 minute alternation
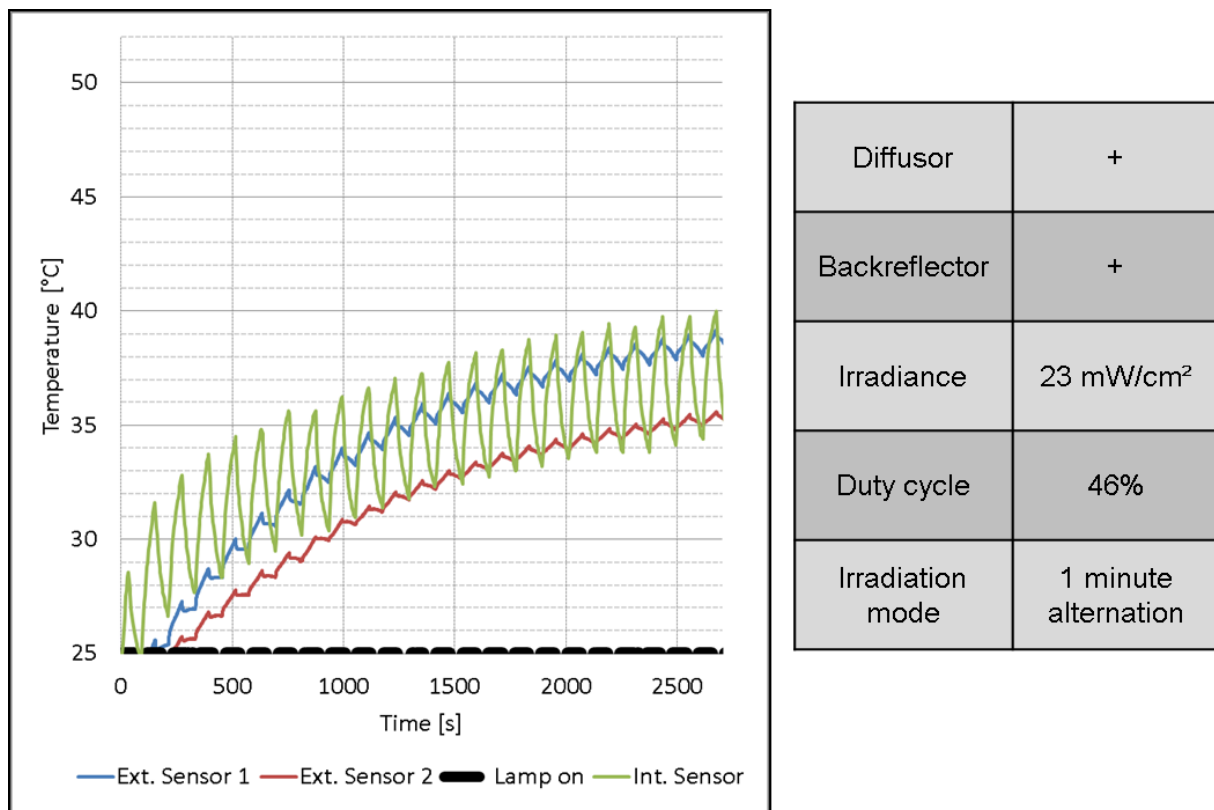
Figure 57: Temperature measurement on skin polymer model during irradiation with the MEDILIGHT flexible LED foil. The irradiance was adjusted to 23 mW/cm² for which a duty cycle of 46% was necessary. Back reflector and diffusor were integrated into the set-up. Green shows the internal sensor, located on the flexible LED foil, while the two external sensors are between the wound dressing and the skin polymer model, one in the middle (blue) and one on the rim (red). A cycle mode of 1 min on and 1 min off was used.

This approach leads to satisfying results, as a maximum temperature of only 40°C is reached for the internal sensor of the MEDILIGHT prototype. The cycling of the LEDs can also be followed by examining the results of the 2 external sensors that have the same pattern of increases and decreases in temperature. For the central external sensor the maximum temperature at the end of the measurement is 39°C and for the second external sensor on the rim it rises to 36°C.

For the MEDILIGHT App an additional feature was programmed, so that the LEDs turn on and off automatically in dependence to the temperature. A minimal and maximal temperature could be chosen, which was decided to be 37°C and 40°C (Figure 58).

Diffusor	+
Backreflector	+
Irradiance	23 mW/cm²
Duty cycle	46%
Irradiation mode	Shutdown at 40°C
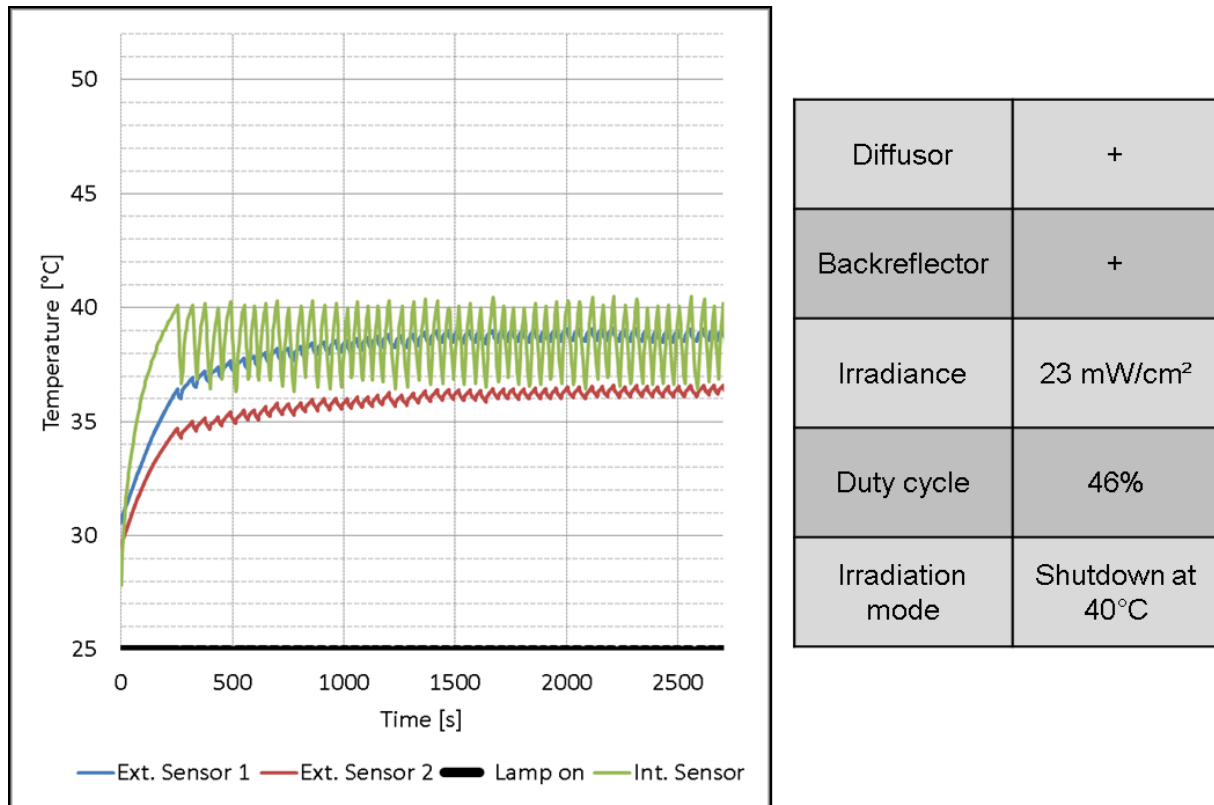
Figure 58: Temperature measurement on skin polymer model during irradiation with the MEDILIGHT flexible LED foil. The irradiance was adjusted to 23 mW/cm² for which a duty cycle of 46% was necessary. Back reflector and diffusor were integrated into the set-up. Green shows the internal sensor, located on the flexible LED foil, while the two external sensors are between the wound dressing and the skin polymer model, one in the middle (blue) and one on the rim (red). A cycle mode was used, where a minimum temperature of 37°C and a maximum temperature of 40°C were chosen.

The curve of the flexible foil shows that the temperature of the flex foil stays between the assigned temperatures. Also the internal external sensor stays at a non-critical temperature of 39°C, as well as the second external sensor with a temperature of 36.5°C. After this safety feature was integrated, the experiments were extended to *in vivo* testing on porcine skin.

For the first experiments on porcine skin, 4 prototypes were attached to the flank of the pig. Two of these prototypes were placed over a wound dressing E2723 and fixed with a pocket. The two other prototypes were attached with the adhesive pocket on the skin surface, but without a wound dressing. One prototype of each group was started and the temperature tracked (Figure 59).

The device was run in cycled mode. Nevertheless there are no cycles while irradiating for around 1 hour. This means that the maximum temperature that was adjusted to 40°C was never reached. The temperature measured at the center of the LED flex foil reaches a maximum of 37°C and also the temperature of the external sensor stays at around 36.5°C.
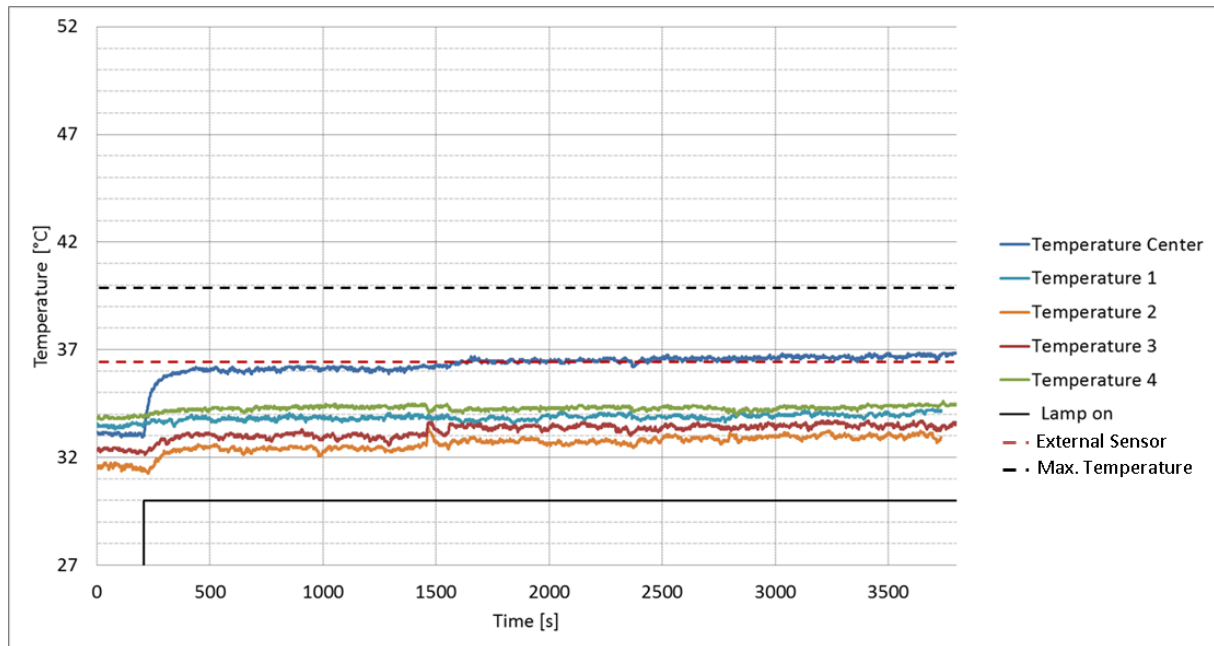
Figure 59: Temperature measurements on porcine skin with the MEDILIGHT prototype and the pocket. An irradiance of 23 mW/cm² was adjusted with a duty cycle of 20%. Five different sensors of the prototype are shown, with one central sensor and four sensors located at the rim (Sensor 1-4). The maximum temperature in the program was adjusted to 40°C which is indicated by the broken black line. An external sensor was placed under the prototype. Its temperature is represented by the broken red line. The on/off-time of the lamp is indicated by the discontinuous black line.

These results show that the temperatures of the LED flex foil and on the surface of the skin are similar, so the sensors are able to measure the temperature correctly. Further tests were performed with the use of the wound dressing E2723 provided by URGO (developed for MEDILIGHT) (Figure 60).
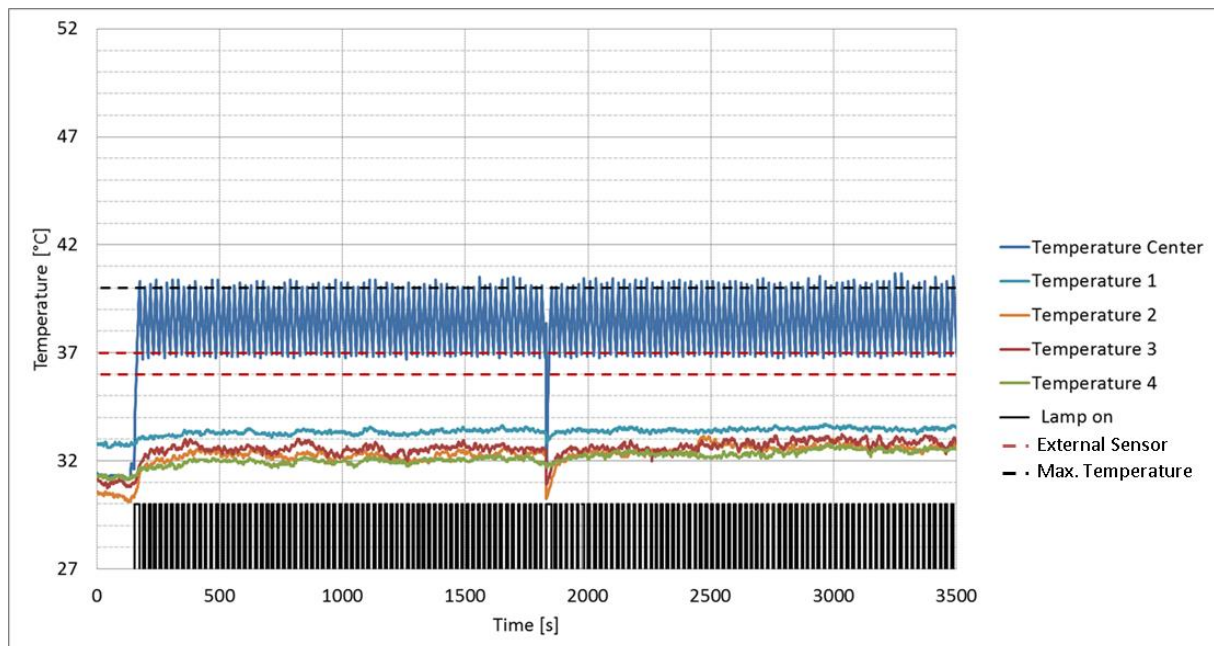
Figure 60: Temperature measurements on porcine skin with the MEDILIGHT prototype, wound dressing E2723 and the pocket. An irradiance of 23 mW/cm² was adjusted with a duty cycle of 62%. Five different sensors of the prototype are shown, with one central sensor and four sensors located at the rim (Sensor 1-4). The maximum temperature in the program was adjusted to 40°C which is indicated by the broken black line. An external sensor was placed under the prototype. Its temperature is represented by the broken red line. The on/off-time of the lamp is indicated by the discontinuous black line.

80

The irradiation scheme looks quite different than in the previous measurement (Figure 59). The duty cycle had to be adjusted to 62% due to the inclusion of the wound dressing. Therefore the temperature rises higher compared to the previous graph and due to that, cycling is necessary. The cycling is indicated by the discontinuous black line ('lamp on'), where the cycles are visible. Also the temperature is fluctuating between the maximum and minimum temperature. The external sensor shows a fluctuation of temperature between 36°C and 37°C. This is represented by the 2 horizontal broken red lines.

The patterns were analyzed and it was found that cycles consist of 8 s on-time and 10 s off-time at the beginning of the measurement. At the end of the experiment the off-time increases to 13 s, meaning that there is a slight heat build-up over time. Fortunately the App can compensate for that, so that in the long run the temperature stays stable under 40°C.

After irradiating the skin with the different set-ups, images of the porcine skin were taken and compared to the images before the start of the experiment (Figure 61).
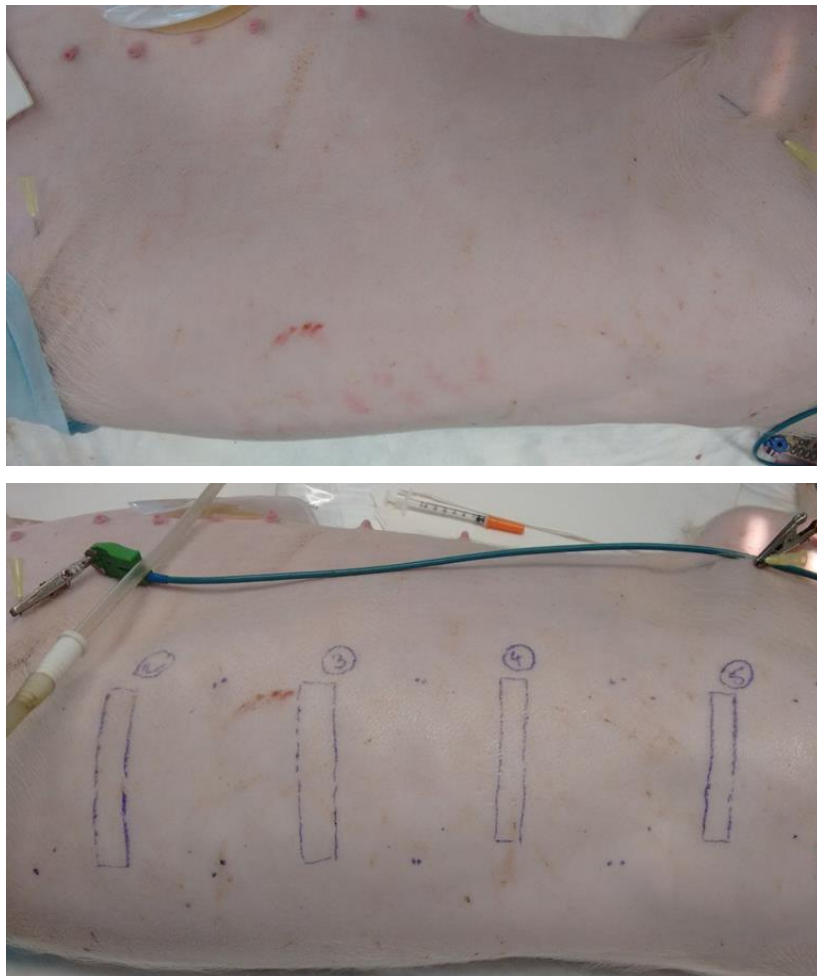
Figure 61: MEDILIGHT prototype, visual comparison of porcine skin before and after irradiation.

There is no difference between the images; especially no hyperemia is visible, which could be a possible side effect.

Due to the fact that the temperature on the surface of the skin is at a reasonable 37°C, further tests with increased maximum temperature were performed. The maximum temperature of one of the prototypes was increased to 42°C to possibly increase the on-times of the cycles and therefore reduce the total treatment time (Figure 62).
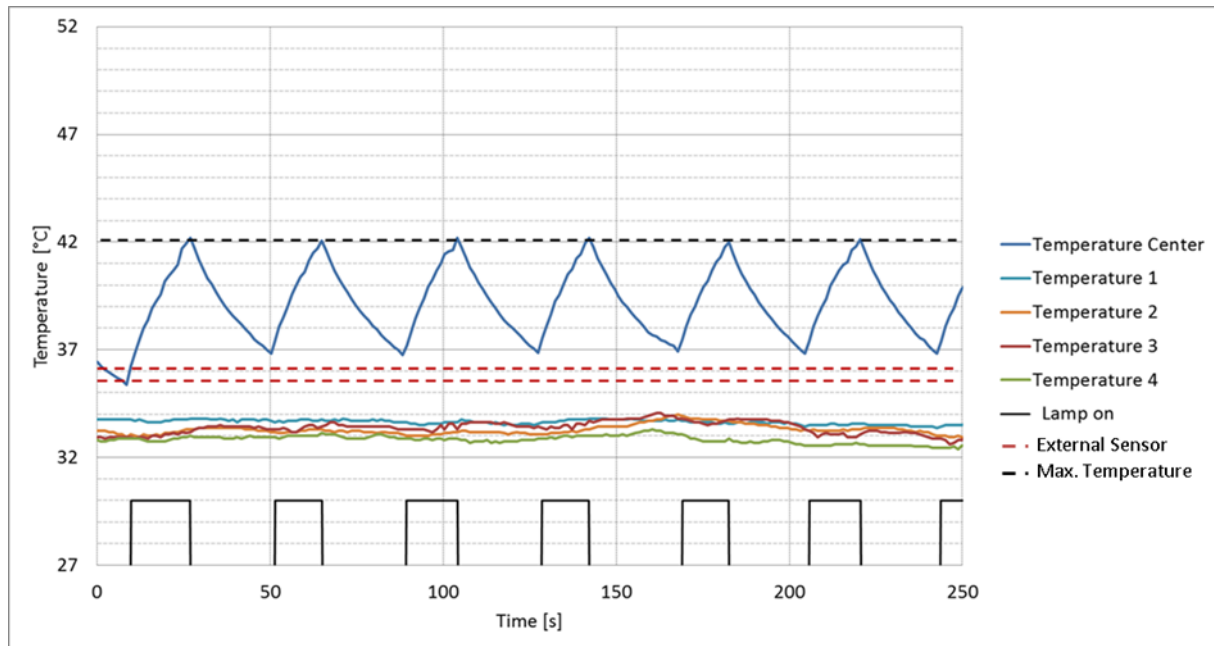
Figure 62: Temperature measurements on porcine skin with the MEDILIGHT prototype, wound dressing E2723 and the pocket. An irradiance of 23 mW/cm² was adjusted with a duty cycle of 62%. Five different sensors of the prototype are shown, with one central sensor and four sensors located at the rim (Sensor 1-4). The maximum temperature in the program was adjusted to 42°C which is indicated by the broken black line. An external sensor was placed under the prototype. Its temperature is represented by the broken red line. The on/off-time of the lamp is indicated by the discontinuous black line.

By changing the maximum temperature the cycles change as well. The on/off-cycle at the beginning of the measurement is 17 s on-time and 21 s off-time which changes to 15 s on-time and 22 s off-time towards the end of the measurement. While irradiating with a higher maximum temperature, the temperature measured by the external sensor is not rising. It stays below 37°C, with the maximum and minimum indicated by the broken red line.

As the temperature is still at a tolerable level, the maximum temperature was increased further to 45°C (Figure 63).

Again, the cycling scheme changes, with the on-time of 31 s and the off time 29 s. Still, the measured temperature of the external sensor does not seem to rise significantly and stays below 37°C. For this pulsing scheme the on/off-times are quite similar and the temperature does not exceed the specified maximum of 40°C. In

conclusion, it was decided that this scheme was used for *in vitro* tests with the prototype, because it does not cause overheating and is the easiest to adjust and calculate with.
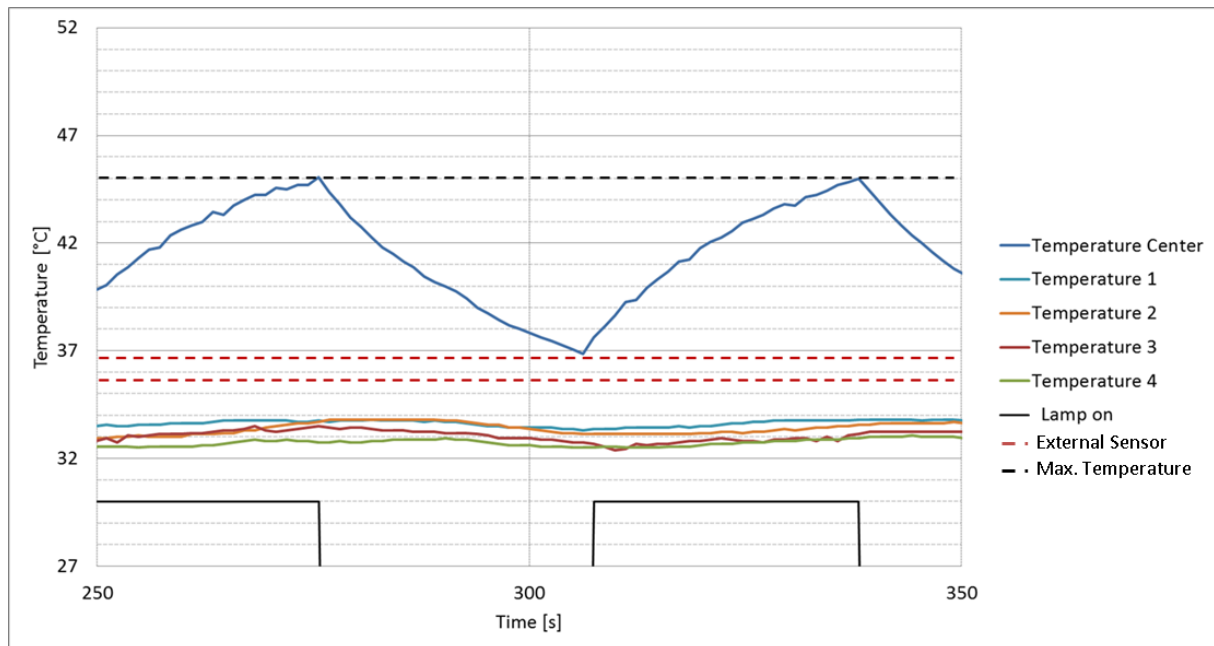
Figure 63: Temperature measurements on porcine skin with the MEDILIGHT prototype, wound dressing E2723 and the pocket. An irradiance of 23 mW/cm² was adjusted with a duty cycle of 62%. Five different sensors of the prototype are shown, with one central sensor and four sensors located at the rim (Sensor 1-4). The maximum temperature in the program was adjusted to 45°C which is indicated by the broken black line. An external sensor was placed under the prototype. Its temperature is represented by the broken red line. The on/off-time of the lamp is indicated by the discontinuous black line.

After the experiments were finished, skin samples from the irradiated area were taken, histological slides created and the different conditions compared (Figure 64).
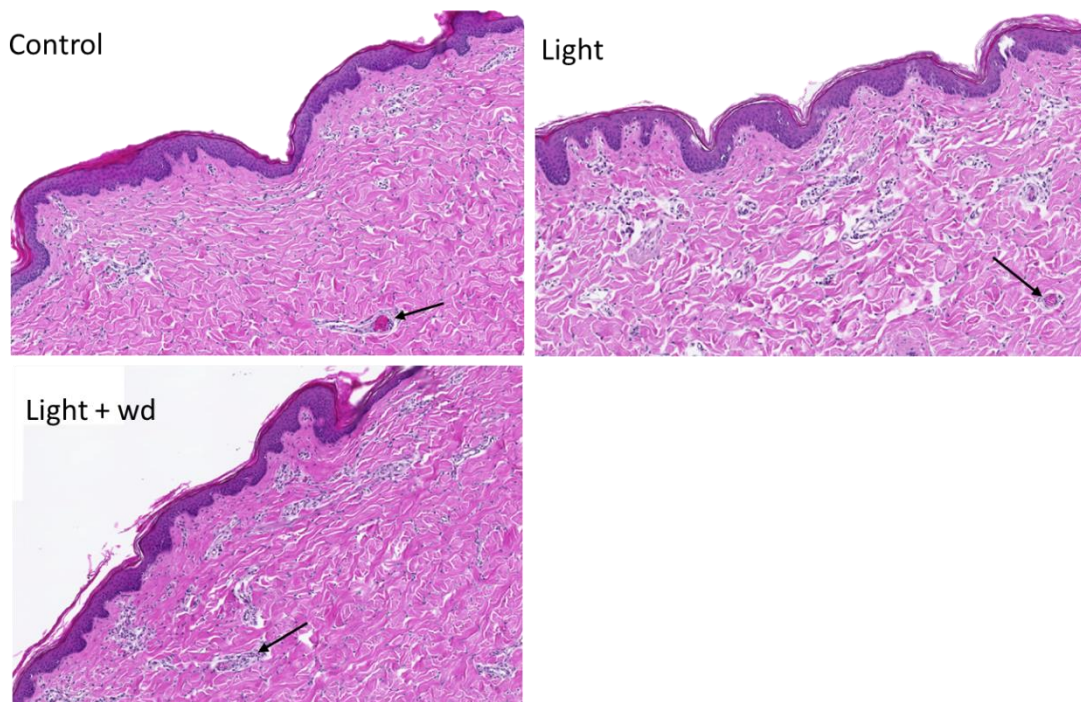
Figure 64: Histology of porcine skin stained with H&E. Arrows show vessels filled with blood. Images from control, light treated and light treated porcine skin through a wound dressing (wd) are shown.

No differences can be seen between all three images. There is no inflammation in irradiated skin samples, as indicated by the absence of neutrophil leukocytes. The epidermal layer is intact for all samples and no vasodilation can be observed, indicated by the arrows.

After these experiments ensured that there are no safety risks, additional adjustments to the prototype were applied. Silicone encapsulation was added to the flexible LED foil to seal the LEDs from sweat and bacteria. With the encapsulation it becomes easier to disinfect the device, making it reusable for one patient. Also the battery was changed to a model with higher capacity and a copper backing was added, to further increase heat dissipation. As these changes were made and the new cycled mode of irradiation was decided upon, the efficacy of the prototype had to be tested again.

3.2.3 Prototype testing – MEDILIGHT prototype *in vitro*

After deciding the final set-up of the prototype and the parts that needed to be included, the prototypes efficacy had to be tested. With the wound dressing, the silicon encapsulation and the back reflector experiments using mixed cultures of keratinocytes and fibroblasts were performed. The experiments were conducted as close to reality as possible, therefore pulsed mode with on/off times of 30 s was used and it was irradiated through the wound dressing E2723. The results were compared to the results of the Philips lamp, without any additions (Figure 65).

The results show a similar biphasic dose-response curve for the MEDILIGHT prototype as for the Philips lamp. For the Philips lamp the highest metabolic activity with a significant increase ($p < 0.0001$) of 5% is observed when irradiation with 10.35 J/cm² takes place. This differs for the prototype, where the peak is reached when applying a dose of 20.7 J/cm² with a significant increase ($p < 0.05$) by 10% compared to the control.

Similarly, the lowest metabolic activity is observed for 82.80, 124.20 and 165.60 J/cm² with a significant decrease ($p < 0.0001$) of metabolic activity by 25% for the Philips lamp and by 20% for 124.20 and 165.60 J/cm² for the MEDILIGHT prototype.

Therefore, the graph for the prototype is shifted to the right to higher fluences, so that it has to be irradiated longer or with higher power density to reach the same effects as for the Philips lamp.

Level -	Level	Prototype p-value	Philips p-value
10.35	0	<.0001*	<.0001*
20.7	0	0.0458*	<.0001*
41.4	0	<.0001*	0.1017
62.1	0	<.0001*	<.0001*
82.8	0	<.0001*	<.0001*
124.2	0	<.0001*	<.0001*
165.6	0	<.0001*	<.0001*
20.7	10.35	<.0001*	0.0137*
41.4	10.35	<.0001*	0.0072*
62.1	10.35	<.0001*	<.0001*
82.8	10.35	<.0001*	<.0001*
124.2	10.35	<.0001*	<.0001*
165.6	10.35	<.0001*	<.0001*
41.4	20.7	<.0001*	<.0001*
62.1	20.7	<.0001*	<.0001*
82.8	20.7	<.0001*	<.0001*
124.2	20.7	<.0001*	<.0001*
165.6	20.7	<.0001*	<.0001*
62.1	41.4	0.4510	<.0001*
82.8	41.4	<.0001*	<.0001*
124.2	41.4	<.0001*	<.0001*
165.6	41.4	<.0001*	<.0001*
82.8	62.1	0.0003*	0.0001*
124.2	62.1	<.0001*	<.0001*
165.6	62.1	<.0001*	<.0001*
124.2	82.8	<.0001*	0.5568
165.6	82.8	<.0001*	0.1394
165.6	124.2	0.7532	0.0081*

Figure 65: XTT results of mixed cultures irradiated with 10.35, 20.70, 41.40, 62.10, 82.80, 124.20 and 165.60 J/cm² of blue light using MEDILIGHT prototypes. Assay was performed 24 h after the irradiation. Prototype set-up included back reflector, silicon encapsulation and wound dressing E2723. As a reference experiments with the Philips lamp were done in parallel. Data are shown as means ± SD. Each value represents n=3 plates with 3 repetitions.

As the efficacy of the prototype was proven, animal studies were conducted using the MEDILIGHT prototype.

3.2.4 Long-term irradiation of diabetic and non-diabetic rats with MEDILIGHT prototype

While the rats were receiving the high-caloric diet, their blood glucose concentration was monitored every two weeks (Figure 66).

It was noted that the glucose concentration for ZDF fa/fa rats is increasing over time from around 150 mg/dL to 500 mg/dL. These rising glucose levels were accompanied by polyuria and polydipsia; therefore development of diabetes could be confirmed in these animals.
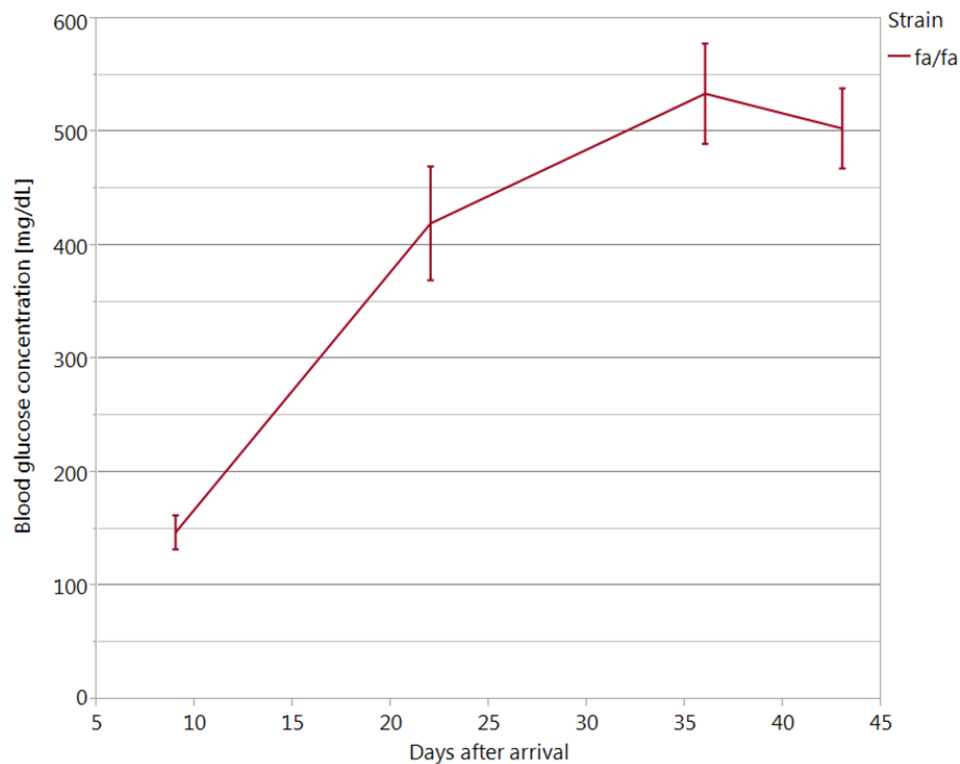
Figure 66: Blood glucose concentration of ZDF fa/fa rats to be irradiated with the MEDILIGHT prototype. The measurements started shortly after the arrival of the animals until the end of the experiment. Values are shown as means ± SD.

During the experiment images of the wounds were taken every second day. To calculate the exact wound sizes in mm² from the pixels in the digital images, an open source image processing package based on ImageJ was used (Fiji). Wound areas were associated with the wound size on the first day to calculate the wound healing in %. Wound areas were compared between the irradiated and control rats, displayed in Figure 67.

In the graph the wound sizes between irradiated and control animals do not show any significant differences, wound sizes on day 3 and day 7 seem to be even slightly, but not significantly, bigger for irradiated rats. The wound sizes at the end of the experiment are equal in size though, therefore blue light treatment does not impair wound healing.

Also, no differences between non-irradiated wounds of irradiated animals and the control wounds of non-irradiated animals could be seen, therefore the data is not shown.
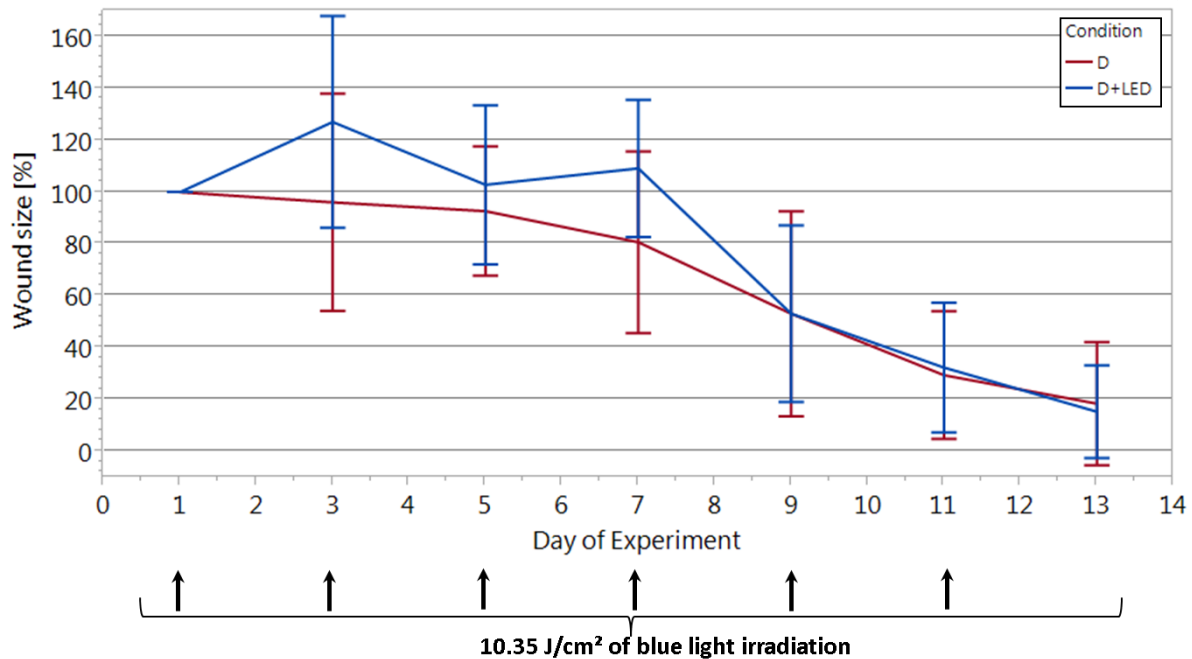
Figure 67: Wound areas displayed in % normalized to the wound area on day 1 (D = Diabetic ZDF fa/fa, LED = Light therapy). Rats were irradiated with 10.35 J/cm² of blue light on day 1, 3, 5, 7, 9, and 11, which is marked by the arrows below the graph. Both groups of animals consist of n=6 animals, data are displayed in means ± SD.

From blood sampling on day 1 and day 13 plasma samples were tested for the concentration of different parameters (Table 23).

Significant differences can be seen for ALT, where the values are significantly decreased after the experiment for control rats by 44% (p < <0.05) and for irradiated rats by 71% (p < 0.001). There is also a significant difference concerning ALT values when irradiated and control rats are compared after the experiment. The difference accounts to a significant decrease by 48% (p < 0.05) for irradiated rats. There is also a reduction in AST concentration in the plasma for both groups after the end of the experiments. This is only significant for irradiated rats, where the decrease amounts to 34% (p < 0.05). Also for GLDH the values are significantly reduced for both groups after the end of the experiment. For control rats the concentration is significantly reduced by 76% (p < 0.01) and for irradiated rats by 84% (p < 0.01). The same effect is observed for potassium values, where for control rats the reduction amounts to 7% (p < 0.05) and for irradiated rats to 8% (p < 0.01). Protein concentration is slightly increased for irradiated rats by 5% (p < 0.05) and sodium levels for both groups by approximately 30% (p < 0.05 and p < 0.001). Development of urea concentration follows the same pattern with a significant reduction of 19% (p < 0.001) for control rats and of 13% (p < 0.01) for irradiated rats.

Table 23: Concentration of different plasma parameters of diabetic control and irradiated rats (ZDF fa/fa) are listed. Samples were taken on day 1 and day 13 of the experiment from n=6 animals per group and time point. Samples before the start of the experiment were pooled for a baseline. Data are expressed as means ± SD. Values significantly different from the baseline are indicated as *p < 0.05, **p < 0.01, ***p <0.001. Significances are referred to the respective baseline; parameters were also compared between the two groups, significant values indicated by *p < 0.05, **p < 0.01, ***p <0.001.

Plasma parameter	Time point [days]	ZDF fa/fa rats Control	ZDF fa/fa rats Irradiated
ALT [U/L]	1	177 ± 94	177 ± 94
	13	99 ± 42*	52 ± 26*****
AST [U/L]	1	121 ± 83	121 ± 83
	13	84 ± 29	80 ± 43*
Calcium [mmol/L]	1	2.79 ± 0.10	2.79 ± 0.10
	13	2.84 ± 0.06	2.86 ± 0.03
Cholesterol [mg/dL]	1	141 ± 15	141 ± 15
	13	133 ± 13	133 ± 9
Creatinine [mg/mL]	1	0.21 ± 0.02	0.21 ± 0.02
	13	0.22 ± 0.01	0.22 ± 0.02
GLDH [U/L]	1	108.6 ± 102.8	108.6 ± 102.8
	13	26.0 ± 24.6**	16.8 ± 19.8**
Phosphate [mmol/L]	1	2.14 ± 0.11	2.14 ± 0.11
	13	2.13 ± 0.16	2.11 ± 0.10
Potassium [mmol/L]	1	5.09 ± 0.39	5.09 ± 0.39
	13	4.72 ± 0.25*	4.67 ± 0.18**
Protein [mg/mL]	1	65 ± 3	65 ± 3
	13	67 ± 2	68 ± 1*
Sodium [mmol/L]	1	133 ± 3	133 ± 3
	13	136 ± 3*	138 ± 1***
Triglycerides [mg/dL]	1	465 ± 102	465 ± 102
	13	311 ± 51***	309 ± 136**
Urea [mg/dL]	1	53.9 ± 5.3	53.9 ± 5.3
	13	43.6 ± 3.6***	47.1 ± 4.5**

Furthermore, the rat specific CRP concentration was tested (Figure 68).
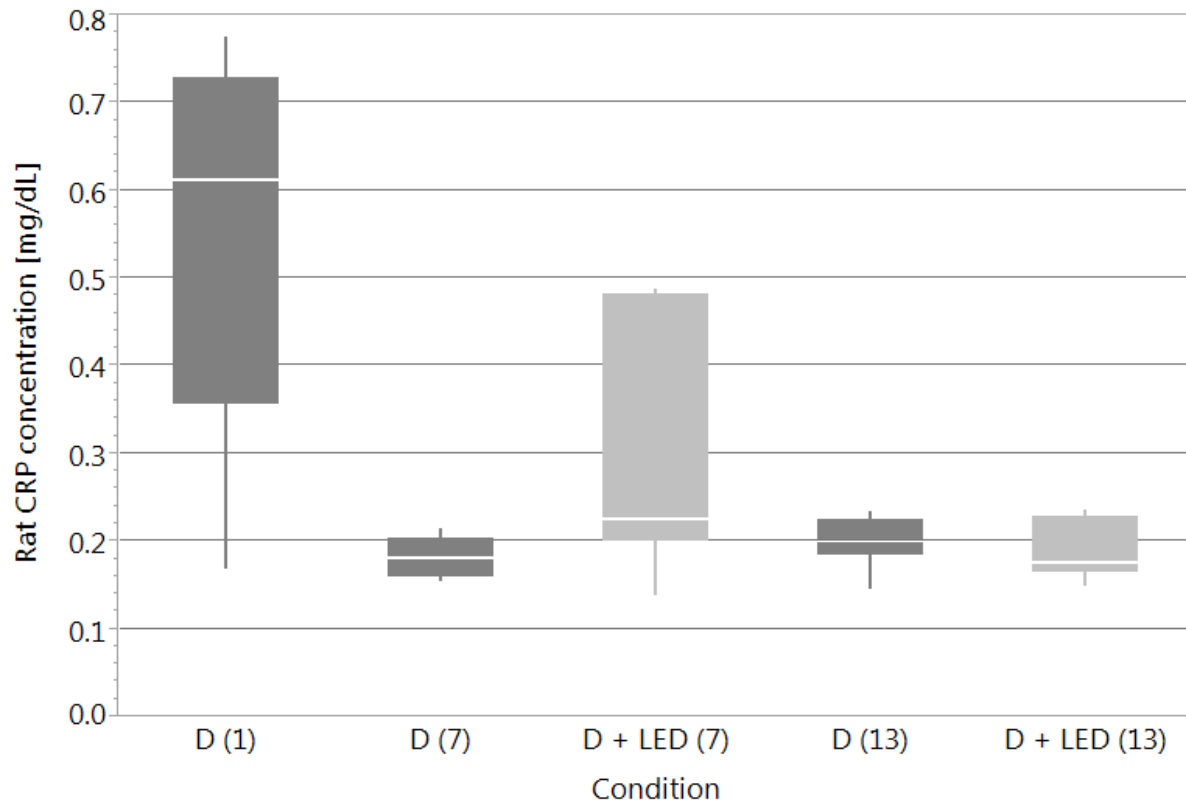
Figure 68: CRP concentration in rat plasma determined by ELISA of control (D) and light treated groups of diabetic rats (D+LED) in a long-term experiment. Samples were taken on day 1, 7 and 13. Data are shown as box plots with the median, upper and lower quartile (interquartile range (IQR)) and whiskers (1.5 x IQR). Each box plot represents n=6 plasma samples.

The results show that on day 1 of the experiment the CRP concentration is quite high at 0.6 mg/dL. If we compare the CRP concentrations on day 7 of the experiment, differences between the groups are showing: for the group receiving light therapy the CRP concentration is around 0.04 mg/dL higher than for the control group ($p < 0.0661$). The differences compared to day 1 are significant for both groups with $p < 0.001$. After the experiment is finished on day 13, CRP is lower compared to day 1 at a level of 0.2 mg/dL ($p < 0.001$), but nearly the same for both groups.

 As no differences between irradiated and control animals could be seen at the end of the experiment, no further analysis was performed.

4 DISCUSSION

4.1 Effects of blue light irradiation on *in vitro* skin models

First, different *in vitro* models of skin, consisting of keratinocytes and fibroblasts, were tested in this study. The co-culture model resulted in unstable, but mostly significant results; however, high standard deviations were a problem. The procedure, where the cells were separated from the cell culture insert, was stressing the cells, leading to inaccurate results. To solve this problem, another skin model was tested. Instead of cultivating the cells and separating them by treatment with trypsin, they were incubated together as a mixed culture. This showed results that were more stable and more consistent with experiments performed on mono-cultures of the respective cells.

With the fluences tested that were obtained from mono-cultures, a biphasic dose response curve could also be confirmed for mixed cultures. Here, irradiation with 10.35 J/cm² of blue light led to an increase of metabolic activity and a decrease with 41.40 J/cm². Higher doses were aimed to be used in a wound healing scenario to first hinder keratinocytes to close a wound prematurely, before fibroblasts could heal the wound from beneath. Secondly, lower doses were employed to enhance wound healing and trigger fibroblasts to proliferate faster and migrate faster to the wound site and thereby closing it.

Results on metabolic activity obtained by XTT test were confirmed with the scratch wound healing assay. The scratch assay proved that blue light treatment does not only have an impact on the metabolic activity, but also influences cells to proliferate and migrate differently, in respect to the fluences used.

After treatment with 10.35 J/cm² of blue light, keratinocytes and mixed cultures showed an increase in proliferation by closing the artificial wound faster than the control cells. In contrast to that, fibroblasts did not show this effect, but revealed a reduced proliferation following low dose blue light treatment. This result does not necessary mean that low doses of blue light enhance metabolic activity while reducing the proliferation in fibroblasts: differences between set-ups of XTT and scratch assay could be the cause of that. While for the XTT assay black 96-well plates were used, this was not possible for scratch assays. Bigger wells were needed in this experiment, but unfortunately, no black plates are available in the size of

12-well plates. This causes a change of irradiance for the scratch assay, compared to the XTT assay. When cells are irradiated in black 96-well plates, some of the light is absorbed by the black walls of the plates. This ensures that there is no cross-talk between the wells and at the same time reduces the irradiance received by the cells. By switching to transparent 12-well plates, no light is absorbed, leading to a higher irradiance, enhanced by refraction in between the wells, allowing cross-talk [89]. While this is also true for the other set-ups without changing the outcome, it is possible that fibroblasts are more susceptible to these changes. Fibroblasts are known to be more sensitive, compared to keratinocytes [90, 91]. They might therefore have a narrower therapeutic window concerning phototherapy while keratinocytes have a broader therapeutic window. When cultivated as a mixed culture, keratinocytes might level out the byproducts of fibroblasts (ROS) therefore leading to an increase in proliferation nonetheless [92].

Treatment with 41.40 J/cm² showed the opposite effect on keratinocytes, fibroblasts and mixed cultures consisting thereof: XTT assays revealed a reduction in metabolic activity for all cell cultures as well as anti-proliferative effects, tested by the scratch assay. Differences could be observed concerning migration. While fibroblasts also migrated to the wound site, keratinocytes and mixed cultures did not express this behavior. Keratinocytes and mixed cultures seem to close the artificial wound primarily by proliferation rather than migration. This can be observed when in fibroblast cultures cells appear randomly in the middle, while for e.g. keratinocytes the cell fronts move towards each other as a whole [93-96].

4.2 Effects of single doses of blue light with various fluences on rats

Because *in vitro* studies revealed the desired results, the experiments were transferred to *in vivo* models, to test the efficacy of blue light and whether any side effects were occurring. For that, the ZDF fa/+ rat was chosen as a suitable model. This is the healthy, lean heterozygous form of rats, where the homozygous animals can be triggered by their feed to develop diabetes type 2 with all its side effects, including impaired wound healing. Single doses of blue light irradiation with different fluences were tested on the healthy ZDF fa/+ rats. Additionally to the fluences identified to change metabolic activity, migration and proliferation, an even higher dose of blue light with 82.80 J/cm² was included in the testing. This fluence of blue

light revealed an anti-bacterial effect, as tested by members of our group and is also confirmed by various studies [97-99].

First, blood glucose measurements were performed to be able to later compare them to the blood glucose levels of diabetic animals. Here, the concentrations were in a normal range with 137 mg/dL (± 10). Then, plasma samples were extracted before and after treatment, to compare whether there is an effect on the parameters of full overview plasma profiles for liver and kidney function.

Differences were observed for AST, which is an indicator for liver damage. AST was significantly increased for all groups post-treatment including control animals. This is very likely a side effect of the anesthetics used in the experiment (ketamine) which are known to lead to liver damage [100, 101].

Also, cholesterol levels differ for all groups after treatment including control animals, which is decreased by approximately 10%. Again, the anesthetic ketamine is likely the reason for this decrease as it alters the lipid metabolism, having an effect on LDL formation [102, 103].

A slight but significant decrease in protein levels for control rats was observed, while irradiated rats did not. Low protein concentrations are not only a possible indicator for protein malnutrition, but are also signs of inflammation and chronic disease [104, 105]. Here, the inflammation is a result of the experimental procedure, where wounds are inflicted on the rats. While control rats show signs of this inflammation it is possible that blue light prevents or reduces inflammatory processes, independently from the dose.

CRP concentration in plasma was determined by a rat specific ELISA. Results showed an increase of CRP concentration after wounding of control rats. CRP is an acute phase protein, which can be used to identify infections or inflammation early on [106]. This of course results from the injury applied by the biopsy punches and is a normal process of wound healing. Also, rats irradiated with 82.80 J/cm² and 41.40 J/cm² of blue light showed an increase in CRP after the treatment, meaning that there is no difference between irradiated and control groups. In contrast to that, animals irradiated with 10.35 J/cm² stand out: with lower concentration of CRP compared to post-experiment values, comparable to values determined before the

start of the experiment. CRP is an unspecific inflammatory parameter and is increased when an inflammation persist in an organism[106]. Reduction or a missing increase for the group irradiated with 10.35 J/cm² indicates a suppression of inflammatory processes.

As the wounds were observed for only three days, a comparison between the wound sizes did not seem to be appropriate to be analysed. Therefore histological slides were imaged and different parameters compared. First the size of the inflammatory sites was determined. Results showed no significant differences due to a small sample size, but some trends could be determined. While wounds irradiated with 82.80 J/cm² of blue light showed no difference to the control, an increase of the inflammatory site after irradiation with 10.35 J/cm² could be seen. In contrast to that, after irradiation with 41.40 J/cm² a decrease of the inflammatory site was observed, compared to the control. Concluding from that and CRP results it can be assumed, that irradiation with low fluences reduces the overall inflammation, but drives the wound healing process forward.

Analysis of histology showed a decreased inflammatory site of skin tissue irradiated with 41.40 J/cm². Number of leukocytes per area was found to be decreased for 82.80 J/cm².

Gene expression analysis showed linear correlation by increasing number of pathways up-regulated of 'Genetic Information Processing' with increasing fluences. Most pathways of cellular processes were up-regulated for 10.35 J/cm² and 41.40 J/cm². Many pathways of the categories 'Metabolism', 'Organismal Systems' and 'Human Diseases' were down-regulated for 41.40 J/cm² and 82.80 J/cm².

For 10.35 J/cm² DNA replication is up-regulated, which increases cell division, causing the metabolic activity and cell proliferation to be increased, as seen *in vitro*. This does not comprise cell survival, as the cell cycle is up-regulated and pathways related to apoptosis are not affected. Some repair mechanisms are up-regulated, which may be caused by cellular stress. Blue light is known to increase ROS production[107-109] which might be the trigger here.

Therefore p53 signaling pathway up-regulation is no surprise. It also reacts to oxidative stress causing cell cycle arrest, cellular senescence or apoptosis. AMPK signaling pathway was down-regulated. AMPK is a sensor of cellular energy status. It is activated when metabolic stresses are present and influence ATP production or consumption. As this pathway is down-regulated, activation of energy-consuming biosynthetic pathways takes place. In our case, only glycan biosynthesis is up-regulated. Phagosome pathways are also up-regulated, which play a role in tissue remodeling and inflammation. The same holds for leukocyte transendothelial migration and toll-like receptor signaling pathways, which were also found to be up-regulated.

The combination of the affected pathways suggests that the immune response is enhanced artificially by the blue light. ROS production is increased, which stresses the cells, causing them to enhance repair mechanisms and inflammatory pathways. The actual damage appears "bigger than it is" or more harmful/serious to the organism; in turn, this leads to an increased metabolic activity and proliferation to heal the injury as fast as possible. This can especially be confirmed by pathways from the main category 'Human Diseases', where bacterial invasion of epithelial cells and systemic lupus erythematosus are up-regulated.

Metabolic pathways were mostly down-regulated for 41.40 J/cm², which could be a reason for the effects seen *in vitro* with this fluence, where proliferation and metabolic activity is decreased. 82.80 J/cm² of blue light do not seem to cause as many down-regulated pathways. For both of the fluences repair mechanisms are up-regulated as well as DNA replication. 'Genetic Information Processing' pathways were mostly found to be up-regulated. Protein production seems to be enhanced, as pathways of ribosomes, RNA transport, mRNA surveillance and protein processing are up-regulated.

Further MAPK signaling pathway is down-regulated, which are important for cell proliferation and migration. This might explain the effects seen *in vitro*, where metabolic activity and proliferation is down-regulated. In that sense also cAMP is down-regulated, which has an influence on metabolism and gene transcription.

For higher fluences the cell cycle is up-regulated, which can occur in response to cellular stress to promote cell cycle arrest and enhance DNA repair. This pathway also activates p53 which is also found to be up-regulated.

Inflammatory pathways are also up-regulated, for instance, Phagosome pathways, which also play a central role in tissue remodeling. In contrast to that peroxisome pathways are down-regulated, which affect redox signaling and lipid homeostasis. Reason for this might be the presence of ROS. The same as for lower fluences, the leukocyte transendothelial migration is up-regulated, increasing inflammatory responses and should improve wound healing.

Cell adhesion molecules (CAMs) are up-regulated for all fluences. They play a critical role in hemostasis, immune response, inflammation, brain morphology, memory and learning, suggesting an enhanced brain function with blue light irradiation.

Pathways linked to Alzheimer and Parkinson disease are down-regulated for all fluences, suggesting an improvement with blue light treatment. Both of these diseases show functional impairment of the brain accompanied by daytime sleepiness and fatigue [55, 57]. Studies proved that blue light irradiation can have a positive effect on sleep quality and cognitive functions in Alzheimer's and Parkinson's patients [51, 54, 56]. Other studies included patients with traumatic brain injury, where recovery could be improved with blue light [51, 52].

4.3   Long-term irradiation of diabetic rats

To start long-term irradiation of these rats, the diabetic wound model was first established. Induction of type 2 diabetes was confirmed by steadily increased glucose levels, accompanied by polyuria and polydipsia. The inflicted wounds were observed over 13 days. Results showed that wounds irradiated with the light schedule over this time course started to heal faster with 10.35 J/cm² of blue light from day 6 onwards. The outcome was an earlier closure of 3 days compared to non-irradiated wounds.

Compared to that, wounds of non-diabetic rats irradiated with blue light closed faster. The difference could be observed already on day 2 of the experiment and was noticeable until day 8. Then blue light had a better effect on diabetic rats, so that the wounds were similar in size for the remaining 5 days.

Further, plasma samples were analyzed, revealing changes due to the induction of diabetes. Cholesterol levels and triglyceride concentrations were increased for diabetic rats. As the blood is saturated with glucose, and cannot be stored as glycogen due to the lack of insulin, fatty acids are formed. Plasma calcium levels

were increased for diabetic rats as well. Increased calcium levels are associated with impaired glucose metabolism, which can be seen in blood glucose concentrations and, of course, was one of the aims here. Decreased plasma creatinine concentration is associated with an increased risk of type 2 diabetes [110], which was the case as seen in the data. Sodium concentration of diabetic rats was found to be decreased compared to the non-diabetic rats. Hyponatremia is associated with high fluid-intake (polydipsia). As this is one of the symptoms of type 2 diabetes it is expected for the diabetic rats. Due to the metabolic changes in diabetic rats, also the inorganic phosphate is increased. As diabetes is not treated, high energy phosphates are reduced and tissue becomes hypoxic.

ELISA for rat specific CRP showed a high concentration for diabetic rats on the day of wound infliction. At the end of the experiment CRP is on similar levels between control and irradiated rats, while irradiated rats show slightly higher values. Differences might be small, but show that inflammation persisted longer in irradiated rats.

Compared to that, non-diabetic animals had a quite low CRP concentration on day 1 compared to diabetic rats. This concentration was slightly decreased on day 13 as the wounds were nearly healed and the inflammation nearly diminished.

The difference between the two set-ups (diabetic/non-diabetic) also suggests that small injuries are more severe for diabetic rats and pose a higher risk to the organism due to the high immune response.

Histologic analysis of epidermal thickness showed that while irradiated wounds were closed faster, the epidermis was quite thin, compared to the non-irradiated counterparts. Non-diabetic irradiated wounds did also close faster, but epidermal thickness was the same as for diabetic animals not treated with light. This means that while blue light irradiation enhances wound healing, it comes with repercussions of thinner skin at the injury site.

Percentage of leukocytes at the inflammatory site showed that diabetic animals have a higher count than non-diabetic animals. This is a side effect of the metabolic disease, where base levels differ between healthy and sick animals. The same trend can be seen for the number of leukocytes on the inflammatory site, where for diabetic animals the number is increased, compared to healthy controls.

Conspicuously TNF and NF-κB pathways are up-regulated. These pro-inflammatory pathways are usually found to be down-regulated as PBM is often used to improve inflammatory conditions [111, 112]. On the other hand, an increase in inflammatory processes might drive wound healing forward, seen in the up-regulation of autophagy, lysosome and phagosome pathways. Acceleration of these pathways can help cleansing the injured tissue faster, by removing cell debris and pathogens. Up-regulated toll-like receptors that can recognize pathogen-associated molecular patterns can contribute to that, as well as up-regulated NOD-like receptor signaling pathway. Also MAPK adds to that, causing cell proliferation, differentiation and migration. Cytokine interaction and receptors were found to be up-regulated, which also enhances cell growth and repair processes, while restoring homeostasis.

While cell cycle seems to be down-regulated after light treatment and apoptosis, necroptosis and ferroptosis are up-regulated, it could be assumed that cell death is taking place increasingly and cells proliferate slower. Studies found though, through FACS analysis of skin cells, that this was not the case [108] and the results show faster wound healing using light treatment. As ROS is produced during PBM application [107-109] these pathways are up-regulated, but to lead to actual cell death, a certain threshold has to be reached, which is not the case here.

Additionally, as in short-term irradiation of rats shows, certain cellular repair mechanisms are up-regulated, which may be already diminished at the end of the long-term irradiation and therefore cannot be found in the gene expression analysis.

The nervous system seemed to be affected by blue light treatment as well. The neurotrophin signaling pathway was found to be up-regulated, which can enhance growth and survival of neural cells and therefore adding to restoring injuries [52, 53].

A study suggests that PBM reduces abdominal adipose tissue inflammatory infiltrate, PBM could reduce inflammatory areas and significantly lower blood glucose levels [113]. Another study suggests improvement of glucose metabolism and intracellular insulin pathway, parameters related to obesity, glucose tolerance and reduced the area of epididymal and mesenteric adipocytes [39].

Fatty acid metabolism and other pathways linked to lipid metabolism were found to be down-regulated, while lipolysis and adipocytokine signaling pathways are up-

regulated. Metabolism of carbohydrates as glycolysis and gluconeogenesis pathways, as well as starch and sucrose metabolism were found to be up-regulated.

4.4 Development of a prototype for use in diabetic patients

In the scope of the MEDILIGHT project, a device was developed, which was intended for use on diabetic patients with chronic wounds. Several optimization steps had to be taken.

First, the efficacy of the device was proven by comparing it to the Philips BioLight, which was used throughout previous experiments. Due to experiments performed with different components, it was decided to use a diffusor, to create a homogenous field of irradiation. In a further step, a wound dressing was compared to the results with the diffusor. The wound dressing was also able to create a homogenous irradiation field, but decreased effects of the blue light due to decreased irradiance. Irradiation times had to be adjusted, so that fluences were increased and irradiation showed the desired outcomes in cell culture.

As irradiation times were increased to compensate for the reduction of irradiance, temperature of the device and on the irradiated surface increased. As this could pose a risk of burns, temperature measurements were performed on skin polymer models. Without optimization maximum temperatures of 52°C were reached.

A strategy to reduce heat build-up, irradiation cycles of 1 min were introduced. Breaks of 1 min in between the irradiations could already reduce the maximum temperature to 40°C.

Secondly, another improvement was added. The device was programmed in such a way that it could measure the temperature with a sensor located on the flexible foil in between the LEDs and shut off and on automatically at pre-programmed temperatures. The range was chosen to be between 37°C and 40°C.

With this safety precautions, animal experiments on porcine skin could be performed. Measurements without the wound dressing revealed a maximum temperature of 37°C after irradiation over 1 h. This served as an alternative, in case irradiation with the wound dressing would lead to high temperatures. As this was confirmed to be safe, experiments with the wound dressing were performed.

Experiments with the wound dressing lead to stable results, where an alternation of on- and off-cycles of 8 s and 13 s was identified. Visual comparison of the porcine

skin showed no differences before and after irradiation, proving the safety of the device, as no initial burns were observed.

In further steps, the maximum temperature was increased, leading to the identification of acceptable cycles for *in vitro* testing with 30 s on- and off-time, respectively.

Final examination of histological skin samples from the irradiated areas revealed no changes in the physiology of the skin, again, proving the safety of the device.

The final set-up of the device with all of its components had to be tested again *in vitro*. XTT results showed a shift of the biphasic dose-response-curve to longer irradiation times/higher fluences. By application of the prototype for 20.70 J/cm² the proliferative effect of blue light could be enhanced in contrast to the Philips BioLight. Similarly, the full effect of the anti-proliferative phase was reached at 82.80 J/cm² with the prototype instead of the initial 41.40 J/cm² with the Philips BioLight.

Finally, the device had to be tested also *in vivo*. In these experiments, only the proliferative effects were analyzed, therefore irradiation with 10.35 J/cm² took place only. Unfortunately, results did not show the desired effects and wound sizes did not change significantly for the irradiated group. Reason for this could be the small therapeutic window of PBM treatment. Effects of PBM can differ significantly, when small details are changed. For instance, precise irradiances with certain irradiation times have to be chosen to reach desired effects. The fluence is not the only criterion that is important, so it would not necessarily lead to the same outcome if lower irradiances are chosen and compensated for by longer irradiation times (resulting in the same fluence). This could have happened when new components were introduced: the overall fluence was the same, but irradiance was lower and irradiation time was increased. To be certain of this outcome, another experiment should be conducted, where the device is tested with the initial settings that were used in previous *in vivo* experiments.

4.5   Conclusion and outlook

Proliferative and anti-proliferative effects could be found for skin cells, using different fluences of blue light. While metabolic activity was increased, proliferation was decreased for fibroblasts tested by the scratch assay when irradiated with

10.35 J/cm² which is contradictory to each other. It is possible that by the different set-up with transparent instead of black plates, the fluence was increased, leading to an anti-proliferative effect. This should be investigated in more detail, where shorter irradiation times are applied.

It could be successfully proven, that also in combination of both cell types, blue light irradiation could trigger the desired effects. For mixed cultures it could be further investigated, if and how the migration behavior of the cells is changing with the application of blue light. This could be achieved by staining keratinocytes and fibroblasts with two different dyes and observing their migration microscopically.

The experiments could also be transferred to *in vivo* studies, where effects could be seen in the gene expression. Here, 10.35 J/cm² of blue light increases inflammation and repair mechanisms locally, therefore overall inflammation is decreased, seen by decreased CRP values. This led to a faster wound closure in the long-term study. Higher fluences triggered similar pathways, but did not show a delay in wound healing. This can be used in a clinical application, when chronic wounds should receive an anti-bacterial treatment, but not affecting the wound healing.

For this a light schedule was created in this study and the corresponding device was developed. The efficacy and safety of the device was proven, but due to changes in the set-up during irradiation, the animal model did not lead to positive results. The set-up has to be optimized in that aspect and *in vivo* experiments should be repeated in that aspect.

5 SUMMARY

In this project a therapy and a device to treat chronic wounds in diabetics were developed. The therapy is based on photobiomodulation using blue light. The effects of different doses of blue light were first tested *in vitro* on skin models of keratinocytes and fibroblasts in different models. Here, an enhanced metabolic activity and proliferation could be identified with 10.35 J/cm². With higher fluences (41.40 and 82.80 J/cm²) the opposite effect could be observed: decreased metabolic activity and proliferation were revealed. Further, the experiments were transferred to *in vivo* testing on rats. Also here, single blue light irradiations with different doses revealed different effects in dependence of the dose, as is typical for photobiomodulation, described as the Arndt-Schulz-curve. Effects could be seen regarding the CRP, showing a reduction of inflammation with lower fluences. Gene expression revealed changes in the inflammatory response, where certain anti-inflammatory and pro-inflammatory pathways were deregulated. The inflammatory response seemed to be enhanced, driving forward the overall inflammation response. This could be confirmed by long-term irradiation of diabetic rats, where wounds treated with light therapy healed faster than non-treated wounds. Inflammatory pathways were deregulated, proliferation and differentiation was up-regulated, formation of fibers and neurons and remodeling of granulation tissue was enhanced.

To be able to apply the findings on patients, a device was developed, which emits blue light. This device was tested *in vitro* first, where single irradiations showed the same effects as with the lamp used for preliminary experiments. To prevent heat development the device was programmed to use pulses instead of continuous irradiation. Thereby the heat development could be reduced from a maximum temperature of 52°C to 37°C with pulses of 30 s. This scheme was tested on porcine skin, where no negative effects could be seen. The light schedule was tested again *in vitro*, showing a shift to higher fluences to achieve the desired effects. *In vivo* testing unfortunately did not lead to positive results, probably due to involvement of a wound dressing, changing the homogeneity of the irradiation area.

Nevertheless, the project led to interesting outcomes, which are ready to be applied in a clinical trial and could improve healing of chronic wounds.

6 REFERENCES

1. Gould, J: Superpowered skin. *Nature,* 563**:** 84-85, 2018.
2. Alberts, B, Johnson, A, Lewis, J, Raff, M, Roberts, K, Walter, P: *Molecular Biology of the Cell*, Garland Science, 2002.
3. Wikramanayake, TC, Stojadinovic, O, Tomic-Canic, M: Epidermal differentiation in barrier maintenance and wound healing. *Adv Wound Care,* 3**:** 272-280, 2014.
4. Wickett, RR, Visscher, MO: Structure and function of the epidermal barrier. *Am J Infect Control,* 34**:** S98-S110, 2006.
5. Shier, D, Butler, J, Lewis, R: *Hole's Human Anatomy and Physiology*, McGraw Hill Education, 1999.
6. MacNeil, S: Progress and opportunities for tissue-engineered skin. *Nature,* 445**:** 874, 2007.
7. Facy, V, Flouret, V, Regnier, M, Schmidt, R: Reactivity of Langerhans cells in human reconstructed epidermis to known allergens and UV radiation. *Toxicol In Vitro,* 19**:** 787-795, 2005.
8. Fratzl, P: *Collagen: structure and mechanics, an introduction*, Springer, 2008.
9. Lindley, LE, Stojadinovic, O, Pastar, I, Tomic-Canic, M: Biology and biomarkers for wound healing. *Plast Reconstr Surg,* 138**:** 18S, 2016.
10. Martin, P: Wound healing - aiming for perfect skin regeneration. *Science,* 276**:** 75-81, 1997.
11. Singer, AJ, Clark, RA: Cutaneous wound healing. *N Engl J Med,* 341**:** 738-746, 1999.
12. Berman, B, Maderal, A, Raphael, B: Keloids and hypertrophic scars: pathophysiology, classification, and treatment. *Dermatol Surg,* 43**:** S3-S18, 2017.
13. Eming, SA, Martin, P, Tomic-Canic, M: Wound repair and regeneration: mechanisms, signaling, and translation. *Sci Transl Med,* 6**:** 265-266, 2014.
14. Su, W-H, Cheng, M-H, Lee, W-L, Tsou, T-S, Chang, W-H, Chen, C-S, Wang, P-H: Nonsteroidal anti-inflammatory drugs for wounds: pain relief or excessive scar formation? *Mediators Inflamm***:** doi: 10.1155/2010/413238, 2010.
15. Plikus, MV, Guerrero-Juarez, CF, Ito, M, Li, YR, Dedhia, PH, Zheng, Y, Shao, M, Gay, DL, Ramos, R, Hsi, T-C: Regeneration of fat cells from myofibroblasts during wound healing. *Science,* 355**:** 748-752, 2017.
16. Tsai, H-W, Wang, P-H, Tsui, K-H: Mesenchymal stem cell in wound healing and regeneration. LWW, 2018.
17. Lazarus, GS, Cooper, DM, Knighton, DR, Margolis, DJ, Pecoraro, RE, Rodeheaver, G, Robson, MC: Definitions and guidelines for assessment of wounds and evaluation of healing. *Arch Dermatol,* 130**:** 489-493, 1994.
18. Christman, AL, Selvin, E, Margolis, DJ, Lazarus, GS, Garza, LA: Hemoglobin A1c predicts healing rate in diabetic wounds. *J Invest Dermatol,* 131**:** 2121-2127, 2011.
19. Sargen, MR, Hoffstad, O, Margolis, DJ: Geographic variation in Medicare spending and mortality for diabetic patients with foot ulcers and amputations. *J Diabetes Complications,* 27**:** 128-133, 2013.
20. Beidler, SK, Douillet, CD, Berndt, DF, Keagy, BA, Rich, PB, Marston, WA: Inflammatory cytokine levels in chronic venous insufficiency ulcer tissue before and after compression therapy. *J Vasc Surg,* 49**:** 1013-1020, 2009.

21. Sindrilaru, A, Peters, T, Wieschalka, S, Baican, C, Baican, A, Peter, H, Hainzl, A, Schatz, S, Qi, Y, Schlecht, A, Weiss, JM, Wlaschek, M, Sunderkotter, C, Scharffetter-Kochanek, K: An unrestrained proinflammatory M1 macrophage population induced by iron impairs wound healing in humans and mice. *J Clin Invest,* 121**:** 985-997, 2011.

22. Loots, MA, Lamme, EN, Zeegelaar, J, Mekkes, JR, Bos, JD, Middelkoop, E: Differences in cellular infiltrate and extracellular matrix of chronic diabetic and venous ulcers versus acute wounds. *J Invest Dermatol,* 111**:** 850-857, 1998.

23. Tarnuzzer, RW, Schultz, GS: Biochemical analysis of acute and chronic wound environments. *Wound Repair Regen,* 4**:** 321-325, 1996.

24. Cohen, BE, Geronemus, RG, McDaniel, DH, Brauer, JA: The role of elastic fibers in scar formation and treatment. *Dermatol Surg,* 43**:** S19-S24, 2017.

25. Wang, PH, Huang, BS, Horng, HC, Yeh, CC, Chen, YJ: Wound healing. *J Chin Med Assoc,* 81**:** 94-101, 2018.

26. Lewis, CE, McTigue, KM, Burke, LE, Poirier, P, Eckel, RH, Howard, BV, Allison, DB, Kumanyika, S, Pi-Sunyer, FX: Mortality, health outcomes, and body mass index in the overweight range: a science advisory from the American Heart Association. *Circulation,* 119**:** 3263-3271, 2009.

27. Han, G, Ceilley, R: Chronic Wound Healing: A Review of Current Management and Treatments. *Adv Ther,* 34**:** 599-610, 2017.

28. Barrientos, S, Brem, H, Stojadinovic, O, Tomic-Canic, M: Clinical application of growth factors and cytokines in wound healing. *Wound Repair Regen,* 22**:** 569-578, 2014.

29. Da Costa, RM, Ribeiro Jesus, FM, Aniceto, C, Mendes, M: Randomized, double-blind, placebo-controlled, dose- ranging study of granulocyte-macrophage colony stimulating factor in patients with chronic venous leg ulcers. *Wound Repair Regen,* 7**:** 17-25, 1999.

30. Smiell, JM, Wieman, TJ, Steed, DL, Perry, BH, Sampson, AR, Schwab, BH: Efficacy and safety of becaplermin (recombinant human platelet-derived growth factor-BB) in patients with nonhealing, lower extremity diabetic ulcers: a combined analysis of four randomized studies. *Wound Repair Regen,* 7**:** 335-346, 1999.

31. Rheinwald, JG, Green, H: Serial cultivation of strains of human epidermal keratinocytes: the formation of keratinizing colonies from single cells. *Cell,* 6**:** 331-343, 1975.

32. Rennert, RC, Rodrigues, M, Wong, VW, Duscher, D, Hu, M, Maan, Z, Sorkin, M, Gurtner, GC, Longaker, MT: Biological therapies for the treatment of cutaneous wounds: phase III and launched therapies. *Expert Opin Biol Ther,* 13**:** 1523-1541, 2013.

33. Streubel, PN, Stinner, DJ, Obremskey, WT: Use of negative-pressure wound therapy in orthopaedic trauma. *J Am Acad Orthop Surg,* 20**:** 564-574, 2012.

34. Kim, GH, Paik, SS, Park, YS, Kim, HG, Kim, IB: Amelioration of Mouse Retinal Degeneration After Blue LED Exposure by Glycyrrhizic Acid-Mediated Inhibition of Inflammation. *Front Cell Neurosci,* 13**:** 319, 2019.

35. Pires, D, Xavier, M, Araujo, T, Silva, JA, Jr., Aimbire, F, Albertini, R: Low-level laser therapy (LLLT; 780 nm) acts differently on mRNA expression of anti- and pro-inflammatory mediators in an experimental model of collagenase-induced tendinitis in rat. *Lasers Med Sci,* 26**:** 85-94, 2011.

36. Hwang, MH, Shin, JH, Kim, KS, Yoo, CM, Jo, GE, Kim, JH, Choi, H: Low level light therapy modulates inflammatory mediators secreted by human annulus

fibrosus cells during intervertebral disc degeneration in vitro. *Photochem Photobiol,* 91**:** 403-410, 2015.

37. Alves, AC, Vieira, R, Leal-Junior, E, dos Santos, S, Ligeiro, AP, Albertini, R, Junior, J, de Carvalho, P: Effect of low-level laser therapy on the expression of inflammatory mediators and on neutrophils and macrophages in acute joint inflammation. *Arthritis Res Ther,* 15**:** 116, 2013.

38. Ucero, AC, Sabban, B, Benito-Martin, A, Carrasco, S, Joeken, S, Ortiz, A: Laser therapy in metabolic syndrome-related kidney injury. *Photochem Photobiol,* 89**:** 953-960, 2013.

39. Silva, G, Ferraresi, C, de Almeida, RT, Motta, ML, Paixao, T, Ottone, VO, Fonseca, IA, Oliveira, MX, Rocha-Vieira, E, Dias-Peixoto, MF, Esteves, EA, Coimbra, CC, Amorim, FT, de Castro Magalhaes, F: Infrared photobiomodulation (PBM) therapy improves glucose metabolism and intracellular insulin pathway in adipose tissue of high-fat fed mice. *Lasers Med Sci,* 33**:** 559-571, 2018.

40. De Freitas, LF, Hamblin, MR: Proposed Mechanisms of Photobiomodulation or Low-Level Light Therapy. *IEEE J Sel Top Quantum Electron,* 22**:** doi: 10.1109/JSTQE.2016.2561201, 2016.

41. McGuff, PE, Deterling, RA, Jr., Gottlieb, LS: Tumoricidal effect of laser energy on experimental and human malignant tumors. *N Engl J Med,* 273**:** 490-492, 1965.

42. Mester, E, Ludany, G, Selyei, M, Szende, B, Total, G: The stimulating effect of low power laser rays on biological systems. *Laser Rev***:** 3-9, 1968.

43. Mester, E, Szende, B, Gartner, P: The effect of laser beams on the growth of hair in mice. *Radiobiol Radiother (Berl),* 9**:** 621-626, 1968.

44. Chow, RT, Johnson, MI, Lopes-Martins, RA, Bjordal, JM: Efficacy of low-level laser therapy in the management of neck pain: a systematic review and meta-analysis of randomised placebo or active-treatment controlled trials. *Lancet,* 374**:** 1897-1908, 2009.

45. Houreld, NN: Shedding light on a new treatment for diabetic wound healing: a review on phototherapy. *Sci World J,* 2014**:** 398412, 2014.

46. Cremer, R, Perryman, P, Richards, D, Holbrook, B: Photo-sensitivity of serum bilirubin. *Biochem J,* 66**:** 60, 1957.

47. Cremer, RJ, Perryman, P, Richards, D: Influence of light on the hyperbilirubinaemia of infants. *Lancet,* 271**:** 1094-1097, 1958.

48. Jiao, Y, Jin, Y, Meng, H, Wen, M: An analysis on treatment effect of blue light phototherapy combined with Bifico in treating neonatal hemolytic jaundice. *Exp Ther Med,* 16**:** 1360-1364, 2018.

49. Ebbesen, F, Vandborg, PK, Madsen, PH, Trydal, T: Effect of phototherapy with turquoise vs. blue LED light of equal irradiance in jaundiced neonates. *Pediatr Res,* 79**:** 308-312, 2016.

50. Hansen, TWR, Maisels, MJ, Ebbesen, F, Vreman, HJ, Stevenson, DK, Wong, RJ: Sixty years of phototherapy for neonatal jaundice - from serendipitous observation to standardized treatment and rescue for millions. *J Perinatol,* 2019.

51. Hennessy, M, Hamblin, MR: Photobiomodulation and the brain: a new paradigm. *J Opt***:** doi: 10.1088/2040-8986/1019/1081/013003, 2017.

52. Sinclair, KL, Ponsford, JL, Taffe, J, Lockley, SW, Rajaratnam, SM: Randomized controlled trial of light therapy for fatigue following traumatic brain injury. *Neurorehabil Neural Repair,* 28**:** 303-313, 2014.

53. Wang, W, Wildes, CP, Pattarabanjird, T, Sanchez, MI, Glober, GF, Matthews, GA, Tye, KM, Ting, AY: A light- and calcium-gated transcription factor for imaging and manipulating activated neurons. *Nat Biotechnol,* 35**:** 864-871, 2017.

54. Ito, T, Yamadera, H, Ito, R, Endo, S: [Effects of bright light on cognitive disturbances in Alzheimer-type dementia]. *Nihon Ika Daigaku zasshi,* 66**:** 229-238, 1999.

55. Lee, JH, Bliwise, DL, Ansari, FP, Goldstein, FC, Cellar, JS, Lah, JJ, Levey, AI: Daytime sleepiness and functional impairment in Alzheimer disease. *Am J Geriatr Psychiatry,* 15**:** 620-626, 2007.

56. Yamadera, H, Ito, T, Suzuki, H, Asayama, K, Ito, R, Endo, S: Effects of bright light on cognitive and sleep-wake (circadian) rhythm disturbances in Alzheimer-type dementia. *Psychiatry Clin Neurosci,* 54**:** 352-353, 2000.

57. Shin, HY, Han, HJ, Shin, DJ, Park, HM, Lee, YB, Park, KH: Sleep problems associated with behavioral and psychological symptoms as well as cognitive functions in Alzheimer's disease. *J Clin Neurol,* 10**:** 203-209, 2014.

58. Alexiades, M: Laser and light-based treatments of acne and acne scarring. *Clin Dermatol,* 35**:** 183-189, 2017.

59. Tzung, TY, Wu, KH, Huang, ML: Blue light phototherapy in the treatment of acne. *Photodermatol Photoimmunol Photomed,* 20**:** 266-269, 2004.

60. Avci, P, Gupta, A, Sadasivam, M, Vecchio, D, Pam, Z, Pam, N, Hamblin, MR: Low-level laser (light) therapy (LLLT) in skin: stimulating, healing, restoring. *Semin Cutan Med Surg,* 32**:** 41-52, 2013.

61. Avci, P, Gupta, GK, Clark, J, Wikonkal, N, Hamblin, MR: Low-level laser (light) therapy (LLLT) for treatment of hair loss. *Lasers Surg Med,* 46**:** 144-151, 2014.

62. Ferraresi, C, Huang, YY, Hamblin, MR: Photobiomodulation in human muscle tissue: an advantage in sports performance? *J Biophotonics,* 9**:** 1273-1299, 2016.

63. Tumilty, S, Mani, R, Baxter, GD: Photobiomodulation and eccentric exercise for Achilles tendinopathy: a randomized controlled trial. *Lasers Med Sci,* 31**:** 127-135, 2016.

64. Da Cunha, RA, Pinfildi, CE, De Castro Pochini, A, Cohen, M: Photobiomodulation therapy and NMES improve muscle strength and jumping performance in young volleyball athletes: a randomized controlled trial study in Brazil. *Lasers Med Sci*, 2019.

65. Orssatto, L, Detanico, D, Kons, RL, Sakugawa, RL, da Silva, JN, Jr., Diefenthaeler, F: Photobiomodulation Therapy Does Not Attenuate Fatigue and Muscle Damage in Judo Athletes: A Randomized, Triple-Blind, Placebo-Controlled Trial. *Front Physiol***:** doi: 10.3389/fphys.2019.00811, 2019.

66. Lanzafame, RJ, Stadler, I, Kurtz, AF, Connelly, R, Peter, TA, Sr., Brondon, P, Olson, D: Reciprocity of exposure time and irradiance on energy density during photoradiation on wound healing in a murine pressure ulcer model. *Lasers Surg Med,* 39**:** 534-542, 2007.

67. Sommer, AP, Pinheiro, AL, Mester, AR, Franke, RP, Whelan, HT: Biostimulatory windows in low-intensity laser activation: lasers, scanners, and NASA's light-emitting diode array system. *J Clin Laser Med Surg,* 19**:** 29-33, 2001.

68. Smith, KC: Low-level laser or led therapy is phototherapy. *Photomed Laser Surg,* 23**:** 78-80, 2013.

69. Karu, T: Photobiology of low-power laser effects. *Health Phys,* 56**:** 691-704, 1989.

70. Kato, M: Cytochrome oxidase is a possible photoreceptor in mitochondria. *Photobiochem Photobiophys,* 2**:** 263-269, 1981.
71. Gordon, SA, Surrey, K: Red and far-red action on oxidative phosphorylation. *Radiat Res,* 12**:** 325-339, 1960.
72. Passarella, S, Casamassima, E, Molinari, S, Pastore, D, Quagliariello, E, Catalano, IM, Cingolani, A: Increase of proton electrochemical potential and ATP synthesis in rat liver mitochondria irradiated in vitro by helium-neon laser. *FEBS Lett,* 175**:** 95-99, 1984.
73. Zhang, DX, Gutterman, DD: Mitochondrial reactive oxygen species-mediated signaling in endothelial cells. *Am J Physiol Heart Circ Physiol,* 292**:** 2023-2031, 2007.
74. Camello-Almaraz, C, Gomez-Pinilla, PJ, Pozo, MJ, Camello, PJ: Mitochondrial reactive oxygen species and Ca2+ signaling. *Am J Physiol Cell Physiol,* 291**:** 1082-1088, 2006.
75. Schieke, SM, Finkel, T: Mitochondrial signaling, TOR, and life span. *Biol Chem,* 387**:** 1357-1361, 2006.
76. Rhoads, DM, Subbaiah, CC: Mitochondrial retrograde regulation in plants. *Mitochondrion,* 7**:** 177-194, 2007.
77. Schroeder, P, Pohl, C, Calles, C, Marks, C, Wild, S, Krutmann, J: Cellular response to infrared radiation involves retrograde mitochondrial signaling. *Free Radic Biol Med,* 43**:** 128-135, 2007.
78. Brookes, PS, Yoon, Y, Robotham, JL, Anders, MW, Sheu, SS: Calcium, ATP, and ROS: a mitochondrial love-hate triangle. *Am J Physiol Cell Physiol,* 287**:** 817-833, 2004.
79. Butow, RA, Avadhani, NG: Mitochondrial signaling: the retrograde response. *Mol Cell,* 14**:** 1-15, 2004.
80. Vacca, RA, Marra, E, Quagliariello, E, Greco, M: Increase of both transcription and translation activities following separate irradiation of the in vitro system components with He-Ne laser. *Biochem Biophys Res Commun,* 203**:** 991-997, 1994.
81. Karu, TI, Pyatibrat, LV, Afanasyeva, NI: A novel mitochondrial signaling pathway activated by visible-to-near infrared radiation. *Photochem Photobiol,* 80**:** 366-372, 2004.
82. Klapczynski, A: Influence of photobiomodulation with blue light on the metabolism, proliferation and gene expression of human fibroblasts. *Medical Research Center.* Ruprecht-Karls-Universität Heidelberg, 2019.
83. Becker, A: Influence of photobiomodulation with blue light on the metabolism, proliferation and gene expression of human keratinocytes. *Medical Research Center.* Ruprecht-Karls-Universität Heidelberg, 2017.
84. Michaelides, K: Example of Sensor Positions on Wound Dressing. MEDILIGHT Deliverable WP 2.4, MEDILIGHT EU Project Horizon 2020, 2017.
85. Application Note, Co-culture in ThinCert cell culture inserts. www.gbo.com/bioscience, Greiner bio-one, 2007.
86. Vedula, SR, Ravasio, A, Lim, CT, Ladoux, B: Collective cell migration: a mechanistic perspective. *Physiology (Bethesda),* 28**:** 370-379, 2013.
87. Mello Coelho, V, Bunbury, A, Rangel, LB, Giri, B, Weeraratna, A, Morin, PJ, Bernier, M, Taub, DD: Fat-storing multilocular cells expressing CCR5 increase in the thymus with advancing age: potential role for CCR5 ligands on the differentiation and migration of preadipocytes. *Int J Med Sci,* 7**:** 1-14, 2009.
88. Product catalogue. www.ssniff.de, ssniff Spezialdiäten, 2017.

89. Kuch, N: Co-cultures of Fibroblasts and Keratinocytes under the influence of blue light. *Medical Research Center.* Hochschule Mannheim, University of Applied Sciences, 2016.

90. Norris, DA, Lyons, MB, Middleton, MH, Yohn, JJ, Kashihara-Sawami, M: Ultraviolet radiation can either suppress or induce expression of intercellular adhesion molecule 1 (ICAM-1) on the surface of cultured human keratinocytes. *J Invest Dermatol,* 95**:** 132-138, 1990.

91. Norris, DA, Morelli, J, Sawami, M, Yohn, J, Furukawa, F: Ultraviolet light (UVL) and epidermal cytotoxicity: perspectives on three different ways that UVL may influence cytotoxic damage. *Dermatologica,* 179 Suppl 1**:** 138-139, 1989.

92. Boonkaew, B, Kempf, M, Kimble, R, Cuttle, L: Cytotoxicity testing of silver-containing burn treatments using primary and immortal skin cells. *Burns,* 40**:** 1562-1569, 2014.

93. Lin, Y, Shao, Q, Zhang, M, Lu, C, Fleming, J, Su, S: Royal jelly-derived proteins enhance proliferation and migration of human epidermal keratinocytes in an in vitro scratch wound model. *BMC Complement Altern Med***:** doi: 10.1186/s12906-12019-12592-12907, 2019.

94. Thaweekitphathanaphakdee, S, Chanvorachote, P, Prateepchinda, S, Khongkow, M, Sucontphunt, A: Abalone Collagen Extracts Potentiate Stem Cell Properties of Human Epidermal Keratinocytes. *Mar Drugs***:** doi: 10.3390/md17070424, 2019.

95. Ascione, F, Vasaturo, A, Caserta, S, D'Esposito, V, Formisano, P, Guido, S: Comparison between fibroblast wound healing and cell random migration assays in vitro. *Exp Cell Res,* 347**:** 123-132, 2016.

96. Justus, CR, Leffler, N, Ruiz-Echevarria, M, Yang, LV: In vitro cell migration and invasion assays. *J Vis Exp***:** doi: 10.3791/51046, 2014.

97. Dos Anjos, C, Sabino, CP, Bueris, V, Fernandes, MR, Pogliani, FC, Lincopan, N, Sellera, FP: Antimicrobial blue light inactivation of international clones of multidrug-resistant Escherichia coli ST10, ST131 and ST648. *Photodiagnosis Photodyn Ther,* 27**:** 51-53, 2019.

98. Shehatou, C, Logunov, SL, Dunman, PM, Haidaris, CG, Klubben, WS: Characterizing the Antimicrobial Properties of 405 nm Light and the Corning(R) Light-Diffusing Fiber Delivery System. *Lasers Surg Med***:** doi: 10.1002/lsm.23132, 2019.

99. Halstead, FD, Hadis, MA, Marley, N, Brock, K, Milward, MR, Cooper, PR, Oppenheim, B, Palin, WM: Violet-Blue Light Arrays at 405nm Exert Enhanced Antimicrobial Activity for Photodisinfection of Monomicrobial Nosocomial Related Biofilms. *Appl Environ Microbiol***:** doi: 10.1128/AEM.01346-01319, 2019.

100. Cheung, HM, Chow, TCH, Yew, DTW: How Ketamine Affects Livers of Pregnant Mice and Developing Mice? *Int J Mol Sci***:** doi: 10.3390/ijms18051098, 2017.

101. Leffa, DD, Bristot, BN, Damiani, AP, Borges, GD, Daumann, F, Zambon, GM, Fagundes, GE, de Andrade, VM: Anesthetic Ketamine-Induced DNA Damage in Different Cell Types In Vivo. *Mol Neurobiol,* 53**:** 5575-5581, 2016.

102. Lasic, E, Lisjak, M, Horvat, A, Bozic, M, Sakanovic, A, Anderluh, G, Verkhratsky, A, Vardjan, N, Jorgacevski, J, Stenovec, M, Zorec, R: Astrocyte Specific Remodeling of Plasmalemmal Cholesterol Composition by Ketamine Indicates a New Mechanism of Antidepressant Action. *Sci Rep,* 9**:** 10957, 2019.

103. Wen, C, Zhang, M, Ma, J, Hu, L, Wang, X, Lin, G: Urine metabolomics in rats after administration of ketamine. *Drug Des Devel Ther,* 9**:** 717-722, 2015.

104. Grover, Z, Ee, LC: Protein energy malnutrition. *Pediatr Clin North Am,* 56**:** 1055-1068, 2009.
105. Yamada, S, Tokumoto, M, Tatsumoto, N, Tsuruya, K, Kitazono, T, Ooboshi, H: Very low protein diet enhances inflammation, malnutrition, and vascular calcification in uremic rats. *Life Sci,* 146**:** 117-123, 2016.
106. Clyne, B, Olshaker, JS: The C-reactive protein. *J Emerg Med,* 17**:** 1019-1025, 1999.
107. Serrage, H, Heiskanen, V, Palin, WM, Cooper, PR, Milward, MR, Hadis, M, Hamblin, MR: Under the spotlight: mechanisms of photobiomodulation concentrating on blue and green light. *Photochem Photobiol Sci,* 18**:** 1877-1909, 2019.
108. Becker, A, Klapczynski, A, Kuch, N, Arpino, F, Simon-Keller, K, De La Torre, C, Sticht, C, van Abeelen, FA, Oversluizen, G, Gretz, N: Gene expression profiling reveals aryl hydrocarbon receptor as a possible target for photobiomodulation when using blue light. *Sci Rep***:** doi: 10.1038/srep33847, 2016.
109. Rohringer, S, Holnthoner, W, Chaudary, S, Slezak, P, Priglinger, E, Strassl, M, Pill, K, Muhleder, S, Redl, H: The impact of wavelengths of LED light-therapy on endothelial cells. *Sci Rep***:** doi: 10.1038/s41598-41017-11061-y, 2017.
110. Harita, N, Hayashi, T, Sato, KK, Nakamura, Y, Yoneda, T, Endo, G, Kambe, H: Lower serum creatinine is a new risk factor of type 2 diabetes: the Kansai healthcare study. *Diabetes Care,* 32**:** 424-426, 2009.
111. Alba, MN, Gerenutti, M, Yoshida, VM, Grotto, D: Clinical comparison of salicylic acid peel and LED-Laser phototherapy for the treatment of Acne vulgaris in teenagers. *J Cosmet Laser Ther,* 19**:** 49-53, 2017.
112. Falcone, D, Uzunbajakava, NE, van Abeelen, F, Oversluizen, G, Peppelman, M, van Erp, PEJ, van de Kerkhof, PCM: Effects of blue light on inflammation and skin barrier recovery following acute perturbation. Pilot study results in healthy human subjects. *Photodermatol Photoimmunol Photomed,* 34**:** 184-193, 2018.
113. Yoshimura, TM, Sabino, CP, Ribeiro, MS: Photobiomodulation reduces abdominal adipose tissue inflammatory infiltrate of diet-induced obese and hyperglycemic mice. *J Biophotonics,* 9**:** 1255-1262, 2016.

7 APPENDIX

Table 24: Complete list of significantly deregulated pathways belonging to KEGG's main category 'Metabolism'. The main category is divided into 13 subcategories. Seven of these categories contain significantly deregulated pathways. They are depicted with their respective NES and adjusted p-values. Up-regulated pathways are indicated by the positive NES colored in red and down-regulated pathways are indicated by the negative NES colored in green. Comparisons were done by the respective conditions of diabetic (DB) or non-diabetic (NDB) rats and animals which received the light treatment (BL) or their control (C).

1. Metabolism				
	DB - C / DB - BL		**NDB - BL / DB - BL**	
	NES	**Adjusted p-value**	**NES**	**Adjusted p-value**
1.0. Global and overview maps				
Metabolic pathways	-1.18	0.0624	-1.29	0.0018
Carbon metabolism	1.02	0.5138	-2.06	0.0012
2-Oxocarboxylic acid metabolism	0.95	0.6326	-1.87	0.0037
Fatty acid metabolism	-1.76	0.0072	-1.67	0.0080
Biosynthesis of amino acids	1.04	0.4762	-1.71	0.0049
1.1. Carbohydrate metabolism				
Glycolysis and Gluconeogenesis	1.69	0.0173	-1.08	0.3913
Citrate cycle (TCA cycle)	1.25	0.2596	-2.08	0.0012
Galactose metabolism	1.55	0.0649	1.56	0.0385
Starch and sucrose metabolism	1.86	0.0102	0.87	0.6983
Amino sugar and nucleotide sugar metabolism	-0.78	0.8737	1.85	0.0015
Propanoate metabolism	-1.11	0.4305	-2.15	0.0012
Pyruvate metabolism	1.21	0.3031	-1.86	0.0025
Glyoxylate and dicarboxylae metabolism	-0.92	0.6654	-1.92	0.0025
Butanoate metabolism	-1.59	0.0591	-1.67	0.0250
1.2. Energy metabolism				
Oxidative Phosphorylation	-0.70	0.9898	-2.68	0.0012
1.3. Lipid metabolism				
Steroid biosynthesis	-2.39	0.0055	-1.84	0.0040
Biosynthesis of unsaturated fatty acids	-2.07	0.0055	-1.10	0.3918
Fatty acid elongation	-1.94	0.0059	-1.38	0.1364
Steroid hormone biosynthesis	-1.82	0.0059	-0.64	0.9856
Sphingolipid metabolism	-1.67	0.0239	2.04	0.0012
Glycerolipid metabolism	1.63	0.0239	1.23	0.1437
Ether lipid metabolism	-1.14	0.3821	1.51	0.0373
Fatty acid biosynthesis	-1.21	0.3485	-1.64	0.0314
1.4. Nucleotide metabolism				
Purine metabolism	1.54	0.0143	1.46	0.0162
1.5. Amino acid metabolism				
Cysteine and methionine metabolism	-1.13	0.3953	-1.99	0.0014
Valine, leucine and isoleucine degradation	-0.93	0.6654	-1.76	0.0044
1.6. Metabolism of other amino acids				
beta-Alanine metabolism	1.89	0.0086	0.94	0.6061
Glutathione metabolism	1.56	0.0409	-1.24	0.2056

1.7. Glycan biosynthesis and metabolism				
Mucin type O-glycan biosynthesis	1.97	0.0064	1.71	0.0151
Glycosylphosphatidylinositol (GPI)-anchor biosynthesis	-1.89	0.0084	-1.14	0.3513
Glycosaminoglycan biosynthesis	2.22	0.0012	2.22	0.0012
Glycosaminoglycan degradation	-0.71	0.9067	2.16	0.0020
Various types of N-glycan biosynthesis	1.4	0.122	1.85	0.0021
Other glycan degradation	1.07	0.4732	2.07	0.0025
Glycosphingolipid biosynthesis	1.28	0.2751	1.97	0.0035
N-Glycan biosynthesis	0.97	0.6142	1.76	0.0042
1.8. Metabolism of cofactors and vitamins				
Retinol metabolism	-1.63	0.0219	0.87	0.7587
1.9. Metabolism of terpenoids and polyketides				
Terpenoid backbone biosynthesis	-1.88	0.0084	-1.19	0.3041
1.11. Xenobiotics biodegradation and metabolism				
Drug metabolism	1.68	0.0189	0.92	0.6701

Table 25: Complete list of significantly deregulated pathways belonging to KEGG's main category 'Genetic Information Processing'. The main category is divided into 4 subcategories. All of these categories contain significantly deregulated pathways. They are depicted with their respective NES and adjusted p-values. Up-regulated pathways are indicated by the positive NES colored in red and down-regulated pathways are indicated by the negative NES colored in green. Comparisons were done by the respective conditions of diabetic (DB) or non-diabetic (NDB) rats and animals which received the light treatment (BL) or their control (C).

2. Genetic Information Processing	DB - C / DB - BL		NDB - BL / DB - BL	
	NES	Adjusted p-value	NES	Adjusted p-value
2.1. Transcription				
Spliceosome	-1.60	0.0096	-2.38	0.0012
RNA polymerase	-1.05	0.5014	-1.99	0.0012
Basal transcription factors	-0.84	0.8008	-1.92	0.0014
2.2. Translation				
Ribosome	-1.89	0.0055	-2.60	0.0012
Ribosome biogenesis in eukaryotes	-1.68	0.0142	-2.30	0.0012
Aminoacyl-tRNA biosynthesis	-1.07	0.4575	-2.10	0.0012
RNA transport	-1.1	0.375	-2.35	0.0012
mRNA surveillance pathway	-1.26	0.2088	-2.12	0.0012
2.3. Folding, sorting and degradation				
RNA degradation	-1.75	0.0087	-2.12	0.0012
Proteasome	-1.70	0.0189	-2.25	0.0012
Protein processing in endoplasmic reticulum	1.09	0.3622	1.63	0.0038
Ubiquitin mediated proteolysis	0.93	0.7121	-1.43	0.0304
2.4. Replication and repair				
DNA replication	-1.42	0.1274	-2.30	0.0012
Nucleotide excision repair	-1.33	0.1859	-2.29	0.0012
Mismatch repair	-0.82	0.7886	-1.91	0.0026
Homologous recombination	-0.8	0.8436	-1.83	0.0035
Base excision repair	-1.36	0.1687	-1.75	0.009
Fanconi anemia pathway	-1.07	0.4600	-1.51	0.0401

Table 26: Complete list of significantly deregulated pathways belonging to KEGG's main category 'Environmental Information Processes'. The main category is divided into 3 subcategories. Two of these categories contain significantly deregulated pathways. They are depicted with their respective NES and adjusted p-values. Up-regulated pathways are indicated by the positive NES colored in red and down-regulated pathways are indicated by the negative NES colored in green. Comparisons were done by the respective conditions of diabetic (DB) or non-diabetic (NDB) rats and animals which received the light treatment (BL) or their control (C).

3. Environmental Information Processes

	DB - C / DB - BL		NDB - BL / DB - BL	
	NES	Adjusted p-value	NES	Adjusted p-value
3.2. Signal transduction				
Hippo signaling pathway	-1.93	0.0055	-1.25	0.1286
HIF-1 signaling pathway	1.76	0.0055	1.81	0.0012
TNF signaling pathway	1.99	0.0055	2.20	0.0012
FoxO signaling pathway	1.66	0.0055	1.31	0.0652
JAK-STAT signaling pathway	1.78	0.0055	2.16	0.0012
cAMP signaling pathway	1.60	0.0067	1.76	0.0012
MAPK signaling pathway	1.46	0.0074	1.70	0.0012
PI3K-Akt signaling pathway	1.42	0.0080	2.32	0.0012
Calcium signaling pathway	1.49	0.0096	1.41	0.0150
NF-kappa B signaling pathway	1.60	0.0156	2.49	0.0012
cGMP-PKG signaling pathway	1.49	0.0162	1.72	0.0012
Rap1 signaling pathway	1.41	0.0206	2.15	0.0012
Ras signaling pathway	1.37	0.0261	2.02	0.0012
Sphingolipid signaling pathway	-0.97	0.6308	2.10	0.0012
Phospholipase D signaling pathway	1.27	0.1016	1.99	0.0012
Apelin signaling pathway	1.28	0.1103	1.77	0.0012
Wnt signaling pathway	-1.37	0.0778	-1.48	0.0141
Phosphatidylinositol signaling system	1.08	0.4208	1.46	0.0241
3.3. Signaling molecules and interaction				
Viral protein interaction with cytokine and cytokine receptor	1.97	0.0055	2.92	0.0012
Cytokine-cytokine receptor interaction	1.53	0.0072	2.55	0.0012
Neuroactive ligand-receptor interaction	1.44	0.0096	1.33	0.0096
ECM-receptor interaction	1.27	0.1692	2.58	0.0012
Cell adhesion molecules (CAMs)	-1.24	0.1897	2.23	0.0012

Table 27: Complete list of significantly deregulated pathways belonging to KEGG's main category 'Cellular Processes'. The main category is divided into 5 subcategories. Four of these categories contain significantly deregulated pathways. They are depicted with their respective NES and adjusted p-values. Up-regulated pathways are indicated by the positive NES colored in red and down-regulated pathways are indicated by the negative NES colored in green. Comparisons were done by the respective conditions of diabetic (DB) or non-diabetic (NDB) rats and animals which received the light treatment (BL) or their control (C).

4. Cellular Processes				
	DB - C / DB - BL		NDB - BL / DB - BL	
	NES	Adjusted p-value	NES	Adjusted p-value
4.1. Transport and catabolism				
Peroxisome	-1.74	0.0096	-1.63	0.0078
Autophagy	1.52	0.0156	-1.48	0.0683
Lysosome	1.50	0.0188	2.89	0.0012
Phagosome	1.40	0.0394	2.68	0.0012
Endocytosis	-0.80	0.9464	1.99	0.0012
4.2. Cell growth and death				
Cell cycle	-1.80	0.0055	-2.08	0.0012
Apoptosis	1.69	0.0055	2.26	0.0012
Necroptosis	1.60	0.0064	1.81	0.0012
Ferroptosis	1.76	0.0162	1.43	0.0708
Oocyte meiosis	-1.36	0.1100	-1.48	0.0221
4.3. Cellular community				
Focal adhesion	1.83	0.0055	2.64	0.0012
Gap junction	1.32	0.1183	1.84	0.0016
Adherens junction	-1.08	0.4460	1.53	0.0202
4.5. Cell motility				
Regulation of actin cytoskeleton	1.18	0.1634	2.13	0.0012

Table 28: Complete list of significantly deregulated pathways belonging to KEGG's main category 'Organismal Systems'. The main category is divided into 10 subcategories. Nine of these categories contain significantly deregulated pathways. They are depicted with their respective NES and adjusted p-values. Up-regulated pathways are indicated by the positive NES colored in red and down-regulated pathways are indicated by the negative NES colored in green. Comparisons were done by the respective conditions of diabetic (DB) or non-diabetic (NDB) rats and animals which received the light treatment (BL) or their control (C).

5. Organismal Systems

	DB - C / DB - BL		NDB - BL / DB - BL	
	NES	Adjusted p-value	NES	Adjusted p-value
5.1. Immune system				
Toll-like receptor signaling pathway	1.94	0.0055	2.17	0.0012
Natural killer cell mediated cytotoxicity	1.84	0.0055	2.06	0.0012
Chemokine signaling pathway	1.75	0.0055	2.72	0.0012
NOD-like receptor signaling pathway	1.64	0.0055	2.25	0.0012
Complement and coagulation cascades	1.78	0.0084	2.69	0.0012
Hematopoietic cell lineage	1.67	0.0119	2.77	0.0012
B cell receptor signaling pathway	1.70	0.0142	1.94	0.0012
Intestinal immune network for IgA production	1.67	0.0239	2.3	0.0012
Fc epsilon RI signaling pathway	1.60	0.0239	1.82	0.0015
IL-17 signaling pathway	1.55	0.0265	1.87	0.0012
Platelet activation	1.29	0.1100	2.42	0.0012
Antigen processing and presentation	-0.96	0.6308	1.99	0.0012
Th1 and Th2 cell differentiation	1.09	0.4001	1.9	0.0012
Th17 cell differentiation	1.36	0.0778	2.08	0.0012
Fc gamma R-mediated phagocytosis	1.01	0.5287	2.35	0.0012
Leukocyte transendothelial migration	1.12	0.3426	2.41	0.0012
C-type lectin receptor signaling pathway	1.19	0.2329	1.75	0.0024
T cell receptor signaling pathway	1.33	0.0959	1.53	0.0138
5.2. Endocrine system				
Insulin signaling pathway	2.05	0.0055	1.03	0.4552
Prolactin signaling pathway	1.82	0.0102	1.58	0.0138
Regulation of lipolysis in adipocytes	1.79	0.0124	2.02	0.0012
Adipocytokine signaling pathwaay	1.72	0.0164	1.33	0.0922
Relaxin signaling pathway	1.49	0.0194	1.94	0.0012
Glucagon signaling pathway	1.53	0.0241	1.03	0.4437
Aldosterone synthesis and secretion	1.50	0.0293	1.78	0.0023
Renin-angiotensin system	1.43	0.1210	2.1	0.0012
Estrogen signaling pathway	-1.29	0.1473	-1.75	0.0012
Renin secretion	1.43	0.0748	2.05	0.0012
Parathyroid hormone synthesis, secretion and action	1.23	0.1859	1.84	0.0012
Thyroid hormone synthesis	1.06	0.4346	1.64	0.0078
Oxytocin signaling pathway	1.22	0.1473	1.45	0.0141
Cortisol synthesis and secretion	1.37	0.1210	1.54	0.0202
GnRH signaling pathway	1.26	0.1825	1.43	0.0346
GnRH secretion	1.39	0.1025	1.49	0.0316

5.3. Circulatory system					
Vascular smooth muscle contraction	1.39	0.0487		1.90	0.0012
Cardiac muscle contraction	0.99	0.5765	-1.71		0.0027
5.4. Digestive system					
Protein digestion and absorption	1.15	0.3133		2.2	0.0012
Salivary secretion	1.14	0.3321		1.74	0.0028
Pancreatic secretion	-1.02	0.5138		1.68	0.0047
Cholesterol metabolism	1.14	0.3622		1.64	0.0108
Gastric acid secretion	-1.21	0.2751		1.51	0.0191
Vitamin digestion and absorption	-1.23	0.3094		1.67	0.0196
5.5. Excretory system					
Endocrine and other factor-regulated calcium reabsorption	1.14	0.3563		1.60	0.0173
5.6. Nervous system					
Neurotrophin signaling pathway	1.43	0.0386		1.57	0.0074
Cholinergic synapse	1.07	0.4192		1.75	0.0012
Serotonergic synapse	-1.05	0.4761		1.76	0.0012
Long-term depression	1.01	0.5287		1.73	0.0038
Retrograde endocannabinoid signaling	-0.77	0.9464	-1.44		0.0254
Glutamatergic synapse	-1.03	0.5138		1.36	0.0422
5.8. Development					
Osteoclast differentiation	2.50	0.0055		2.57	0.0012
Axon guidance	-1.48	0.0188		1.25	0.0867
5.9. Aging					
Longevity regulating pathway	1.46	0.0442		1.05	0.4147
5.10. Environmental adaptation					
Thermogenesis	1.09	0.3425	-2.42		0.0012
Circadian entrainment	-0.91	0.7121		1.79	0.0016

Table 29: Complete list of significantly deregulated pathways belonging to KEGG's main category 'Human Diseases'. The main category is divided into 12 subcategories. Ten of these categories contain significantly deregulated pathways. They are depicted with their respective NES and adjusted p-values. Up-regulated pathways are indicated by the positive NES colored in red and down-regulated pathways are indicated by the negative NES colored in green. Comparisons were done by the respective conditions of diabetic (DB) or non-diabetic (NDB) rats and animals which received the light treatment (BL) or their control (C).

6. Human Diseases

	DB - C / DB - BL		NDB - BL / DB - BL	
	NES	Adjusted p-value	NES	Adjusted p-value
6.1. Cancers - Overview				
Pathways in cancer	1.51	0.0064	1.97	0.0015
Transcriptional misregulation in cancer	1.70	0.0055	1.69	0.0012
Proteoglycans in cancer	1.09	0.3525	1.96	0.0012
MicroRNAs in cancer	0.91	0.8436	1.49	0.0028
Central carbon metabolism in cancer	1.19	0.2751	1.42	0.0481
Choline metabolism in cancer	1.23	0.1916	1.48	0.0217
PD-L1 expression and PD-1 checkpoint pathway in cancer	1.43	0.0637	1.72	0.0046
6.2. Cancers - specific types				
Pancreatic cancer	1.93	0.0059	1.57	0.0147
Basal cell carcinoma	-1.58	0.0284	-1.55	0.0271
Chronic myeloid leukemia	1.89	0.0059	1.40	0.0480
Acute myeloid leukemia	2.02	0.0059	1.37	0.0708
Small cell lung cancer	1.52	0.0268	1.78	0.0028
Glioma	1.37	0.1016	1.59	0.0138
Prostate cancer	1.08	0.4192	1.41	0.0304
Melanoma	1.43	0.0778	1.51	0.0199
6.3. Immune diseases				
Rheumatoid arthritis	1.94	0.0059	2.85	0.0012
Inflammatory bowel disease (IBD)	1.18	0.3080	2.48	0.0012
Graft-versus-host disease	1.29	0.1974	2.17	0.0012
Asthma	1.15	0.3846	2.09	0.0014
Autoimmune thyroid disease	1.03	0.5063	1.73	0.0054
Allograft rejection	1.13	0.3694	1.90	0.0015
Primary immunodeficiency	1.04	0.5028	1.82	0.0078
6.4. Neurogenerative diseases				
Prion diseases	1.80	0.0143	2.13	0.0012
Alzheimer disease	0.71	1.0000	-2.06	0.0012
Parkinson disease	0.61	1.0000	-2.64	0.0012
Huntington disease	0.82	0.9585	-2.36	0.0012
6.6. Cardiovascular diseases				
Fluid shear stress and atherosclerosis	1.96	0.0055	2.02	0.0012
Hypertrophic cardiomyopathy (HCM)	1.51	0.0328	1.42	0.0335
Dilated cardiomyopathy (DCM)	1.49	0.0347	1.49	0.0182
Morphine addiction	1.37	0.0815	1.87	0.0012
Viral myocarditis	1.31	0.1473	2.00	0.0012

6.7. Endocrine and metabolic diseases					
AGE-RAGE signaling pathway in diabetic complications	2.02	0.0055		2.47	0.0012
Insulin resistance	1.62	0.0096		1.23	0.1347
Type II diabetes mellitus	1.59	0.0328		1.00	0.5254
Non-alcoholic fatty liver disease (NAFLD)	1.31	0.0826	-2.07		0.0012
Type I diabetes mellitus	1.32	0.1634		1.94	0.0012
6.8. Endocrine and metabolic diseases					
Yersinia infection	1.89	0.0055		2.20	0.0012
Salmonella infection	1.95	0.0059		2.37	0.0012
Pertussis	1.59	0.0239		2.82	0.0012
Tuberculosis	1.45	0.0239		2.57	0.0012
Bacterial invasion of epithelial cells	0.69	0.9905		2.37	0.0012
Legionellosis	1.38	0.1183		1.69	0.0097
Staphylococcus aureus infection	-1.10	0.4090	-1.80		0.0017
6.9. Endocrine and metabolic diseases					
Human cytomegalovirus infection	1.59	0.0058		2.18	0.0012
Hepatitis B	1.56	0.0064		1.78	0.0012
Kaposi sarcoma-associated herpesvirus infection	1.47	0.0142		1.96	0.0012
Herpes simplex virus 1 infection	1.32	0.0253		1.54	0.0012
Measles	1.24	0.1473		1.92	0.0012
Influenza A	1.36	0.0578		2.35	0.0012
Human papillomavirus infection	-1.15	0.2596		1.65	0.0012
Human immunodeficiency virus 1 infection	1.06	0.3953		1.69	0.0012
Hepatitis C	1.01	0.5287		1.65	0.0025
Human T-cell leukemia virus 1 infection	1.17	0.1677		1.43	0.0087
Epstein-Barr virus infection	0.92	0.7886		1.45	0.0089
6.10. Infectious diseases					
Leishmaniasis	2.02	0.0059		2.72	0.0012
Malaria	2.00	0.0059		2.87	0.0012
Amoebiasis	1.77	0.0061		2.61	0.0012
African trypanosomiasis	1.88	0.0086		2.26	0.0012
Chagas disease (American trypanosomiasis)	1.37	0.0740		2.23	0.0012
Taxoplasmosis	1.16	0.2751		2.49	0.0012
6.12. Drug resistance					
Platinum drug resistance	1.61	0.0239		1.07	0.3872
Endocrine resistance	1.52	0.0264		1.34	0.0652
EGFR tyrosine kinase inhibitor resistance	1.48	0.0487		1.96	0.0012

8 CURRICULUM VITAE AND PUBLICATIONS

PERSONALIEN

Name und Vorname:	Natalia Kuch
Geburtsdatum:	11.01.1990
Geburtsort:	Saran, Kasachstan
Familienstand:	Ledig
Vater:	Johann Kuch
Mutter:	Tatjana Kuch

SCHULISCHER WERDEGANG

09/2000 – 06/2009　　Theodor-Heuss-Gymnasium Pforzheim
　　　　　　　　　　　　　Note: 2,1

UNIVERSITÄRER WERDEGANG

01/2016 – heute　　　　Doktorandin am Zentrum für Medizinische Forschung,
　　　　　　　　　　　　　Universität Heidelberg, Deutschland
　　　　　　　　　　　　　Doktorarbeit: Influence of blue light on skin models
　　　　　　　　　　　　　consisting of fibroblasts and keratinocytes

10/2013 – 01/2016　　　Master of Science – Bioprocess Development
　　　　　　　　　　　　　Hochschule Mannheim
　　　　　　　　　　　　　Note: 1,7
　　　　　　　　　　　　　Master-Thesis
　　　　　　　　　　　　　Co-cultures of Fibroblasts and Keratinocytes under the
　　　　　　　　　　　　　influence of blue light

Betreuer: Prof. Dr. med. Norbert Gretz

Zentrum für Medizinische Forschung, Ruprecht-Karls-Universität Heidelberg

10/2009 – 08/2013   Bachelor of Science - Biotechnologie

Hochschule Mannheim

Note: 2,1

Bachelor-Thesis

Aufklärung der Biosynthesewege von Xenorhabdinen und Phenylethylamiden in *Xenorhabdus*

Betreuer: Prof. Dr. Helge B. Bode

Institut für Molekulare Biotechnologie, Goethe-Universität Frankfurt am Main

Praxissemesterarbeit

Assaying Cell Death in the Root Apex of Arabidopsis Thaliana after Induction of Genotoxic Stress

Betreuer: Dr. rer. nat. Peter Doerner

Institute of Molecular Plant Sciences, University of Edinburgh, Scotland

9 ACKNOWLEDGEMENTS

First of all, I would like to thank Prof. Norbert Gretz for the opportunity to work on such an interesting and innovative topic. I enjoyed working on an important and future oriented project and would like to thank him for the advice and support throughout the past years. I am grateful he recommended me for the graduate school, which did not only help me gain more knowledge about relevant topics, but also providing financial support.

Also, I would like to thank Sina Schwalm and Edda Eustachi for helping with small and big bureaucratic obstacles and the encouragement and supporting optimism.

Further, I would like to thank Jasmin Baumgartl and Cathleen Fichtner for their support in the lab. Without you many critical situations could not have been handled as well. Thank you for your scientific advice and taking the time to help me take care of my problems.

I also thank Maria Muciek, Dr. Carsten Sticht and especially Dr. Carolina De La Torre for helping me with the gene expression analysis. Viktoria Skude and Alexander Schlund also deserve my sincere gratitude for introducing me to the animal facility and the countless hours they took to support me and my project.

Moreover, thank you to all colleagues from the ZMF. Thank you for the mental support, the conversations and being more than colleagues. A special thanks to Anna Klapczynski, Fabiola Arpino, Stefania Palumbo, Cristina Daniele and, again, Dr. Carolina De La Torre for sharing hardships and successes and mutually supporting each other.

Last but not least, I want to express my gratitude to my friends and my boyfriend. Thank you for your constant support and patience. I appreciate your personal advices and am grateful for always having an open ear.